ACCEPTED FOR PUBLICATION IN THE AJ SPECIAL THINGS ISSUE
Preprint typeset using LaTeX style emulateapj v. 10/09/06

arXiv:0810.2116v2 [astro-ph] 14 Oct 2008

DYNAMICAL CENTERS AND NON-CIRCULAR MOTIONS IN THINGS GALAXIES: IMPLICATIONS FOR DARK MATTER HALOS

C. TRACHTERNACH[1], W.J.G. DE BLOK[2], F. WALTER[3], E. BRINKS[4], R.C. KENNICUTT, JR.[5]

Accepted for publication in the AJ special THINGS issue

ABSTRACT

We present harmonic decompositions of the velocity fields of 19 galaxies from THINGS (The H I Nearby Galaxy Survey) which quantify the magnitude of the non-circular motions in these galaxies and yield observational estimates of the elongations of the dark matter halo potentials. Additionally, we present accurate dynamical center positions for these galaxies. We show that the positions of the kinematic and photometric centers of the large majority of the galaxies in our sample are in good agreement. The median absolute amplitude of the non-circular motions, averaged over our sample, is 6.7 $\mathrm{km\,s^{-1}}$, with ~ 90 percent of the galaxies having median non-circular motions of less than $\sim 9\,\mathrm{km\,s^{-1}}$. As a fraction of the total rotation velocity this translates into 4.5 percent on average. The mean elongation of the gravitational potential, after a statistical correction for an unknown viewing angle, is 0.017 ± 0.020, i.e., consistent with a round potential. Our derived non-circular motions and elongations are smaller than what is needed to bring Cold Dark Matter (CDM) simulations in agreement with the observations. In particular, the amplitudes of the non-circular motions are not high enough to hide the steep central mass-density profiles predicted by CDM simulations. We show that the amplitudes of the non-circular motions decrease towards lower luminosities and later Hubble types.

Subject headings: galaxies: kinematics and dynamics — dark matter — galaxies: fundamental parameters — galaxies: ISM — galaxies: spiral — galaxies: dwarf

1. INTRODUCTION

Dark Matter is one of the fundamental ingredients of our current cosmological paradigm (e.g., Spergel et al. 2007). It is the dominant mass component in most galaxies, and as such determines the properties and evolution of these objects. Measuring or modeling the properties of these dark matter halos can thus help improve our knowledge of galaxy evolution and its relation with cosmology. Dark matter cannot be observed directly, so its characteristics must be derived observationally by studying the gravitational effect it has on tracer particles (be it atoms or photons). Alternatively, its properties can be studied using sophisticated computer simulations. The latter have now converged on a picture where dark matter consists of massive, non-relativistic particles, also called Cold Dark Matter (CDM).

Simulations adopting this framework find galaxy halos to be tri-axial (e.g., Frenk et al. 1988; Dubinski 1994; Hayashi et al. 2004, 2007; Capuzzo-Dolcetta et al. 2007), and to have a characteristic mass density profile. Its most distinghuishing feature is the steep increase in dark matter density towards the center, usually described as a power-law $\rho \sim r^{\alpha}$ with $\alpha \leq -1$ (e.g., Navarro et al. 1996, 1997). Much effort has been dedicated to obtaining observational confirmation of these predictions, concentrating mainly on dark matter dominated galaxies. Most observational determinations of the distribution of dark matter in these galaxies (as deduced from their kinematics) seem, however, to indicate that it is not characterized by a r^{-1} "cusp", but by a central kpc-sized "core" with a constant dark matter density (McGaugh & de Blok 1998; de Blok et al. 2001a,b; Marchesini et al. 2002; de Blok & Bosma 2002; Gentile et al. 2004; Simon et al. 2003, 2005; de Blok 2005; Zackrisson et al. 2006; Gentile et al. 2007; Spano et al. 2008; Kuzio de Naray et al. 2006, 2008).

Whether this core is real or a result of unrecognized systematics in the observations has been the subject of some debate. For example, it is conceivable that the photometric and kinematic centers could be physically offset from each other (see, e.g, Matthews & Gallagher 2002), which would lead to an artifical flattening of the inferred mass density distribution if the "wrong" center is chosen (see, e.g., Swaters et al. 2003a). A second effect which has been discussed by many authors is the effect of non-circular motions. These are a natural consequence of tri-axial halos (Hayashi et al. 2004; Hayashi & Navarro 2006; Hayashi et al. 2007), but can also be caused by bars, spiral arms, or other perturbations to the potential (cf. Rhee et al. 2004; Valenzuela et al. 2007). As an example of how they could affect the observations, Hayashi & Navarro (2006) show that the ellipticity of the dark matter halo can induce large non-circular motions in the inner parts of galaxies (up to ~ 15 percent of the total rotation velocity), thus making an intrinsic *cuspy* density profile appear *cored*. Using simulated rotation curves, de Blok et al. (2003) show that non-circular motions of the order of ~ 20 $\mathrm{km\,s^{-1}}$ over a large fraction of the disk are needed to make them consistent with CDM halos (see also Gentile et al. 2005, who reach similar conclusions derived from actual observations).

As mentioned above, most of these studies have concentrated on dark matter dominated galaxies, and more specifically on extremely late-type spirals as well as late-type dwarf

Electronic address: trachter@astro.rub.de
Electronic address: edeblok@ast.uct.ac.za
Electronic address: walter@mpia-hd.mpg.de
Electronic address: E.Brinks@herts.ac.uk
Electronic address: robk@ast.cam.ac.uk
[1] Astronomisches Institut, Ruhr-Universität Bochum, Universitätsstraße 150, 44780 Bochum, Germany
[2] Department of Astronomy, University of Cape Town, Private Bag X3, Rondebosch 7701, South Africa
[3] Max Planck Institut für Astronomie, Königstuhl 17, 69117 Heidelberg, Germany
[4] Centre for Astrophysics Research, University of Hertfordshire, College Lane, Hatfield, AL10 9AB, United Kingdom
[5] Institute of Astronomy, University of Cambridge, Madingley Road, Cambridge CB3 0HA, United Kingdom

galaxies (a group of galaxies commonly known as Low Surface Brightness [LSB] galaxies). The baryonic components of these galaxies, being a minor contribution to the total mass, can be used in these systems as a tracer for the dark matter component. However, a question which naturally arises is how representative these galaxies are for the galaxy population at large. The shallow potentials and low mass surface densities potentially allow the possibility that their photometric and kinematic centers have particularly large offsets, and/or that the importance of non-circular motions in their disks is anomalously high. Systematic observational studies of center positions and non-circular motions in late-type spiral and dwarf galaxies are, however, still comparatively rare (but see, e.g., Matthews & Gallagher 2002; Simon et al. 2003, 2005; Gentile et al. 2005; Kuzio de Naray et al. 2006, 2008).

One can also take a broader approach and study non-circular motions and center offsets across the Hubble sequence, with the aim of, firstly, tying the existing studies of dark matter-dominated galaxies into a larger, established scheme of galaxy properties changing with Hubble type and luminosity, and, secondly, providing a baseline for future studies.

For this reason, we have embarked on a major study of a large sample spanning a major part of the Hubble sequence to measure possible offsets between positions of the dynamical and photometric centers, as well as the importance of any non-circular motions. We will be using the THINGS (The HI Nearby Galaxy Survey; Walter et al. 2008, see Section 2) sample which covers a large range in physical properties, and enables us to address aspects such as the importance of dark matter as a function of Hubble type, the applicability of dark matter models, the shapes of rotation curves, etc. Many of these topics are covered in some detail in de Blok et al. (2008) and Oh et al. (2008). The THINGS sample furthermore contains a number of dark matter dominated dwarf galaxies that should provide direct clues on the behaviour of the centers and the importance of non-circular motions in extremely late-type galaxies and enable a comparison with earlier Hubble types.

Deviations from purely circular motions in galaxies in general can have different causes, including chaotic non-circular motions induced for example by star formation (as investigated in detail for two THINGS dwarf galaxies in Oh et al. 2008), or systematic non-circular motions that relate to the potential (e.g., spiral arms, tri-axiality of the halo). Here, we will focus on the systematic non-circular motions. One way to quantify these is to make a harmonic decomposition of the velocity field. An extensive description of the harmonic decomposition technique is given in Schoenmakers (1999). Several groups have measured non-circular motions in disk galaxies using this technique (e.g., Schoenmakers et al. 1997; Wong et al. 2004; Gentile et al. 2005). However, none of these works report non-circular motions as large as those proposed by Hayashi & Navarro (2006). Simon et al. (2003) used a different technique to measure the non-circular motions in NGC 2976. They conclude that although the inner 300 pc of NGC 2976 contain relatively large non-circular motions, the slope of its (cored) density profile is not significantly affected by that. Swaters et al. (2003b) on the contrary argue that the non-circular motions in DDO 39 might prevent the derivation of a well-constrained density profile.

As for the center offsets, de Blok et al. (2001a) and de Blok (2004) show that significant differences between the mass density profiles of cored and cuspy halos become prominent interior to a radius of ~ 1 kpc. This radius follows directly from the halo models and is fairly independent of (realistic) assumptions on halo parameters of either model. Center offsets significantly smaller than a kpc are thus unlikely to have a major impact on the shapes of the rotation curves.

A previous study by Matthews & Gallagher (2002) directly addresses the issue of center offsets using high-resolution rotation curves of a sample of 21 extreme late-type, low-luminosity, low-surface brightness spiral galaxies. They compare the systemic velocities as derived from HI and Hα observations and in general find excellent agreement (for two-thirds of their sample the velocities agree to better than 10 km s^{-1}), leading them to conclude that "most extreme late-type spirals seem to have well-defined centers in spite of their often diffuse stellar disks and shallow central potentials."

In this paper we will quantify the central positions of the THINGS galaxies, as well as quantify the strength of the non-circular motions in these galaxies, and investigate their dependence on global galaxy properties, such as luminosity. We will also check whether the mass models of the THINGS galaxies as presented in de Blok et al. (2008) and Oh et al. (2008) are affected by these non-circular motions.

The paper is organized as follows. After a brief description of the sample in §2, we extensively discuss the various ways in which one can define the center of a galaxy in §3, and present our best determinations of the positions of the true kinematic centers of our sample galaxies. These center positions are used as inputs for our harmonic decompositions of the observed velocities, as described in §4. We illustrate the procedure and show the results for one case-study galaxy in detail in §5. Results for the rest of the sample are presented in the Appendix. Our results and several quality checks are presented and discussed in §6, and the conclusions are summarized in §7.

2. SAMPLE AND DATA

For our analysis, we used THINGS (The H I Nearby Galaxy Survey), an H I spectral line survey of 34 nearby disk galaxies obtained at the NRAO[6] VLA in B, C, and D arrays. THINGS contains a wide range of galaxy types, i.e., high and low surface brightness galaxies, grand design spirals and dwarf irregulars, barred and non–barred galaxies, all observed at high spatial ($\sim 10''$ for the natural weighted data cubes) and velocity (≤ 5.2 km s^{-1}) resolution (for a detailed description of THINGS, see Walter et al. 2008). The great advantage of THINGS is that all galaxies have been observed, reduced, and analyzed in a homogeneous manner. The large range in physical properties enables one to study trends with, e.g., Hubble type. Furthermore, as THINGS was designed to overlap with the SINGS survey (Spitzer Infrared Nearby Galaxies Survey, Kennicutt et al. 2003), we can use its IRAC 3.6 μm images (which give a virtually dust-free view of the stellar disk) to directly compare photometric and kinematic centers.

In this paper, we will study the kinematics of galaxies. We therefore use the sub-sample of THINGS for which de Blok et al. (2008) derived accurate rotation curves. This sample includes THINGS galaxies with inclinations larger than 40° that are not undergoing obvious strong interactions, as well as NGC 6946, which, despite its lower inclination proved suitable for the derivation of a rotation curve. Basic properties of the galaxies of our sample are given in Table 1.

[6] The National Radio Astronomy Observatory is a facility of the National Science Foundation operated under cooperative agreement by Associated Universities, Inc.

For our analysis, we used the velocity fields which were created by fitting hermite polynomials to the velocity profiles from the natural weighted data cubes (as described in detail in de Blok et al. 2008). Additionally, we made use of the radio continuum maps from THINGS (Walter et al. 2008), as well as the 3.6 μm images from SINGS (Kennicutt et al. 2003).

3. ESTIMATING GALAXY CENTERS

For a correct appraisal of the non-circular motions in a galaxy (as derived from a harmonic decomposition) it is important to accurately determine the position of its center (cf. Schoenmakers 1999). There are several ways in which one can determine the position of the center of a galaxy. As central activity in galaxies is likely to coincide with the bottom of the galaxy potential well, a central compact radio source is a good indicator of the center of a galaxy. Similarly, nuclear star clusters can be used to locate the center (Matthews & Gallagher 2002). One can also fit ellipses to the surface brightness distribution as well as construct a tilted-ring model using the kinematic data to obtain additional, independent estimates.

Ideally, these different determinations should all coincide. Large discrepancies can indicate strong disturbances, caused, e.g., by spiral arms or strong bars, or a genuine offset between the kinematic and photometric center. For the majority of our galaxies, multiple center estimates can be derived, namely kinematic centers derived from the velocity fields, as well as photometric centers as deduced from the 20-cm radio continuum maps taken from THINGS and from the *Spitzer* 3.6 μm images.

As will be shown in the subsequent analysis, for most galaxies the kinematic center position agrees with the position of the radio continuum source and/or the center as derived from the IRAC image within the uncertainties. In those cases where the positions of the photometric and kinematic centers could be determined accurately, we have generally adopted one of the photometric centers as our best center position, given that the photometric centers usually have smaller uncertainties. Note that this particular choice affects our determination of the non-circular motions. The position of the dynamical center is to first order that position which minimizes the non-circular motions in a tilted-ring fit and adopting this (or a variable) center position would thus results in non-circular motions slightly smaller than the ones derived here for the photometric centers. For most of our galaxies the difference will be minimal, but the general effect is important to keep in mind.

Also note that it is still important to evaluate any possible differences between the two types of centers, even when both are well-defined. This will enable a better understanding of possible systematic effects inherent in the method, which is important for the interpretation of the results from galaxies where the centers may not be as well-defined.

Below follows a description of the methods used to determine the various center estimates. An application of these methods is given for one "case-study" galaxy in Section 5. Detailed and more technical descriptions are then given for all galaxies in Appendix A.

3.1. *Radio continuum*

A nuclear point source in the radio continuum is usually associated with a central compact object, which naturally should be at (or very close to) the bottom of the potential well of the galaxy. For all galaxies which show such a source in the THINGS radio continuum maps, its position was determined by fitting a Gaussian to the central source. The uncertainties for the center positions estimated in this way are all similar ($\leq 1''$) and we therefore do not show individual uncertainties for center estimates deduced from the radio continuum.

3.2. *Spitzer/IRAC 3.6 μm image*

We make use of the high-resolution 3.6 μm images from SINGS (Kennicutt et al. 2003)[7]. These allow an almost dust-free view of the predominantly old stellar populations, though we note that the 3.6 μm band can also contain some trace emission from hot dust, PAHs and AGB stars.

For all galaxies in our sample, we determined the central 3.6 μm position by fitting ellipses using the GIPSY[8] task ELLFIT, taking care that the ellipse fits were not affected by small scale structures. For those galaxies which also show a well-defined nuclear source in the 3.6 μm image, we additionally derived the central position by fitting a Gaussian to the central source. The two different center estimates generally agree very well. However, as the center position derived by fitting a Gaussian to the central source is usually better constrained as the center from ELLFIT, we only list the former (where available) in Table 2. Because of the homogeneous and consistently small positional uncertainty of less than $1''$, we do not list these here.

3.3. *Kinematic center*

In addition to the photometric centers mentioned above, we also derive kinematic centers using the GIPSY task ROTCUR. This task fits a set of tilted rings of a given width to the velocity field of a galaxy and determines their central positions, rotation and systemic velocities, inclinations and position angles. We use the best available center position (i.e., a central continuum source, if present, otherwise a nuclear source in the 3.6 μm image and as a last resort the center as derived using ELLFIT) as an initial center estimate for ROTCUR and make a fit with all parameters left free (including the center). By averaging the central positions over a radial range unaffected by spiral arms or other large-scale disturbances, we derive the position of the kinematic center for each galaxy.

The determination of the positions of all centers are described in Appendix A, and all center estimates are summarized in Table 2, where our adopted best center positions are shown in bold face.

4. HARMONIC DECOMPOSITION

We perform a harmonic decomposition of the velocity fields by decomposing the velocities found along the tilted-rings into multiple terms of sine and cosine.

Following Schoenmakers (1999), we describe the line-of-sight velocity, $v_{\rm los}$, as:

$$v_{\rm los}(r) = v_{\rm sys}(r) + \sum_{m=1}^{N} c_m(r)\cos m\psi + s_m(r)\sin m\psi, \qquad (1)$$

where N is the maximum fit order used, r is the radial distance from the dynamical center, ψ is the azimuthal angle in the plane of the disk, and $v_{\rm sys}$ is the $0^{\rm th}$ order harmonic component, c_0. Initial tests showed that a decomposition of the velocity fields up to third order (i.e., $N = 3$) is sufficient to

[7] A small number of galaxies in our sample were not part of SINGS. For these galaxies, the data were retrieved from the *Spitzer* archive.

[8] GIPSY, the Groningen Image Processing SYstem (van der Hulst et al. 1992)

TABLE 1
BASIC PROPERTIES FOR THE GALAXIES IN OUR SAMPLE.

Name	D	r_{25}	M_B	i	PA	V_{tot}	Δr	M_{HI}	Type
	Mpc	kpc	mag	°	°	km s^{-1}	″	10^8 M$_\odot$	
(1)	(2)	(3)	(4)	(5)	(6)	(7)	(8)	(9)	(10)
NGC 925	9.2	14.2	–20.04	66	287	115	3.0	45.8	7
NGC 2366	3.4	2.2	–17.17	64	40	55	6.0	6.5	10
NGC 2403	3.2	7.4	–19.43	63	124	135	4.0	25.8	6
NGC 2841	14.1	14.2	–21.21	74	153	260	5.0	85.8	3
NGC 2903	8.9	15.2	–20.93	65	204	190	7.0	43.5	4
NGC 2976	3.6	3.8	–17.78	65	335	80	3.5	1.4	5
NGC 3031	3.6	11.6	–20.73	59	330	200	6.0	36.4	2
NGC 3198	13.8	13.0	–20.75	72	215	150	6.0	101.7	5
IC 2574	4.0	7.5	–18.11	53	56	70	6.0	14.8	9
NGC 3521	10.7	12.9	–20.94	73	340	210	6.0	80.2	4
NGC 3621	6.6	9.4	–20.05	65	345	140	6.5	70.7	7
NGC 3627	9.3	13.9	–20.74	62	173	133	5.0	8.2	3
NGC 4736	4.7	5.3	–19.80	41	296	120	5.0	4.0	2
DDO 154	4.3	1.2	–14.23	66	230	48	6.5	3.6	10
NGC 4826	7.5	11.4	–20.63	65	121	150	5.0	5.5	2
NGC 5055	10.1	17.4	–21.12	59	102	190	5.0	91.0	4
NGC 6946	5.9	9.8	–20.61	33	243	220	3.0	41.5	6
NGC 7331	14.7	19.6	–21.67	76	168	233	3.0	91.3	3
NGC 7793	3.9	6.0	–18.79	50	290	130	6.0	8.9	7

NOTE. — (1): the name of the galaxy; (2): distance as given in Walter et al. (2008); (3): radius of the major axis of the galaxy at the $\mu_B = 25\,\mathrm{mag\,arcsec^{-2}}$ isophote level, taken from LEDA; (4): absolute *B*-band magnitude as given in Walter et al. (2008); (5): average inclination as given in de Blok et al. (2008); (6): average position angle as given in de Blok et al. (2008); (7): total rotation velocity (used for the normalization of the non-circular motions); (8): adopted spacing of the tilted-rings; (9): H I mass as listed in Walter et al. (2008); (10): morphological type from LEDA

capture most of the non-circular signal, as is described in Section 6.4.1.

The usual description of the apparent velocity, under the assumption of purely circular motion can be retrieved by only including $m = 0$ and $m = 1$ terms in Eq. 1, i.e.,

$$v_{los}(r) = v_{sys}(r) + c_1(r)\cos\psi + s_1(r)\sin\psi, \qquad (2)$$

and by ignoring streaming (radial) motions (i.e., $s_1 = 0$). The circular rotation velocity corresponds therefore to c_1. Note that the dependence on inclination is included in the c_m and s_m terms. For the following discussion it is worthwhile to repeat a few rules of thumb which apply to harmonic decompositions as given in Schoenmakers et al. (1997) and Schoenmakers (1999):

(1) A perturbation of the gravitational potential of order m will cause $m+1$ and $m-1$ harmonics in the velocity field (so an $m = 2$ two-armed spiral component will cause $m = 1$ and $m = 3$ harmonics in the velocity field).

(2) Perturbations in the gravitational potential are independent and can therefore be added. The same holds for velocity perturbations.

(3) The elongation of the potential ϵ_{pot} in the plane of the disk of the galaxy can be calculated at each radius as follows:

$$\epsilon_{pot}\sin 2\varphi_2 = (s_3 - s_1)\frac{1+2q^2+5q^4}{c_1(1-q^4)}, \qquad (3)$$

where $q = \cos i$. The only remaining unknown quantity is φ_2, the unknown angle in the plane of the ring between the minor axis of the elongated ring and the observer.

(4) Velocities induced by a global elongation of the potential will result in a constant offset in $\epsilon_{pot}\sin 2\varphi_2$. Velocities induced by spiral arms occur on much smaller scales, and will therefore only lead to perturbations ("wiggles") around this offset.

(5) If the fitted inclination is close to the intrinsic inclination of the disk, then $c_3 = 0$. Small offsets of a few km s^{-1} result in only small (1-2 degree) inclination offsets.

We use the GIPSY task RESWRI. This task performs a tilted-ring fit assuming circular rotation, creates a model velocity field, subtracts this from the original velocity field, and does a harmonic expansion of the residuals. RESWRI does not down-weight velocities along the minor axis as is usually done in standard rotation curve analysis, and thus emphasizes the non-circular motions. For the width of the annuli (cf. Col (8) of Table 1), we chose half the beam width; neighboring rings are thus not independent.

We calculate the quadratically added amplitude ("power") for each order of the harmonic decomposition using

$$A_1(r) = \sqrt{s_1^2(r)}, \qquad (4)$$

for $m = 1$ (note that c_1 corresponds to the circular velocity and is not included in the calculation of the amplitude of $A_1(r)$), and

$$A_m(r) = \sqrt{c_m^2(r) + s_m^2(r)}, \qquad (5)$$

for $m > 1$.

Additionally, we calculate the quadratically added amplitude of all (i.e., up to $N = 3$) non-circular harmonic components ("total power"):

$$A_r(r) = \sqrt{s_1^2(r) + c_2^2(r) + s_2^2(r) + c_3^2(r) + s_3^2(r)}. \qquad (6)$$

The radial variation of $A_m(r)$ and $A_r(r)$ can be checked for coincidence with visible features in the galaxies. To quantify the power of the non-circular motions in a compact way, we also use $\tilde{A}_m$, the median of $A_m(r)$ defined for each value of m, and $\tilde{A}_r$, the median of $A_r(r)$. We derive two values for $\tilde{A}_m$ and

$\tilde{A}_r$, one for the entire radial range and one for the inner 1 kpc (for those galaxies where sufficiently high signal-to-noise H I is present in the inner parts). The 1 kpc value is not arbitrarily chosen but follows from both the core and cusp models for reasonable choices of halo parameters. The distinction between a cusp and a core can be made most clearly interior to this radius (de Blok et al. 2001a; de Blok 2004), and it is therefore important to separately quantify the non-circular motions in this inner region. Values determined for the entire radial range are thus determined over the entire extent of the H I disk, except for radii where RESWRI failed to converge properly or produce stable results. These radii are usually characterized by very small filling factors and are mostly found in the outer parts of the galaxies.

In the following we will discuss the absolute non-circular motions, as well as the same motions expressed as a fraction of the local and total rotation velocity. The latter is defined as the rotation velocity of the flat part of the rotation curve, or as the maximum rotation velocity if the rotation curve is still rising at the outermost point.

RESWRI creates a residual velocity field which can be used as an indicator for those non-circular motions that are not captured with the harmonic decomposition (as will be shown in Section 6.4.1). As the residual velocity fields contain only values which scatter around a mean zero level, we use *absolute* residual velocity fields in our analysis.

Finally, as mentioned in Schoenmakers (1999), the center position should be kept fixed during the harmonic decomposition. This is because a galaxy which has real, physical c_2 and s_2 terms in its velocity field would, in the case of an unconstrained center position, appear to have a center which drifts in such a way as to minimize these terms. Moreover, rapidly varying center positions at small radii (with offsets larger than the relevant ring radii) have no physical basis.

5. NGC 3198 — A CASE–STUDY

Here we present the derivation of the central position and the harmonic decomposition in some detail for one galaxy. The purpose of this section is to explain the conventions and notations used and demonstrate our methods for one galaxy in our sample. A complete description and discussion of all galaxies from our sample is given in the Appendix.

5.1. *Center estimates*

The 3.6 μm IRAC image of NGC 3198 shows two well-defined spiral arms, emanating from a prominent bulge. The central component has a nuclear point source embedded, which has a counterpart in the radio continuum. The IRAC and continuum centers agree to within $1''$. For ease of reference, and in order to have a compact notation for the center positions, we will in our discussion frequently refer to positions with respect to the pointing center (as listed in Walter et al. 2008). This pointing center has no physical meaning, and merely provides a convenient zero-point, unrelated to any particular choice of the central position. We will refer to the offsets from the pointing center as δX (positive in the direction of decreasing right ascension) and δY (positive in the direction of increasing declination). Both are expressed in arcseconds. Note that we list the full coordinates of all center positions we derive in Table 2 (with the position used for further analysis shown in bold face).

In our determination of the kinematic center of NGC 3198, we start with an unconstrained ROTCUR fit with the position of the radio continuum center (δX= $-1.''4$, δY= $-0.''1$) as an initial estimate. Fig. 1 shows the variation of the center position from the ROTCUR fit over the radial range of the galaxy, together with our best photometric center. As can be seen by the variation of δX and δY, the outer parts ($r \geq 150''$) of NGC 3198 are strongly affected by the spiral arms. For the derivation of the dynamical center, we therefore restrict the averaging of δX and δY to radii with $r \leq 100''$ (indicated in Fig. 1 by the vertical lines at these radii). The dynamical center derived in such a way is offset from the pointing center by $\delta X = -1.''4 \pm 1.''7$, $\delta Y = -0.''2 \pm 2.''1$ (i.e., to the south-east). Averaging δX and δY over all tilted-rings results in a similar center position, though with a larger scatter.

To put our estimates for the center positions in context, we show them together with the IRAC and radio continuum map (where available) overlaid on the central $150'' \times 150''$ of the H I total intensity map (cf. Fig. 2). Also shown are the central positions of the individual tilted-rings. As can be seen, all center positions agree well within the uncertainties and to within one natural-weighted beam (hereafter referred to as "the beam") and we therefore adopt the center as derived from the radio continuum map as our best center position.

5.2. *Harmonic expansion*

The radial distribution of all fitted parameters from the harmonic decomposition of NGC 3198 are shown in Fig. 3. The PA of NGC 3198 rises swiftly within the inner $200''$, and then slowly declines. The inclination varies in the inner parts over a range of about five degrees, but shows a steady increase beyond $r \sim 450''$, indicating that the outer disk is warped. The c_3 term is small for all radii, meaning that the fitted inclination is close to the intrinsic inclination of the disk. Although there is no global offset from zero for c_2 and s_2, they show small deviations at radii coinciding with the locations of spiral arms in the 3.6 μm image of NGC 3198, or in the total H I map presented in Walter et al. (2008). The s_1 and s_3 terms are best described as wiggles caused by spiral arms on top of a slight offset. The amplitudes of all non-circular components (c_2, c_3, s_1, s_2, s_3) are generally only a few $\mathrm{km\,s^{-1}}$.

In Fig. 4, we show derived parameters which were calculated according to Eqs. 3-6. The median amplitudes of the individual harmonic components, derived following Eqs. 4 and 5, are similar in amplitude, ranging from $\tilde{A}_m \sim 2-3$ $\mathrm{km\,s^{-1}}$ (when averaged over the entire radial range), or ≤ 2 percent of $V_{\rm tot}$. For the inner 1 kpc, the amplitudes are even smaller ($\tilde{A}_m < 1.5\,\mathrm{km\,s^{-1}}$). The distribution of $A_r(r)$ (cf. Eq. 6) shows that the amplitude of the non-circular motions is $A_r(r) \leq 8$ $\mathrm{km\,s^{-1}}$ for most radii. The median amplitude is $\tilde{A}_r \sim 4.5\,\mathrm{km\,s^{-1}}$ when averaged over the entire radial range, and $\tilde{A}_r \sim 1.5\,\mathrm{km\,s^{-1}}$ when averaged over the inner 1 kpc only.

The elongation of the potential, $\epsilon_{\rm pot}\sin(2\varphi_2)$, derived according to Eq. 3 is small over most of the radial range, but shows traces of the same spiral arms which cause the variation in, e.g., the s_3 component. Inwards of $r \sim 30''$, the elongation is rather unconstrained — mainly because of the larger uncertainty in the derived inclination, which enters into the uncertainty in $\epsilon_{\rm pot}$ as a fourth power. The weighted mean elongation of the potential is fairly small with $\langle \epsilon_{\rm pot}\sin(2\varphi_2)\rangle = 0.017 \pm 0.020$, and within the uncertainties consistent with zero.

As mentioned in Section 4, RESWRI creates residual velocity fields, which can be used to quantify the signal which

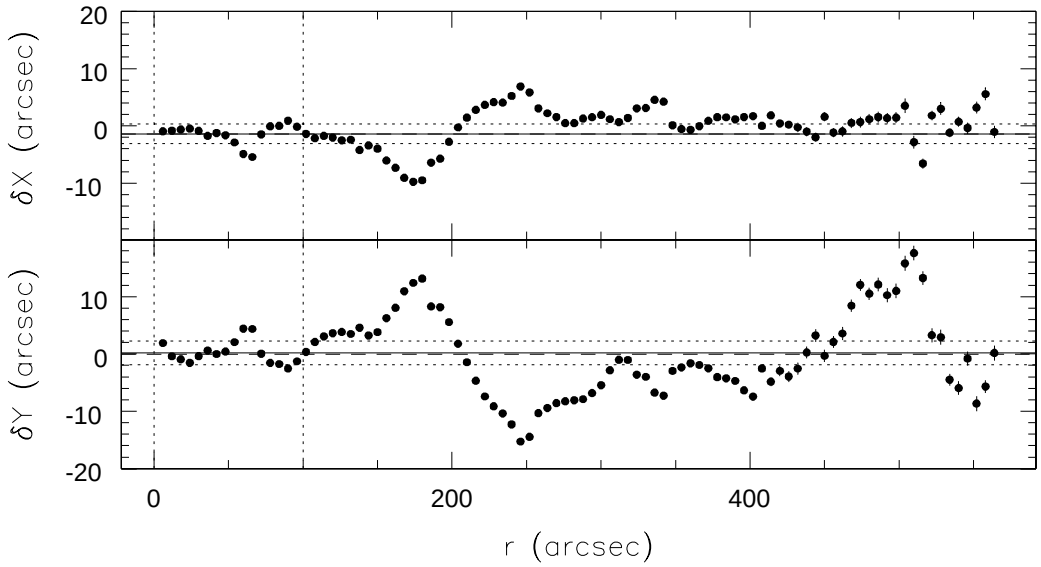

FIG. 1.— Radial variation of the center positions of the individual tilted-rings derived in an unconstrained fit with ROTCUR. The center positions are given as an offset from the pointing center (in arcseconds). The two vertical lines at $r = 0''$ and $r = 100''$ denote the radial range over which the center positions were averaged in order to derive a kinematic center. The resulting kinematic center (together with its standard deviation) is indicated by the black solid (and dotted) lines. Our best center position (in this case from the radio continuum) is indicated by the dashed horizontal line, which is however barely distinguishable from the kinematic estimate because of the good agreement between these two.

was not captured in the harmonic expansion. For NGC 3198, we find a median absolute value of $\sim 2.6\,\mathrm{km\,s^{-1}}$, showing that a harmonic decomposition up to third order is capable of capturing most non-circular motions. This is addressed more fully in Section 6.4.1.

The results from the harmonic decompositions are summarized (for all galaxies) in Table 3 and detailed descriptions for all galaxies are given in Appendix A.

6. RESULTS

In the previous section and in the detailed notes on the individual galaxies in the Appendix, we show how the center positions are derived and present the results of the harmonic decompositions. The different center estimates are summarized in Table 2, where our adopted positions are shown in bold face. The results from the harmonic decomposition are summarized in Table 3.

In this section, we will put these results in context and address some of the astrophysical questions discussed in the Introduction. Section 6.1 will deal with the results of the center estimates, whereas Section 6.2 deals with the results of the harmonic decompositions. In Section 6.3, we compare the latter with predictions from CDM simulations. In Section 6.4, we present and discuss several consistency checks which we applied to test our methods.

6.1. *Quality of the center estimates*

In this section, we discuss the quality and reliability of our center positions. An intrinsically cuspy density profile can be mistaken for a flat, constant-density one, if possible offsets between the kinematic and the photometric center of a galaxy are ignored. Using the photometric center to derive a rotation curve or a mass model in the presence of such an offset will result in a less steep rotation curve and density profile. A potential cusp could then appear as a core-like density profile.

As we have determined the kinematic and photometric centers of the galaxies in our sample, we can directly test if such offsets exist. This is shown in Fig. 6, where we show the offsets between the dynamical and photometric centers for the galaxies in our sample. The offsets are generally less than ~ 0.1 kpc, with only two galaxies reaching offsets of ~ 0.3 kpc.

These results are similar to those derived by Matthews & Gallagher (2002) for a sample of 21 extreme late-type spiral galaxies. They compare the systemic velocites as derived from the rotation curves of these galaxies with the central velocities of the corresponding global HI profiles. For over two-thirds of their sample they find offsets less than 10 km $\mathrm{s^{-1}}$ and from this they conclude that their sample galaxies, despite their late-type, diffuse stellar disks and shallow potentials, do have well-defined centers. A similar comparison of the systemic velocities and central HI profile velocities (measured at 20 percent of the peak level) of our sample galaxies (using the values as listed in Walter et al. 2008 and de Blok et al. 2008) shows a similarly good agreement with an absolute velocity difference $\Delta V = 1.7 \pm 1.7$ km $\mathrm{s^{-1}}$, the largest offset being 6.2 km $\mathrm{s^{-1}}$.

We also show the distribution of offsets between the kinematic and the best (photometric) center estimates for the 15 galaxies in our sample with well-constrained photometric centers. For 13 out of the 15 galaxies shown in Fig. 5, the dynamical center differs by less than the size of one beam from the best (photometric) center — and for 10 galaxies the agreement is even better than half the size of the beam. Only two galaxies (NGC 3627 and NGC 6946) show moderate offsets

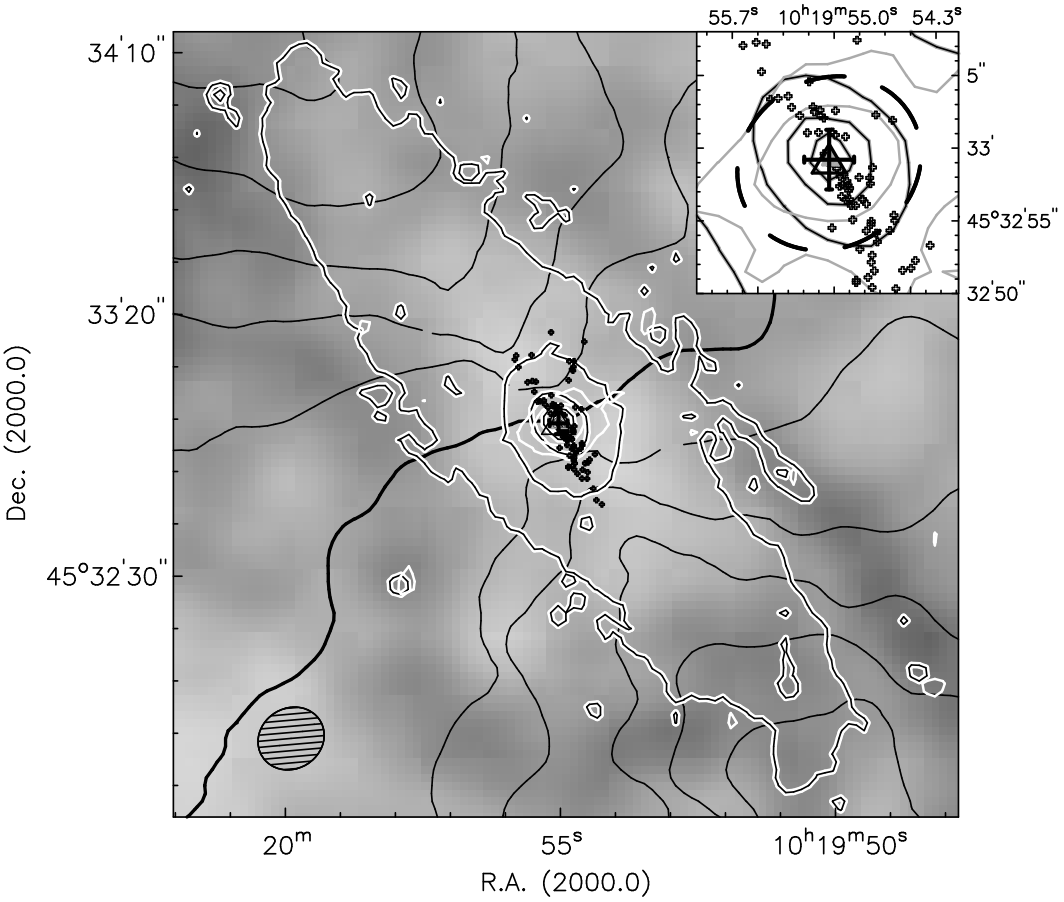

FIG. 2.— This figure shows the inner 150″ × 150″ of NGC 3198. The integrated natural-weighted H I map is shown in grayscales. The beam is indicated in the bottom-left corner. The black contours show iso-velocity contours from the hermite velocity field. The thick black contour is shown at 663 km s^{-1} and represents the systemic velocity given in de Blok et al. (2008). The other velocity contours are spaced by 25 km s^{-1}. The thin black contours overlaid on the thick white contours represent the 3.6 μm IRAC image. They are drawn at 2, 5, 10, 20, and 50 percent of the maximum intensity level. The white contours represent the THINGS radio continuum map, and are drawn at 10, 20, and 50 percent of the peak intensity. The black dots indicate the individual center positions from ROTCUR and the black cross represents the derived dynamical center together with its uncertainty. The derived center from the 3.6 μm image is shown as a gray, filled triangle, whereas the one from the radio continuum is shown as a black, open triangle. **Inset:** To better highlight the different center estimates, we show an inset of the innermost 18″ in the upper-right corner. For clarity reasons we do not show the H I grayscale and velocity field contours here. The contours from the 3.6 μm image are shown in black and are given at the same intensity levels as in the main plot. The same holds for the radio continuum contours, which are shown here in gray. The individual center estimates from ROTCUR are shown as small crosses. In the inset, the beam is indicated by the thick black dashed ellipse and is centered on our best center position.

of between one and two beam sizes. Given that the former galaxy is extremely asymmetric (due to its interactions in the Leo group) and the latter has a low inclination which makes fitting tilted-rings more difficult, these outliers can be understood.

The strength of the agreement we find does depend on how well-constrained the dynamical center estimates are. A tightly constrained kinematic center position which agrees with a well-determined photometric center allows one to draw strong conclusions. A weakly constrained kinematic center less so, as the increased uncertainties allow agreement with a whole range of photometric centers, as long as they are located somewhere near the kinematic center. To test the strength of our conclusions we therefore determine for each galaxy the offsets between the centers of individual tilted-rings and the best center estimate. Because of the sparsely filled rings in the very outer parts, as well as the presence of warps and asymmetries, we restrict this analysis to the data points in the inner half of each galaxy (i.e., those with $r < 0.5\,r_{\rm max}$), with $r_{\rm max}$ as listed in Table 3. In Fig. 7, we show a histogram of the distribution of these offsets in terms of beam size for all galaxies in our sample. Approximately 50 percent of the center positions of the ∼1000 individual tilted-rings differ less than one beam from our best center position. Another 25 percent show an offset between one and two beam sizes and only a small fraction shows large offsets. Note that the center positions of some of the tilted-rings can be affected by the presence of spiral arms and other features. Large offsets for individual rings do therefore not necessarily imply intrinsic offsets between center positions, but need to be regarded within the context of the results for the whole galaxy. The radial variation of the center positions are shown in Fig. 1 for NGC 3198 and in the top panels of Figs. 25-42 for the other galaxies in our sample.

Our results show that for the large majority of the galaxies

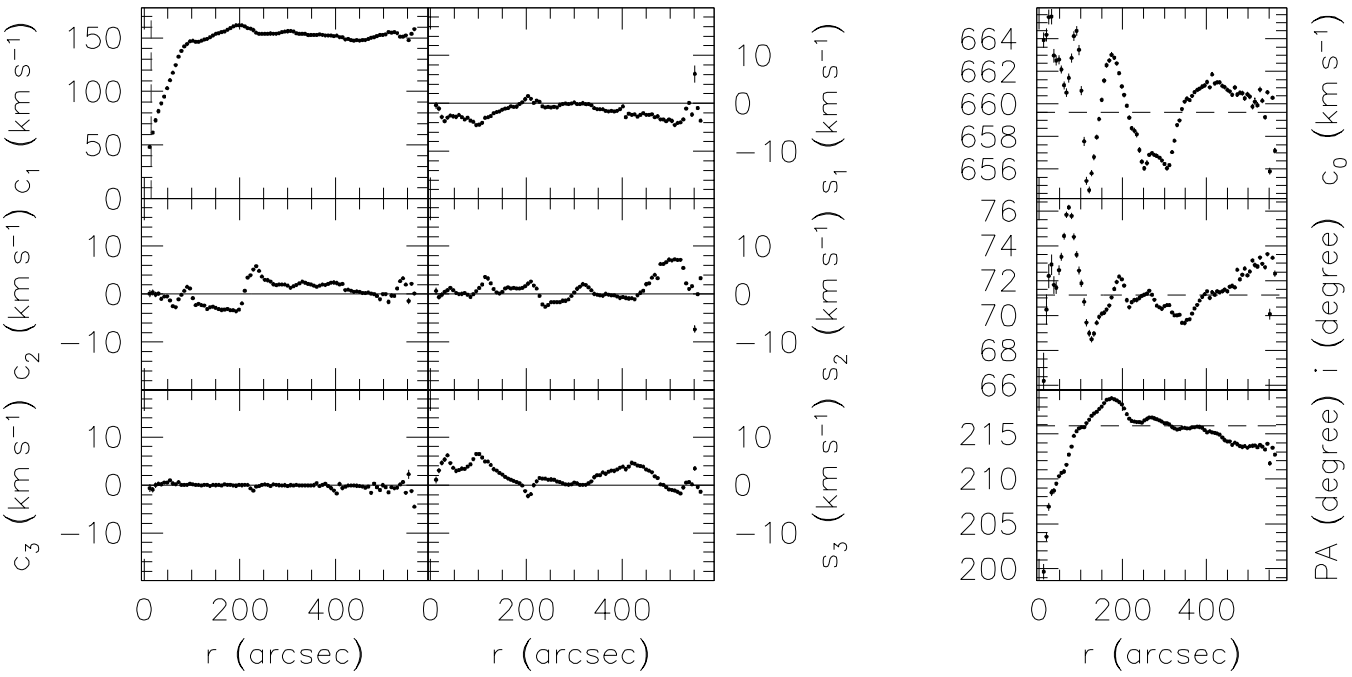

FIG. 3.— **Left:** circular (c_1), and non-circular (c_2, c_3, s_1, s_2, s_3) harmonic components (derived according to Eq. 1), all corrected for inclination and plotted *vs.* radius. The dashed vertical line in the panel showing the distribution of c_1 indicates the radius corresponding to 1 kpc. **Right:** systemic velocity c_0, inclination and position angle, plotted *vs.* radius. The dashed horizontal lines represent the error weighted means. The inclination and position angle are from the tilted-ring fit assuming circular rotation. The error bars shown in all panels of this figure are the formal uncertainties from RESWRI.

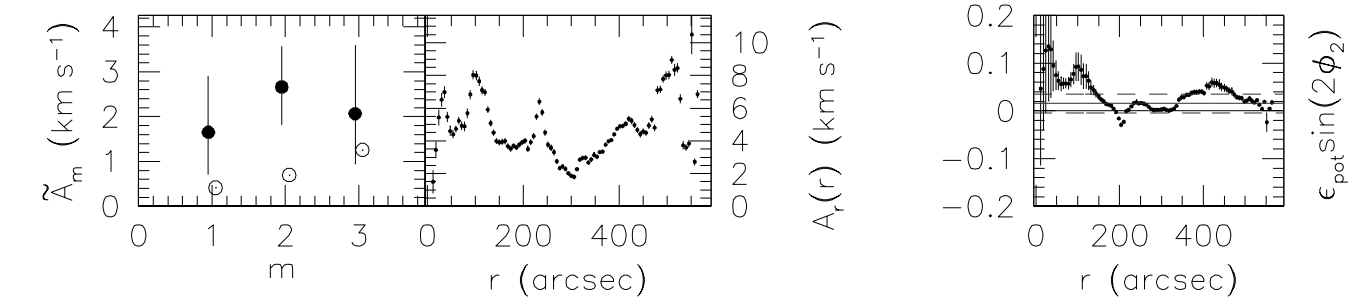

FIG. 4.— **Left:** $\tilde{A}_m$, the median amplitudes of the individual harmonic components, derived following Eqs. 4 and 5, plotted *vs.* harmonic number m. The error bars denote the upper and lower quartile of the distribution of $A_m(r)$. We have calculated the median amplitudes twice: once for the entire radial range (filled circles), and once for the inner 1 kpc (open circles). Note that in the case of NGC 3198, the median for the inner 1 kpc has no error bars, as the inner 1 kpc contains only one data point. **Middle:** $A_r(r)$, the quadratically added amplitude of all non-circular components (derived following Eq. 6) *vs.* radius. The errors were estimated assuming Gaussian error propagation. For most radii, the amplitude is $A_r(r) \leq 8\,\mathrm{km\,s^{-1}}$. **Right:** the radial distribution of the elongation of the potential, $\epsilon_{\rm pot}\sin(2\varphi_2)$, derived according to Eq. 3. The uncertainties are also estimated assuming Gaussian error propagation. The elongation is fairly unconstrained in the inner $\sim 30''$, mainly because of the large uncertainty in the inclination, which enters into the uncertainty of $\epsilon_{\rm pot}$ as a fourth power. The weighted mean elongation (and its standard deviation) are represented by the horizontal dotted (and dashed) lines. The weighted mean elongation of NGC 3198 is $\langle\epsilon_{\rm pot}\sin(2\varphi_2)\rangle = 0.017 \pm 0.020$, and thus consistent with a round potential.

studied here, the photometric and kinematic center positions agree within their uncertainties and also to within a beam. See also Sec. 6.4.4 where we evaluate the impact of a shift in center position on our results.

6.2. *Results of the harmonic decomposition*

Here, we discuss the results of the harmonic decompositions in a more general way. For a description of the results for individual galaxies we refer to Appendix A. Because of the low filling-factor of its velocity field (cf. de Blok et al. 2008), we did not perform a harmonic decomposition for NGC 4826.

In Fig. 8 we show plot the harmonic decomposition results as a function of absolute magnitude, Hubble type and dark matter dominance. In all panels, we distinguish between barred and non–barred galaxies. The Hubble types are listed in Table 1 and the bar classifications are based on NED. The dark matter dominance is expressed as the ratio of total baryonic mass to total dynamical mass $M_{\rm bar}/M_{\rm tot}$. The baryonic mass is calculated using the mass models presented in de Blok et al. (2008), where we have used the Kroupa IMF results (their Table 4). The total dynamical mass is calculated using the radius of the outermost point of the rotation curve and the velocity is taken from Table 1. We note that for NGC 3627 we cannot show $M_{\rm bar}/M_{\rm tot}$ as the non-circular motions in this galaxies were too large for de Blok et al. (2008) to derive

TABLE 2
CENTER POSITIONS FOR THE GALAXIES IN OUR SAMPLE.

Name	kinematic (ROTCUR) center		3.6 μm center		radio continuum center	
	α_{2000} (h m s)	δ_{2000} ($^\circ$ $'$ $''$)	α_{2000} (h m s)	δ_{2000} ($^\circ$ $'$ $''$)	α_{2000} (h m s)	δ_{2000} ($^\circ$ $'$ $''$)
NGC 925	**02 27 16.5±0.7**	**+33 34 43.5±4.1**	02 27 17.0[a]	+33 34 42.4[a]	...	...
NGC 2366	**07 28 53.9±0.7**	**+69 12 37.4±7.8**	07 28 53.4[a]	+69 12 40.3[a]	...	...
NGC 2403	**07 36 51.1±0.9**	**+65 36 02.9±4.2**	07 36 51.0[a]	+65 36 02.1[a]	...	...
NGC 2841	09 22 02.6±0.1	+50 58 35.3±1.0	09 22 02.7	+50 58 35.4	**09 22 02.7**	**+50 58 35.4**
NGC 2903	09 32 10.0±0.2	+21 30 02.5±2.2	09 32 10.1	+21 30 04.9	**09 32 10.1**	**+21 30 04.3**
NGC 2976	09 47 14.9±0.5	+67 55 00.8±1.4	**09 47 15.3**	**+67 55 00.0**	...	...
NGC 3031	09 55 33.5±0.6	+69 03 52.0±3.9	09 55 33.3	+69 03 54.6	**09 55 33.1**	**+69 03 54.7**
NGC 3198	10 19 55.0±0.2	+45 32 59.2±2.0	10 19 55.0	+45 32 59.1	**10 19 55.0**	**+45 32 58.9**
IC 2574[b]	**10 28 27.5±2.7**	**+68 24 58.7±10.4**	...	...	...	...
NGC 3521	11 05 48.6±0.1	–00 02 08.4±1.4	**11 05 48.6**	**–00 02 09.2**	...	...
NGC 3621	11 18 16.6±0.2	–32 48 48.5±6.5	**11 18 16.5**	**–32 48 50.9**	...	...
NGC 3627	11 20 15.3±0.2	+12 59 22.7±4.8	11 20 15.0	+12 59 29.2	**11 20 15.0**	**+12 59 29.6**
NGC 4736	12 50 53.0±0.2	+41 07 14.2±2.0	12 50 53.1	+41 07 11.9	**12 50 53.0**	**+41 07 13.2**
DDO 154	**12 54 05.9±0.2**	**+27 09 09.9±3.4**	...	...	...	...
NGC 4826	12 56 43.6±0.1	+21 40 59.3±0.8	12 56 43.6	+21 40 59.2	**12 56 43.6**	**+21 41 00.3**
NGC 5055	13 15 49.3±0.2	+42 01 45.1±1.3	13.15 49.3	+42 01 45.5	**13 15 49.2**	**+42 01 45.3**
NGC 6946	20 34 52.4±0.6	+60 09 11.8±5.9	20 34 52.3	+60 09 14.3	**20 34 52.2**	**+60 09 14.4**
NGC 7331	22 37 04.1±0.1	+34 24 54.4±2.2	**22 37 04.1**	**+34 24 56.5**	...	...
NGC 7793	23 57 49.8±0.2	–32 35 25.2±2.1	**23 57 49.7**	**–32 35 27.9**	...	...

NOTE. — The uncertainties in the ROTCUR centers are given in units of seconds (for right ascension) and arcseconds (for declination). The center position chosen for subsequent analysis is shown in bold face.

[a]Derived by fitting ellipses with ELLFIT

[b]The center coordinates of IC2574 were derived using a bulk velocity field cleared of non-circular motions as presented in Oh et al. (2008)

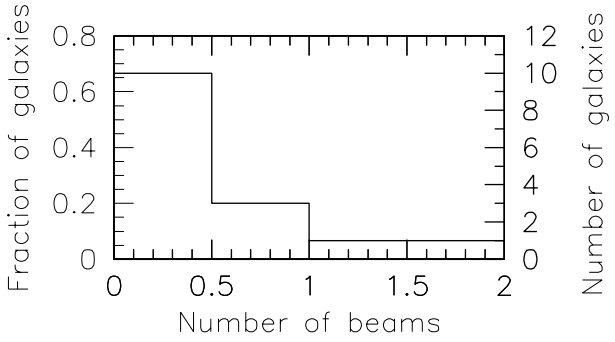

FIG. 5.— The histogram shows the offset between the dynamical and the best (photometric) center for those 15 galaxies in our sample which have a well-constrained photometric center position. The offset is shown in terms of beam size. For 13 of the 15 galaxies, the different center estimates agree to within one beam (typical beam size: $\sim 10''$), showing that there is no indication for a genuine and general offset between kinematic and photometric centers in our sample.

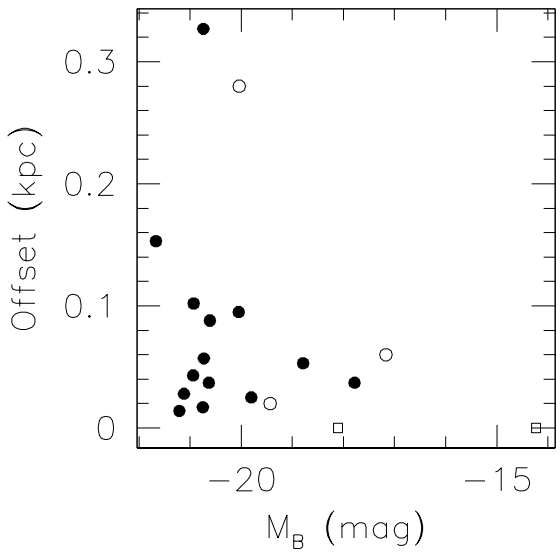

FIG. 6.— Offsets between kinematic and photometric centers of the galaxies in our sample. Filled circles indicate galaxies for which we adopted the position of the photometric center as our best center estimate. Open circles represent galaxies for which we adopted the position of the kinematic center. Open squares indicate the two galaxies for which no reliable photometric center position could be derived.

a mass model.

In the upper panels of Fig. 8, we show the results for $\tilde{A}_r$. It is clear that the magnitude of the non-circular motions decreases towards lower luminosities and later Hubble types (top panel of Fig. 8). A more tentative trend is visible for $M_{\rm bar}/M_{\rm tot}$ where the dark-matter dominated galaxies have on average the lowest non-circular motions. When these motions are expressed as a fraction of $V_{\rm tot}$, we see that their contribution is roughly independent of luminosity, Hubble type or dark matter dominance (Fig. 8, middle panel). For 16 out of the 18 galaxies, the non-circular contribution is smaller than 6 percent of $V_{\rm tot}$ and it has a mean value (averaged over the entire sample) of 4.5 percent. Both in the top and in the middle panel of Fig. 8, barred galaxies do not stand out, except for NGC 3627. This is different if we look only at the non-circular motions in the inner 1 kpc (Fig. 8, bottom panel). As expected, most barred galaxies have rather high non-circular motions in the innermost region. Note that some galaxies are not shown in these diagrams, as we have no data above a detection limit of 3 σ in their inner 1 kpc.

As a comparison, we also calculated the amplitude of the non-circular motions within the inner 2, 3, 4, and 5 kpc, using two different methods. The approach shown in Fig. 9 measures the non-circular motions by taking the median of the $A_r(r)$ values within rings of 1 kpc width, as measured over

TABLE 3
DERIVED QUANTITIES FROM THE HARMONIC DECOMPOSITIONS.

Name	$\tilde{A}_r$ km s^{-1}	$\tilde{A}_{r,1\mathrm{kpc}}$ km s^{-1}	$\tilde{A}_r/V_{\mathrm{max}}$ percent	$\langle\epsilon_{\mathrm{pot}}\sin(2\varphi_2)\rangle$	$\tilde{M}_{\mathrm{resid}}$ km s^{-1}	r_{max} ″
(1)	(2)	(3)	(4)	(5)	(6)	(7)
NGC 925	$6.30^{+1.63}_{-1.74}$	$9.45^{+0.64}_{-2.98}$	5.5	0.000 ± 0.046	3.0	282
NGC 2366	$2.94^{+1.46}_{-1.24}$	$1.17^{+0.12}_{-0.40}$	5.3	0.004 ± 0.066	2.4	252
NGC 2403	$4.03^{+1.39}_{-1.33}$	$2.60^{+0.59}_{-0.48}$	3.0	-0.022 ± 0.025	2.9	950
NGC 2841	$6.71^{+4.67}_{-3.54}$	···	2.6	-0.001 ± 0.014	3.5	635
NGC 2903	$6.10^{+3.64}_{-2.68}$	$13.55^{+2.70}_{-6.18}$	3.2	0.006 ± 0.028	2.8	602
NGC 2976	$2.81^{+0.75}_{-1.18}$	$2.18^{+0.77}_{-0.55}$	3.5	-0.010 ± 0.018	2.1	147
NGC 3031	$9.14^{+2.08}_{-3.05}$	···	4.6	0.007 ± 0.045	3.0	840
NGC 3198	$4.49^{+1.00}_{-0.91}$	1.50[a]	3.0	0.016 ± 0.020	2.6	565
IC 2574	$3.75^{+1.78}_{-1.04}$	$1.36^{+0.49}_{-0.06}$	5.4	0.012 ± 0.047	2.7	505
NGC 3521	$8.80^{+3.45}_{-4.62}$	$3.12^{+12.67}_{-1.77}$	4.2	0.017 ± 0.019	4.5	415
NGC 3621	$3.36^{+1.00}_{-1.09}$	$5.52^{+0.94}_{-3.21}$	2.4	0.002 ± 0.022	2.3	600
NGC 3627	$28.49^{+10.91}_{-5.87}$	···	14.7	-0.024 ± 0.071	3.6	165
NGC 4736	$10.01^{+3.63}_{-2.14}$	$8.79^{+1.87}_{-1.56}$	8.3	-0.055 ± 0.149	2.5	400
DDO 154	$1.61^{+0.42}_{-0.65}$	$1.43^{+0.14}_{-0.53}$	3.4	0.024 ± 0.033	1.2	325
NGC 5055	$4.11^{+1.61}_{-0.73}$	$8.38^{+11.14}_{-2.60}$	2.2	-0.003 ± 0.025	3.1	450
NGC 6946	$7.28^{+3.12}_{-2.88}$	···	3.6	0.004 ± 0.069	3.4	420
NGC 7331	$5.94^{+1.65}_{-1.21}$	···	2.6	-0.003 ± 0.017	4.2	297
NGC 7793	$5.08^{+0.90}_{-1.67}$	$3.41^{+0.64}_{-0.48}$	3.9	-0.067 ± 0.085	2.2	372
Sample mean	**6.72**	**4.80**	**4.5**	**0.011**	**2.9**	
Sample rms	**5.91**	**3.99**	**2.9**	**0.013**	**0.8**	

NOTE. — (1): the name of the galaxy; (2): $\tilde{A}_r$, the median of the quadratically added amplitude of the non-circular motions, averaged over the entire radial range. Uncertainties indicate the lower and upper quartile; (3): same as (2) but averaged over the inner 1 kpc only; (4): the percentage the non-circular motions contribute to the total rotation velocity; (5): the weighted mean elongation of the potential; (6): the median of the absolute residual velocity field after the harmonic decomposition; (7): maximum radius for the averaging of $\tilde{A}_r$ and ϵ_{pot}. The bottom two rows contain the mean values and their rms over the entire sample. For ϵ_{pot}, this value represents the weighted mean.

[a]This value has no upper or lower quartile as the inner 1 kpc of NGC 3198 contain only one data point.

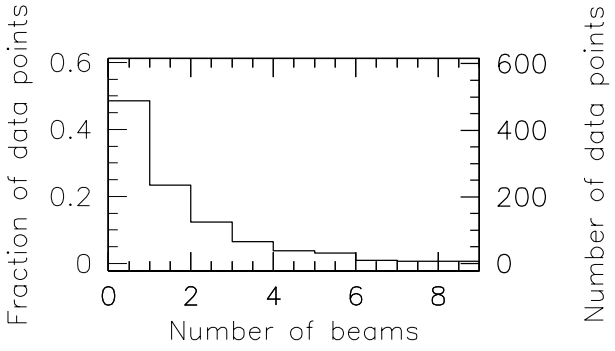

FIG. 7.— The histogram shows (for all galaxies in our sample) the offset between the individual tilted-ring center estimates and the corresponding best center position in terms of beam size. The typical beam size is $\sim 10''$ (this corresponds to a physical size of 170 pc – 750 pc). Only tilted-rings inwards of $r = 0.5\,r_{\mathrm{max}}$ were included. The histogram demonstrates that our dynamical center estimates are well-constrained and in good agreemend with the photometric center positions.

radii $0 < r < 1$ kpc, $1 < r < 2$ kpc, ..., $4 < r < 5$ kpc. Our second approach, shown in Fig. 10, simply increases the radial range over which the amplitudes are averaged ($0 < r < 1$ kpc, $0 < r < 2$ kpc, ..., $0 < r < 5$ kpc). In both cases, we have divided our sample into three absolute magnitude bins. It is apparent from the two figures that galaxies with low luminosity have the lowest amplitudes of non-circular motions in the inner parts, regardless of the chosen method. Since the approach shown in Fig 9 measures the non-circular motions more locally than the method shown in Fig 10, it is also more affected by local features like effects of star formation. For instance, the two relatively high amplitudes in the $4 < r < 5$ kpc bin of the bottom panel of Fig. 9 belong to IC 2574 and NGC 2366. The former has a supergiant shell at those radii (see Walter et al. 1998), whereas the latter has a large star forming region in its outer parts (see Oh et al. 2008 for an in-depth analysis of the small-scale non-circular motions in these two galaxies). The only other low-luminosity galaxy in our sample which extends out to 5 kpc radius (DDO 154) is completely quiescent in contrast. In the analysis shown in Fig. 10, these effects have "averaged out", due to the larger area used for the averaging.

However, no matter how they are binned, in absolute terms the measured amplitudes of the non-circular motions are

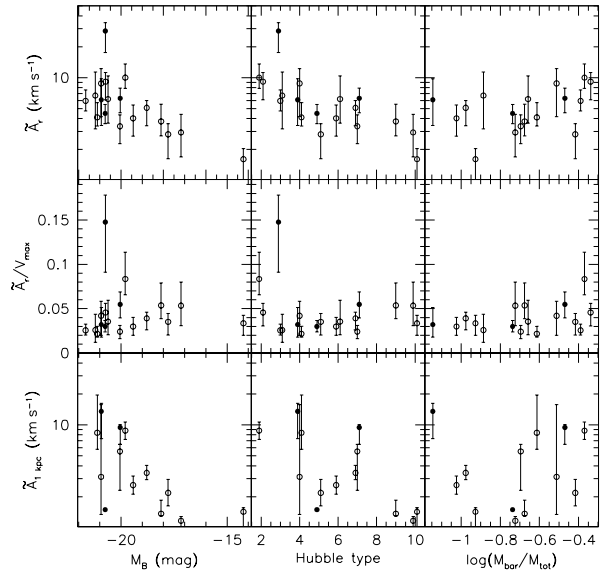

FIG. 8.— The non-circular motions measured in different ways for our entire sample. Barred galaxies are shown as filled circles, non–barred as open circles. **Top panel:** Median amplitude of the non-circular motions ($\tilde{A}_r$) on a logarithmic scale *vs*. absolute magnitude (left), Hubble type (center) and baryonic to total mass ratio (right). Error bars indicate the upper and lower quartile of the radial distribution of $\tilde{A}_r$. **Middle panel:** The percentage the non-circular motions contribute to the total rotation velocity. **Bottom panel:** Like top panel, but the averaging was restricted to the inner 1 kpc of the galaxies. Note that for five galaxies, the data do not show significant amounts of H I in the inner kpc, and they are therefore not shown in the two bottom panels.

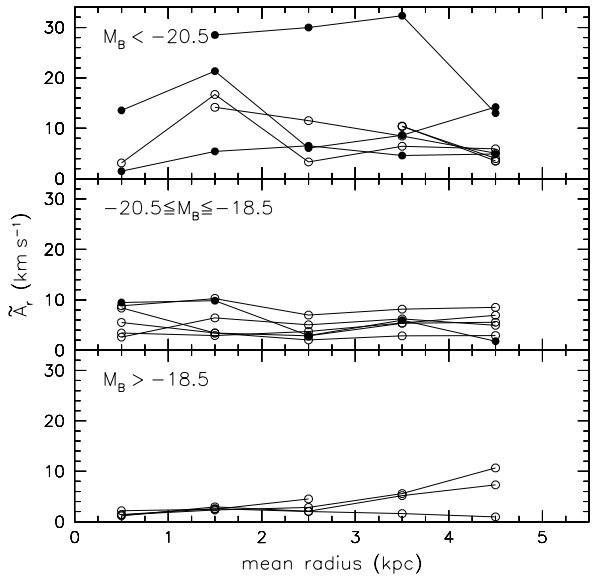

FIG. 9.— The amplitude of the non-circular motions within rings of 1 kpc width (i.e., $0 < r < 1$ kpc, $1 < r < 2$ kpc, ..., $4 < r < 5$ kpc) for each galaxy (if data available). All measurements of a specific galaxy are connected by a line. Filled symbols correspond to barred galaxies, open symbols to non–barred galaxies. We divide the plot into three subpanels. The top panel contains all galaxies with $M_B < -20.5$, the middle panel those with $-20.5 \leq M_B \leq -18.5$ and the bottom panel all galaxies with $M_B > -18.5$.

small. In order to account for the different rotation velocities, we have normalized the amplitudes shown in Figs. 9 and 10 by the local rotation velocity. The results are shown in Figs. 11 and 12, respectively. For the large majority of the galaxies in our sample, the non-circular motions in the inner few kpc contribute approximately ten percent to the local rotation velocity. Three galaxies (NGC 925, NGC 2903, and IC 2574) contain non-circular motions larger than 20 percent of the local rotation velocity. For NGC 925 and NGC 2903, it is likely that the large non-circular motions are associated with their stellar bars, especially as Figs. 11 and 12 indicate that large non-circular motions in the central parts are predominantly found in barred galaxies. For IC 2574, the large ratio between non-circular and circular motions is mainly caused by the slow rise of its rotation curve in the inner kpc. Over the same radial range the *absolute* non-circular motions are generally less than 2.3 km s^{-1}.

We will now discuss the elongation of the potential (see Fig. 13). The weighted average elongation and its standard deviation are $\langle \epsilon_{\rm pot} \sin(2\varphi_2) \rangle = 0.011 \pm 0.013$. This elongation and the individual elongation measurements still contain an unknown viewing angle φ_2, for which one can apply a statistical correction by dividing the elongation by the expectation value of φ_2, $2/\pi$ (middle panel of Fig. 13). The average, corrected elongation is $\langle \epsilon_{\rm pot} \rangle = 0.017 \pm 0.020$, i.e., consistent with a round potential.

The elongations show neither a trend with absolute magnitude, nor with Hubble type, nor with dark matter dominance. If the influence of the disk decreases with baryonic mass, and if the dark matter halos are indeed tri-axial (or more precisely, have an elliptical potential distortion in the plane of their disk, cf. Hayashi & Navarro 2006), one would expect the measured elongations to increase with decreasing (baryonic)

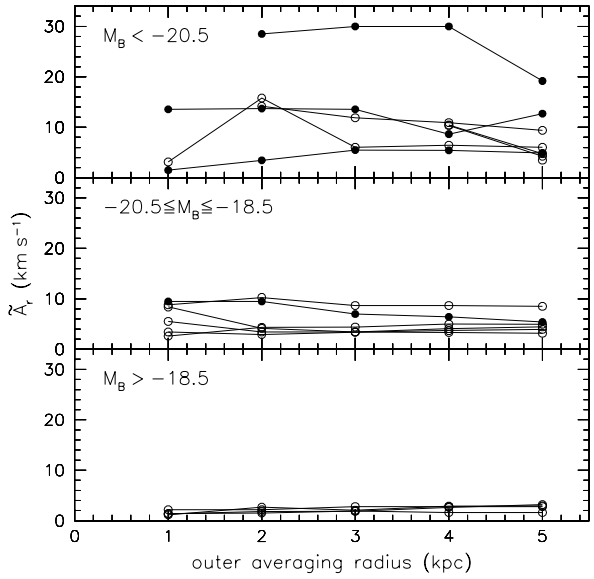

FIG. 10.— Like Fig. 9, but the amplitude of the non-circular motions were averaged within rings of increasing radius (i.e., $0 < r < 1$ kpc, $0 < r < 2$ kpc, ..., $0 < r < 5$ kpc). As the region over which the non-circular motions are averaged increases outwards, the amplitudes shown are less affected by local features such as the effects of star formation.

mass. However, no such trend is seen in our data.

One explanation could be that the baryons dominate the total potential sufficiently so that the elongation values we measure are really the elongations of the potentials of the baryonic disks. As the self-interaction (dissipation) of the (gas component) baryons tends to circularize the orbits, any (kinemati-

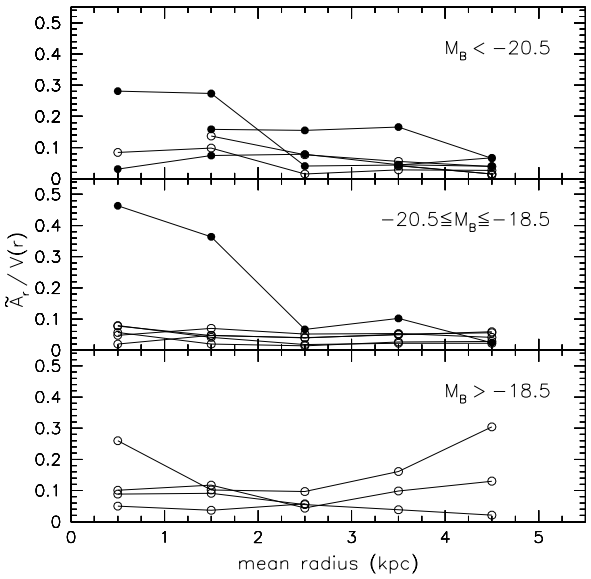

FIG. 11.— Like Fig. 9, but the amplitudes of the non-circular motions are normalized by the local rotation velocity. Except for a few galaxies, the non-circular motions in the inner few kpc have an amplitude of ~ 10 percent of the local rotation velocity, irrespective of the galaxies' luminosity. Only three galaxies have non-circular motions in their centers which are larger than 20 percent of the local rotation velocity. Note also that large non-circular motions (in relative terms) are predominantly found in barred galaxies.

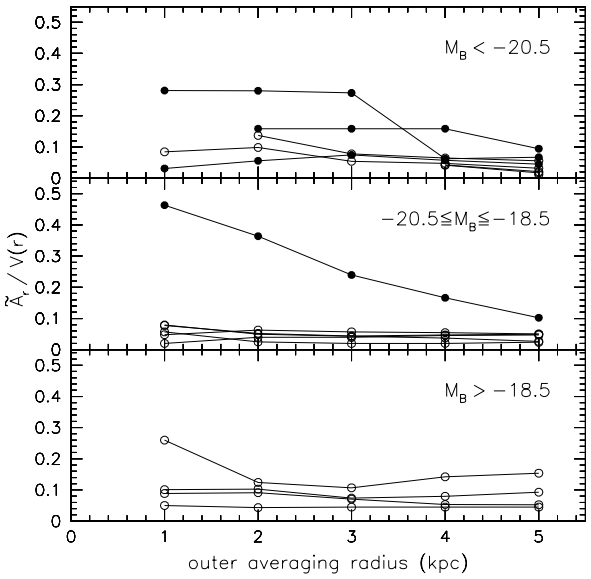

FIG. 12.— Like Fig. 10, but the amplitudes of the non-circular motions are normalized by the local rotation velocity. Analogous to Fig. 10, the increasing region for the averaging of the non-circular motions causes the amplitudes to be somewhat less affected by local features such as the effects of star formation.

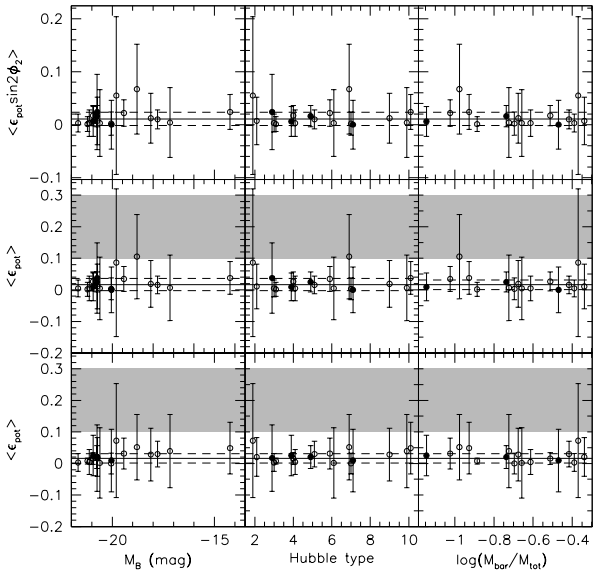

FIG. 13.— **Top panel:** Elongation of the potential *vs.* absolute magnitude (left), Hubble type (center) and baryonic to total mass ratio (right). The horizontal lines represent the weighted mean and its standard deviation ($\langle\epsilon_{\rm pot}\sin(2\varphi_2)\rangle = 0.011 \pm 0.013$). Barred galaxies are shown as filled circles, non–barred ones as open circles. The distribution of $\langle\epsilon_{\rm pot}\sin(2\varphi_2)\rangle$ shows neither a trend with luminosity, nor with Hubble type. **Middle panel:** Like top panel, but a statistical correction for the unknown viewing angle was applied to the individual elongation measurements and to their mean and standard deviation. The hatched area indicates the CDM predictions by Hayashi & Navarro (2006). The elongations of the large majority of the galaxies shown here are systematically lower (rounder) than what is predicted by CDM simulations, although the measurements for some galaxies have large enough error bars to make them marginally consistent with the lower end of the CDM predictions. **Bottom panel:** Like middle panel, but we averaged the elongation of the potential not over the entire radial range, but only out to $r < 0.5\,r_{\rm max}$ ($r_{\rm max}$ is the maximum radius to which our analysis extends). This has generally only little effect on the individual elongation measurements. The mean value has not changed ($\langle\epsilon_{\rm pot}\rangle = 0.017 \pm 0.020$ *vs.* $\langle\epsilon_{\rm pot}\rangle = 0.016 \pm 0.015$) and we therefore do not see an indication that the elongation of the potentials increase inwards.

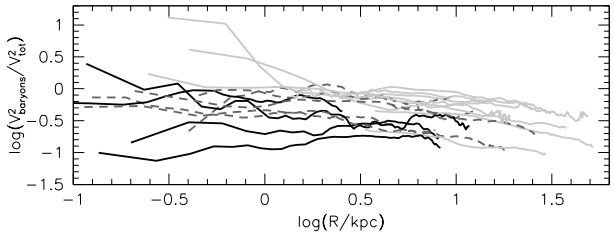

FIG. 14.— The radial distribution of $M_{\rm bar}/M_{\rm tot}$ in the THINGS galaxies, derived from the Kroupa IMF mass models presented in de Blok et al. (2008). Light-gray full curves represent galaxies brighter than M_B = 20.5. Dashed, dark-gray curves show galaxies with $-20.5 \leq M_B < -18.5$. Black curves show galaxies fainter than M_B = –18.5.

cal) traces of the tri-axial dark matter potential would thus be wiped out. With a variation in total $M_{\rm bar}/M_{\rm tot}$ of close to an order of magnitude, this means the circularization process ought to be extremely effective over a large range of mass ratios. The relevant quantity here, however, is not the *total* dark matter dominance but the *local* one. We therefore show in Fig. 14 a measure for the local ratio of $M_{\rm bar}/M_{\rm tot}$ as a function of radius, based on the Kroupa IMF mass models presented in de Blok et al. (2008). We see that whilst for the high luminosity galaxies the local importance of dark matter and baryons in the inner parts is roughly equal, it drops to values of $M_{\rm bar}/M_{\rm tot} \sim 1/3$ in the outer parts. For the low luminosity galaxies the importance of the baryons is, however, close to an order of magnitude lower. Again, this implies that the circularization process should be equally effective over a large range in local mass ratios, and already manage to wipe out the tri-axial signal when the baryons contribute only ~ 10 percent

to the local mass. Note that in the above we have assumed that both stars and gas contribute to the circularization process. It is however likely that only the gas component is relevant, as the stars will not necessary dissipate as strongly. If this is the case, the relevant quantity is the $M_{\rm gas}/M_{\rm tot}$ ratio, which can be another order of magnitude lower than the $M_{\rm bar}/M_{\rm tot}$ ratios discussed here. In summary, attributing the circular potentials to dissipation requires that the circularization process is already effective when the baryons contribute only ~ 10 percent to the total mass. Alternatively, the dissipation may not be relevant at such low mass ratios, in which case the potentials are truly round. The well-known dark matter dominance of LSB galaxies may imply that similar conclusions also hold for them; direct and equally detailed measurements should provide the additional information needed to draw definitive conclusions.

6.3. *Comparison with predictions from simulations*

One of the clearest outcomes of simulations is that CDM halos are triaxial (e.g., Frenk et al. 1988; Dubinski 1994; Hayashi et al. 2004; Moore et al. 2004; Kasun & Evrard 2005; Hayashi & Navarro 2006; Hayashi et al. 2007). We compare our results with predictions based on cosmological ΛCDM simulations. Hayashi et al. (2004); Hayashi & Navarro (2006) present models where they use an elliptical distortion of the gravitational potential (mimicking a tri-axial halo) to explain the observed solid-body rotation curves of dwarfs and LSB galaxies within a CDM context. This distortion affects the orbits and thus also the rotation curve. In this picture, the major axis rotation curve depends on the viewing angle of the elliptical distortion. This viewing angle can be chosen in such a way that the major axis rotation curve in the elliptical potential looks identical to what it would have been, had the gas been on circular orbits (i.e., without elliptical distortion and without non-circular motions). It would therefore hide the presence of the disturbance due to tri-axiality and look like a solid-body rotation curve.

However, even if the angle is adjusted in such a way, the minor axis rotation curve of the tri-axial case would still show large streaming motions. These can be up to 15 percent of the total rotation velocity. As we show in Fig. 8, the observed non-circular motions in our sample are generally much smaller and never reach 15 percent of the total rotation (see also the minor-axis position-velocity diagrams presented in de Blok et al. 2008). In Figs. 11 and 12, we normalize the amplitudes of the non-circular motions by the *local* (circular) rotation velocity. At a radius of 1 kpc, Hayashi et al. (2004) report non-circular motions as high as 50 percent of the local rotation velocity. At smaller radii, the contribution of the non-circular motions is even larger. The results shown in Figs. 11 and 12, however, show that for the large majority of the galaxies in our sample, the non-circular motions are only as high as ten percent of the local rotation velocity. Only in one barred galaxy (NGC 925) do the non-circular motions reach an amplitude close to 50 percent of the local rotation velocity in the inner 1 kpc. The dwarf galaxies (bottom panels of Figs. 11 and 12) are of most interest here, as these galaxies are the ones most dominated by dark matter. The non-circular motions in three out of the four dwarfs in our sample (NGC 2366, NGC 2976, and DDO 154) contribute only ten percent to the local rotation velocity. Therefore, the non-circular motions in these galaxies do not significantly affect the mass models presented in de Blok et al. (2008) and Oh et al. (2008) and preclude the possibility that their cored density profiles (cf. aforementioned papers) are intrinsic cuspy profiles which have been artificially flattened by large non-circular motions. The non-circular motions in the inner kpc of IC 2574 amount to ~ 26 percent of the local rotation velocity, a factor two smaller than predicted in Hayashi et al. (2004). We refer to Oh et al. (2008) for a full treatment of the IC 2574 non-circular motions.

The gravitational potential in the simulations of Hayashi & Navarro (2006) is elongated in the inner parts as $\langle\epsilon_{\rm pot}\rangle = 0.2 \pm 0.1$ (their Fig. 3). All but two of the individual elongation measurements presented here are systematically lower than those predictions and consistent with a round potential, although some have large enough error bars to make them marginally consistent with the lower end of the CDM predictions.

If DM halos do indeed have an elliptical distortion in their inner parts, we would expect to find higher elongations there. To test this idea, we have also determined the elongations of the potential by using only data out to $r = 0.5\,r_{\rm max}$ (bottom panel of Fig. 13). The individual elongation measurements do not change significantly if averaged only over the inner half of the disk. Their weighted mean ($\langle\epsilon_{\rm pot}\rangle = 0.016 \pm 0.015$) is not significantly different from the value obtained by averaging over the entire disk ($\langle\epsilon_{\rm pot}\rangle = 0.017 \pm 0.020$) and we therefore see no indication that the gravitational potential is more elongated towards the center of the galaxies.

One caveat relating to the above discussion is that the model presented in Hayashi & Navarro (2006) consists of only a dark matter component, while real galaxies contain baryons as well. Baryonic processes, such as dissipation in the gas component might affect the dynamics within the visible disk of observed galaxies, thus invalidating any comparisons. As we showed in Sect. 6.2, however, in some of the galaxies in our sample the local baryon to total mass ratio is only ~ 10 percent. If dissipation or circularization of the orbits affects the results found for our galaxies, this implies that the 10 percent of baryons are able to wipe out the dynamical signature of the 90 percent of dark matter. If dissipation is really this efficient, it would also imply that analyses of, e.g., the scatter in the Tully-Fisher relation in order to put limits on the tri-axiality of haloes (e.g., Franx & de Zeeuw 1992) are only relevant for the elongations of the baryonic disks, but not for those of dark matter haloes. In summary, unless the effects of baryonic dissipation are extremely efficient, it is difficult to reconcile the tri-axialities found in simulations with those inferred for the low-luminosity galaxies in our sample. More extensive observations and more detailed simulations ought to show whether these results hold for the general disk galaxy population.

6.4. *Consistency Checks*

In this section, we compare the results of our harmonic decomposition with the traditional tilted-ring analysis presented in de Blok et al. (2008). Additionally, we present quality controls which show the limitations of our methods, test and validate our current results as well as indicate room for improvement.

6.4.1. ROTCUR *vs.* RESWRI*: residual velocity fields*

Here, we compare the residual velocity fields from the ROTCUR analysis by de Blok et al. (2008) with those from our analysis with RESWRI. As mentioned in Section 4, the residual velocity fields are derived by subtracting a model using the final parameter estimates from the original data. For both

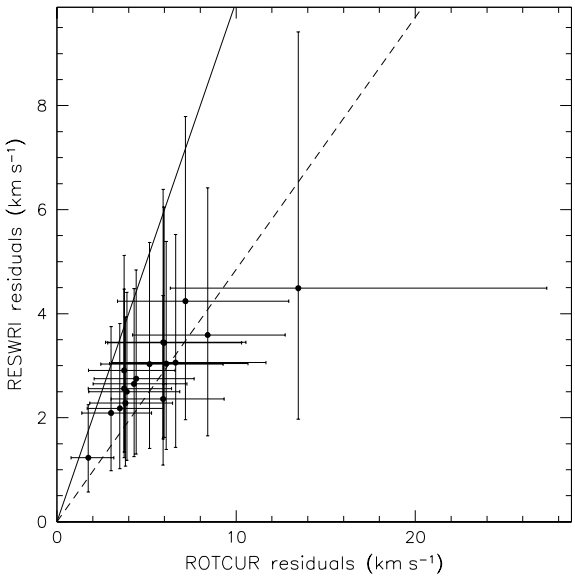

FIG. 15.— Median of the absolute residual velocity field from the rotation curve analysis of de Blok et al. (2008) *vs.* the one from the harmonic decomposition presented in this paper. The error bars indicate the lower and upper quartile, the solid line represents a one–to–one relation, and the dashed line the unweighted least square fit through the data points. The residuals in the traditional ROTCUR analysis are all larger than those from the RESWRI fits, as expected. The difference between the solid line and dashed line is due to the non-circular motions quantified in this paper.

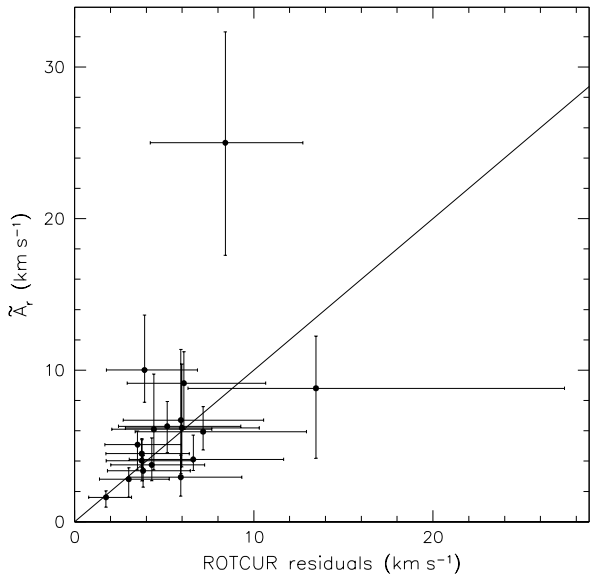

FIG. 16.— Median of the absolute residual velocity field from the rotation curve analysis in de Blok et al. (2008) *vs.* $\tilde{A}_r$, the median of the (radially averaged) quadratically added amplitudes of the non-circular motions quantified in this paper. The error bars indicate the lower and upper quartile. Galaxies with large residuals in the ROTCUR fits show generally also larger non-circular motions. The outlier in the upper part of the panel is NGC 3627, which shows large non-circular motions, but only moderate residuals in the ROTCUR analysis by de Blok et al. (2008).

types of residual fields, we calculate the median and the lower and upper quartile of the *absolute* residual velocity fields. These are compared in Fig. 15. It is clear that all galaxies have larger residuals in the ROTCUR analysis than they have in the RESWRI analysis. This is of course to be expected, given that ROTCUR considers only circular motion, while RESWRI also takes non-circular motions into account. Nevertheless, it is a quality test which shows that our results are behaving in the expected manner. The largest median amplitude of the residual RESWRI velocity fields is 4.5 $\mathrm{km\,s^{-1}}$ (for NGC 3521). The average value of the sample is 2.9 $\mathrm{km\,s^{-1}}$, which clearly shows that a harmonic expansion up to third order is capable of capturing the majority of the non-circular motions in most galaxies.

Looking at Fig. 15, it becomes also clear that galaxies with small ROTCUR residuals also have small RESWRI residuals. Small ROTCUR residuals, however, indicate that a model assuming circular rotation already provides a good approximation. Therefore, it is to be expected that these galaxies show only small non-circular motions. This expectation is tested in Fig. 16, where we plot the median values of the absolute residual velocity fields from de Blok et al. (2008) *vs.* the median amplitudes $\tilde{A}_r$ of the non-circular motions from our harmonic decompositions. Most galaxies are located near the line of unity, showing that our expectation is indeed correct. The only real outlier in Fig. 16 is NGC 3627, which is clearly offset from all other galaxies as it has — despite its large non-circular motions ($\tilde{A}_r \sim 28.5\ \mathrm{km\,s^{-1}}$) — only moderate ROTCUR residuals. The results for the other galaxies, however, show that even a simple model considering only circular rotation can fit most galaxies quite well. These small residuals therefore demonstrate (independently from our RESWRI analysis) that non-circular motions are generally small.

6.4.2. *Making prior assumptions during the* RESWRI *runs*

The rotation curves of all galaxies in our sample were derived and discussed in detail by de Blok et al. (2008). The general procedure for the derivation of a rotation curve includes keeping some parameters fixed in the tilted-ring fits, thus reducing the number of free parameters for each individual fit with ROTCUR. In the current analysis we derive all tilted-ring parameters in a single fit with all parameters left free and do not attempt to correct for the motions induced by, e.g., star formation or spiral arms. Thus, it is expected that the tilted-ring parameters derived by us differ to some extent from the ones derived by de Blok et al. (2008). In order to check this and to estimate the impact on our results, we compare the derived values for our unconstrained harmonic decompositions with those from constrained decompositions with PA and i fixed to the final values from de Blok et al. (2008). We apply this test to two representative galaxies, NGC 3198 and DDO 154, a spiral galaxy and a dwarf irregular.

In the case of NGC 3198 (Fig. 17), most values agree remarkably well between the constrained and the unconstrained fit. Because de Blok et al. (2008) have assumed a constant inclination in the inner parts (in order to compensate for effects caused by spiral arms), our unconstrained values differ slightly in this region. Note though that the effect on the rotation curve is negligible. Fixing the inclination has the predictable effect that the c_3 term reaches values of a few $\mathrm{km\,s^{-1}}$ as this term tries to compensate for the effect the spiral arms have on the velocity field. The impact of this, however, is minor, as one can see in the distribution of $A_r(r)$ and $\tilde{A}_m$ as well as in the negligible difference in the derived rotation velocity. The elongation of the potential is also largely unaffected by constraining i and PA. The only noticeable differences are the different-sized error bars. As the inclination contributes

to the fourth power to the error of the elongation of the potential, the error bars are naturally smaller in the case of a fixed inclination.

For DDO 154 (Fig. 18), the differences between the harmonic components of the two decompositions are generally of the order of $\sim 1\,\mathrm{km\,s^{-1}}$. The inclinations in the unconstrained fit differ inwards of $r \approx 80''$ from the ones in the constrained fit. This is because of the close-to solid-body rotation of DDO 154, which makes the simultaneous determination of the correct inclination difficult. The impact on the results, even in the inner $80''$, is nevertheless small. For instance, the derived rotation velocities are indistinguishable between the two decompositions. This shows that the magnitude of the non-circular motions is not very sensitive to small variations in PA or inclination.

6.4.3. *Hermite vs. Intensity weighted mean VF*

Hermite velocity fields differ from intensity weighted mean (IWM) velocity fields when dealing with asymmetric (i.e., non-Gaussian) profiles. It was noted, e.g., by de Blok et al. (2008), that hermite velocity fields better reproduce the velocity of the peak intensity of the profile, as their analytical function includes an h_3 (skewness) term (see, e.g., van der Marel & Franx 1993). For a detailed overview of the different types of velocity fields we refer to the discussion in de Blok et al. (2008).

As we are using the hermite velocity fields, an investigation of how using IWM velocity fields affects our analysis, if at all, is warranted. We perform unconstrained harmonic decompositions with RESWRI using identical initial conditions on the hermite and on the IWM velocity fields of NGC 3198 and DDO 154. The results are summarized in Figs. 19 and 20, respectively. As small differences between the two decompositions are visible, it is clear that how a velocity field is created does play a role in the analysis. A close inspection of the radial variation of the various quantities shown in both figures indicates that the radial variations are more pronounced in the case of the hermite velocity field. The choice of the velocity field construction method has, however, little impact on the derived quantities (see, e.g., bottom panels of Figs. 19 and 20), and therefore does not change our conclusions in any significant way.

6.4.4. *Decomposition under the assumption of an incorrect center*

In this section, we test the influence of an incorrect center position on our results. As test candidates, we have chosen one galaxy where the position of the center is very well-defined (NGC 2841), and one where the center is less obvious (NGC 2366). For both galaxies, we deliberately shift the center positions used in RESWRI by $2''$, $4''$, $6''$, and $10''$ along their major and minor axes. The results of the most extreme cases ($10''$ offsets, i.e., approximately the beam size) are compared with the results from our best center positions in Figs. 21-24.

For NGC 2366, the effect of an incorrectly chosen center is small, irrespective of whether the center is shifted along the major (Fig. 21) or along the minor (Fig. 22) axis. For offsets along the major (minor) axis, the median amplitude of the non-circular motions increases from $\tilde{A}_r \sim 3\,\mathrm{km\,s^{-1}}$ for our best center position to $\tilde{A}_r \sim 3.5\,\mathrm{km\,s^{-1}}$ ($\tilde{A}_r \sim 4\,\mathrm{km\,s^{-1}}$). Our results for the dwarf galaxy NGC 2366 are therefore unaffected by small offsets in the center position, indicating that for a rotation curve showing close-to solid-body rotation, a modest offset from the true center position is not crucial for the analysis presented here.

For NGC 2841, the situation is different. A $10''$ offset along the major axis (Fig. 23) already increases the median amplitude of the non-circular motions from $\tilde{A}_r \sim 7\,\mathrm{km\,s^{-1}}$ to $\tilde{A}_r \sim 12\,\mathrm{km\,s^{-1}}$. In the case of an offset along the minor axis (Fig. 23), the increment is even larger ($\tilde{A}_r \sim 25\,\mathrm{km\,s^{-1}}$).

Note that the difference in the harmonic components is mostly to be found in the $m = 2$ term. This is to be expected, as a galaxy will appear kinematically lopsided if a center offset from the dynamical center is chosen for the harmonic decomposition. Also note that, as expected, it is the cosine coefficient c_2 which shows the largest amplitude in the case of an offset along the major axis, and the sine coefficient s_2 in the case of an offset along the minor axis.

For NGC 2841 — a galaxy with a steep and subsequently flat rotation curve — our results are sensitive to the chosen center position and an offset center would clearly show itself by increased non-circular motions. But this example is of course rather contrived, as for galaxies like NGC 2841, the center is usually so well-defined that uncertainties of $10''$ as modeled here are unlikely to occur within the THINGS sample.

We have shown that the results of a harmonic decomposition of galaxies like NGC 2841 (i.e., having a steep rotation curve) are sensitive to offsets in the galaxies' center position. For NGC 2366, i.e., a dwarf galaxy showing close-to solid-body rotation, our results are mostly insensitive to small offsets in the center position. The less well-defined center for NGC 2366 does therefore not affect our results of that galaxy.

7. SUMMARY AND CONCLUSIONS

We have analyzed H I velocity fields of 19 THINGS disk and dwarf galaxies at the currently best available spatial and spectral resolution. The observations, data reduction and analysis of all these galaxies were done in an identical and homogeneous manner (Walter et al. 2008; de Blok et al. 2008). We have determined the center positions of these 19 galaxies by comparing the kinematic center estimates with those from the radio continuum and/or NIR data.

We have derived reliable center positions and show that most galaxies in our sample do not exhibit significant offsets between their kinematic and their optical centers. For 18 out of 19 galaxies from our sample, we have performed a harmonic decomposition of their velocity fields with the aim of quantifying the amount of non-circular motions and deriving a lower limit for the elongation of the potential.

Our results show that in the (large) majority of our sample galaxies, the effects of non-circular motions are small, irrespective of whether these non-circular motions are measured in the inner few kpc or over the entire radial range. Within our sample, the average amplitude of the non-circular motions is $\tilde{A}_r = 4.8 \pm 4.0\,\mathrm{km\,s^{-1}}$ for the inner 1 kpc and $\tilde{A}_r = 6.7 \pm 5.9\,\mathrm{km\,s^{-1}}$ when averaged over the entire radial range. High non-circular motions in the inner parts of the galaxies are mostly found in barred, and/or luminous galaxies. The galaxies in our sample least dominated by baryonic matter (i.e., the low luminosity galaxies) show the smallest non-circular motions in the sample, especially in the inner parts, thus not showing the streaming motions one would associate with elliptical distortions or tri-axial halos.

The inner few kpc of the large majority of the galaxies in our sample contain non-circular motions of the order of ten

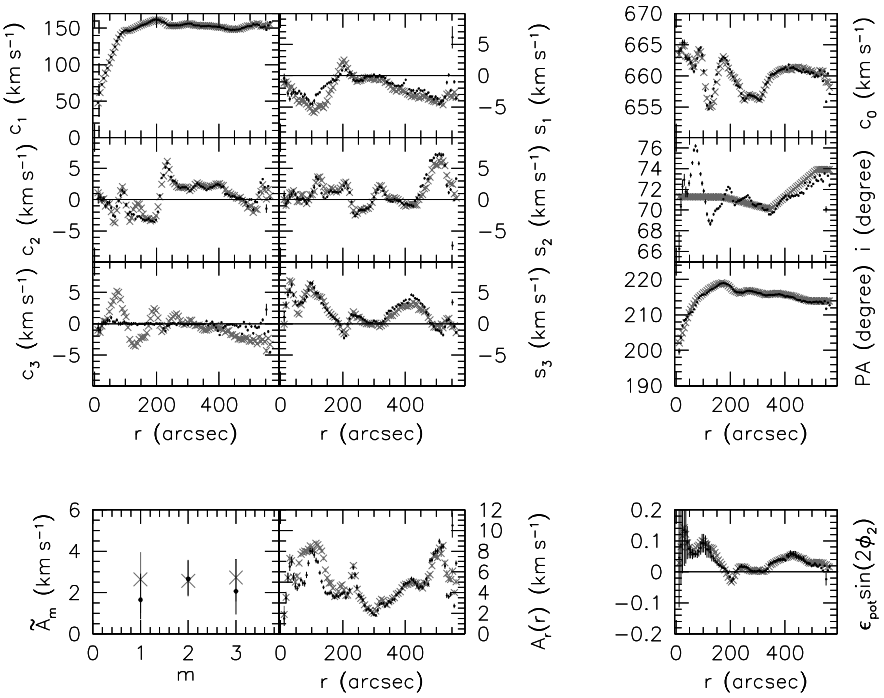

FIG. 17.— The results of the unconstrained (black dots) and constrained (gray crosses) harmonic decomposition of NGC 3198. For the constrained fit, the inclination and position angle were fixed to the values from de Blok et al. (2008). The layout of the figure is identical to that of Figs. 3 and 4, except that we do not show any weighted means in the panels on the right-hand side. The parameters that are plotted in this figure are defined in Sec. 5. The constant inclination in the inner parts of NGC 3198 cause a non-zero c_3 term which results in slightly higher non-circular motions in the inner parts.

percent of the local rotation velocity. Averaged over our sample, the median amplitude of the non-circular motions in the inner 1 kpc is 8 ± 3 percent of the local rotation velocity. For three out of the four dwarf galaxies in our sample, the amplitudes of the non-circular motions amount to (at most) ten percent of the local rotation velocity.

Whether the non-circular motions are expressed in absolute terms or if they are normalized by the local rotation velocity does not affect the conclusions: the amount of non-circular motions detected in the majority of our galaxies is significantly smaller than what is expected from CDM simulations and they are far too small to "hide a cusp in a core" as proposed, e.g., by Hayashi & Navarro (2006).

The average elongation of the gravitational potential and its scatter, both statistically corrected for the unknown viewing angle φ_2, is $\langle \epsilon_{pot} \rangle = 0.017 \pm 0.020$. This is significantly lower than the predictions from cosmological simulations. The individual elongation measurements show that the large majority of the galaxies in our sample have elongation measurements which are systematically below the CDM predictions. The elongation of all galaxies in our sample is consistent with a round potential, although some galaxies have large enough uncertainties to make them also (marginally) consistent with the lower end of the predicted range for CDM halos. We therefore see no indication for a significant tri-axiality within the H I disks of the THINGS galaxies.

CT gratefully acknowledges the help and support from Ralf-Jürgen Dettmar. The work of CT is supported by the German Ministry for Education and Science (BMBF) through grant 05 AV5PDA/3. The work of WJGdB is based upon research supported by the South African Research Chairs Initiative of the Department of Science and Technology and National Research Foundation. EB gratefully acknowledges financial support through an EU Marie Curie International Reintegration Grant (Contract No. MIRG-CT-6-2005-013556). This research has made use of the NASA/IPAC Extragalactic Database (NED) which is operated by the Jet Propulsion Laboratory, California Institute of Technology, under contract with the National Aeronautics and Space Administration. We acknowledge the usage of the HyperLeda database (http://leda.univ-lyon1.fr).

REFERENCES

Battaglia, G., Fraternali, F., Oosterloo, T., & Sancisi, R. 2006, A&A, 447, 49
Braun, R., Walterbos, R. A. M., Kennicutt, Jr., R. C., & Tacconi, L. J. 1994, ApJ, 420, 558
Capuzzo-Dolcetta, R., Leccese, L., Merritt, D., & Vicari, A. 2007, ApJ, 666, 165
de Blok, W. J. G. 2004, in IAU Symposium, Vol. 220, Dark Matter in Galaxies, ed. S. Ryder, D. Pisano, M. Walker, & K. Freeman, 69
de Blok, W. J. G. 2005, ApJ, 634, 227
de Blok, W. J. G., & Bosma, A. 2002, A&A, 385, 816
de Blok, W. J. G., Bosma, A., & McGaugh, S. 2003, MNRAS, 340, 657
de Blok, W. J. G., McGaugh, S. S., Bosma, A., & Rubin, V. C. 2001a, ApJ, 552, L23
de Blok, W. J. G., McGaugh, S. S., & Rubin, V. C. 2001b, AJ, 122, 2396
de Blok, W. J. G., Walter, F., Brinks, E., Trachternach, C., Oh, S.-H., & Kennicutt, Jr., R. C. 2008, submitted to AJ
Dubinski, J. 1994, ApJ, 431, 617
Franx, M., & de Zeeuw, T. 1992, ApJ, 392, L47
Frenk, C. S., White, S. D. M., Davis, M., & Efstathiou, G. 1988, ApJ, 327, 507
Gentile, G., Burkert, A., Salucci, P., Klein, U., & Walter, F. 2005, ApJ, 634, L145
Gentile, G., Salucci, P., Klein, U., & Granato, G. L. 2007, MNRAS, 375, 199
Gentile, G., Salucci, P., Klein, U., Vergani, D., & Kalberla, P. 2004, MNRAS, 351, 903

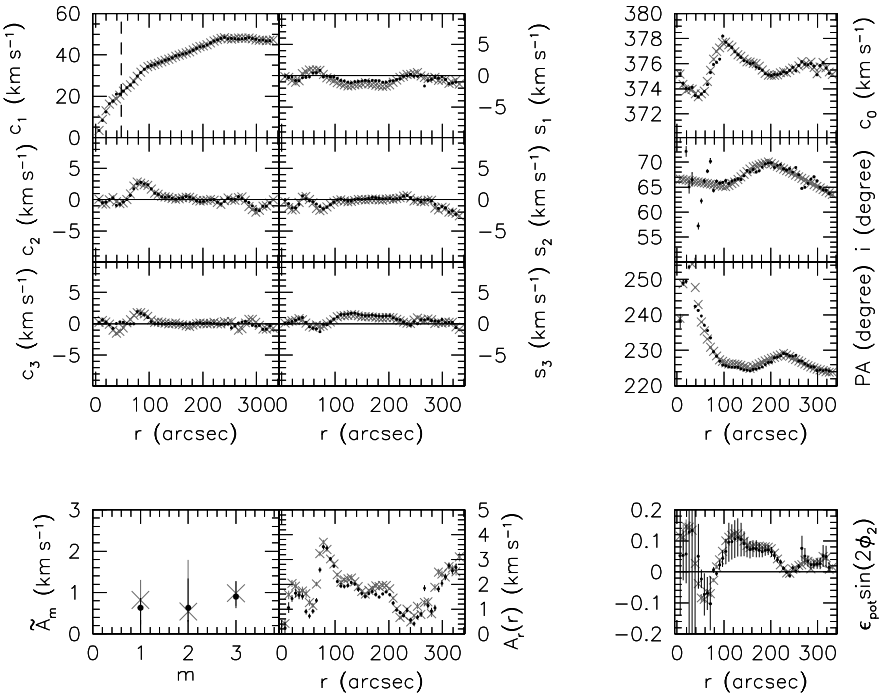

FIG. 18.— Like Fig. 17 but for DDO 154. The differences between the two decompositions are mostly negligible. The close-to solid-body rotation of DDO 154 makes a determination of the inclination in the inner parts (in an unconstrained fit) more difficult. The impact of the less well-constrained *i* is, however, small.

Hayashi, E., & Navarro, J. F. 2006, MNRAS, 373, 1117

Hayashi, E., Navarro, J. F., Jenkins, A., Frenk, C. S., Power, C., White, S. D. M., Springel, V., Stadel, J., Quinn, T., & Wadsley, J. 2004, ArXiv Astrophysics e-prints

Hayashi, E., Navarro, J. F., & Springel, V. 2007, MNRAS, 248

Kasun, S. F., & Evrard, A. E. 2005, ApJ, 629, 781

Kennicutt, Jr., R. C., Armus, L., Bendo, G., Calzetti, D., Dale, D. A., Draine, B. T., Engelbracht, C. W., Gordon, K. D., Grauer, A. D., Helou, G., Hollenbach, D. J., Jarrett, T. H., Kewley, L. J., Leitherer, C., Li, A., Malhotra, S., Regan, M. W., Rieke, G. H., Rieke, M. J., Roussel, H., Smith, J.-D. T., Thornley, M. D., & Walter, F. 2003, PASP, 115, 928

Kuzio de Naray, R., McGaugh, S. S., & de Blok, W. J. G. 2008, ApJ, 676, 920

Kuzio de Naray, R., McGaugh, S. S., de Blok, W. J. G., & Bosma, A. 2006, ApJS, 165, 461

Maoz, D., Filippenko, A. V., Ho, L. C., Macchetto, F. D., Rix, H.-W., & Schneider, D. P. 1996, ApJS, 107, 215

Marchesini, D., D'Onghia, E., Chincarini, G., Firmani, C., Conconi, P., Molinari, E., & Zacchei, A. 2002, ApJ, 575, 801

Matthews, L. D., & Gallagher, III, J. S. 2002, ApJS, 141, 429

McGaugh, S. S., & de Blok, W. J. G. 1998, ApJ, 499, 41

Moore, B., Kazantzidis, S., Diemand, J., & Stadel, J. 2004, MNRAS, 354, 522

Navarro, J. F., Frenk, C. S., & White, S. D. M. 1996, ApJ, 462, 563

—. 1997, ApJ, 490, 493

Oh, S.-H., de Blok, W. J. G., Walter, F., Brinks, E., & Kennicutt, Jr., R. C. 2008, submitted to AJ

Rhee, G., Valenzuela, O., Klypin, A., Holtzman, J., & Moorthy, B. 2004, ApJ, 617, 1059

Schoenmakers, R. H. M. 1999, PhD thesis, Univ. Groningen

Schoenmakers, R. H. M., Franx, M., & de Zeeuw, P. T. 1997, MNRAS, 292, 349

Simon, J. D., Bolatto, A. D., Leroy, A., & Blitz, L. 2003, ApJ, 596, 957

Simon, J. D., Bolatto, A. D., Leroy, A., Blitz, L., & Gates, E. L. 2005, ApJ, 621, 757

Spano, M., Marcelin, M., Amram, P., Carignan, C., Epinat, B., & Hernandez, O. 2008, MNRAS, 383, 297

Spergel, D. N., Bean, R., Doré, O., Nolta, M. R., Bennett, C. L., Dunkley, J., Hinshaw, G., Jarosik, N., Komatsu, E., Page, L., Peiris, H. V., Verde, L., Halpern, M., Hill, R. S., Kogut, A., Limon, M., Meyer, S. S., Odegard, N., Tucker, G. S., Weiland, J. L., Wollack, E., & Wright, E. L. 2007, ApJS, 170, 377

Swaters, R. A., Madore, B. F., van den Bosch, F. C., & Balcells, M. 2003a, ApJ, 583, 732

Swaters, R. A., Verheijen, M. A. W., Bershady, M. A., & Andersen, D. R. 2003b, ApJ, 587, L19

Valenzuela, O., Rhee, G., Klypin, A., Governato, F., Stinson, G., Quinn, T., & Wadsley, J. 2007, ApJ, 657, 773

van der Hulst, J. M., Terlouw, J. P., Begeman, K. G., Zwitser, W., & Roelfsema, P. R. 1992, in Astronomical Society of the Pacific Conference Series, Vol. 25, Astronomical Data Analysis Software and Systems I, ed. D. M. Worrall, C. Biemesderfer, & J. Barnes, 131

van der Marel, R. P., & Franx, M. 1993, ApJ, 407, 525

Walter, F., Brinks, E., de Blok, W. J. G., Bigiel, F., Kennicutt, Jr., R. C., & Thornley, M. 2008, submitted to AJ

Walter, F., Kerp, J., Duric, N., Brinks, E., & Klein, U. 1998, ApJ, 502, L143+

Wong, T., Blitz, L., & Bosma, A. 2004, ApJ, 605, 183

Zackrisson, E., Bergvall, N., Marquart, T., & Östlin, G. 2006, A&A, 452, 857

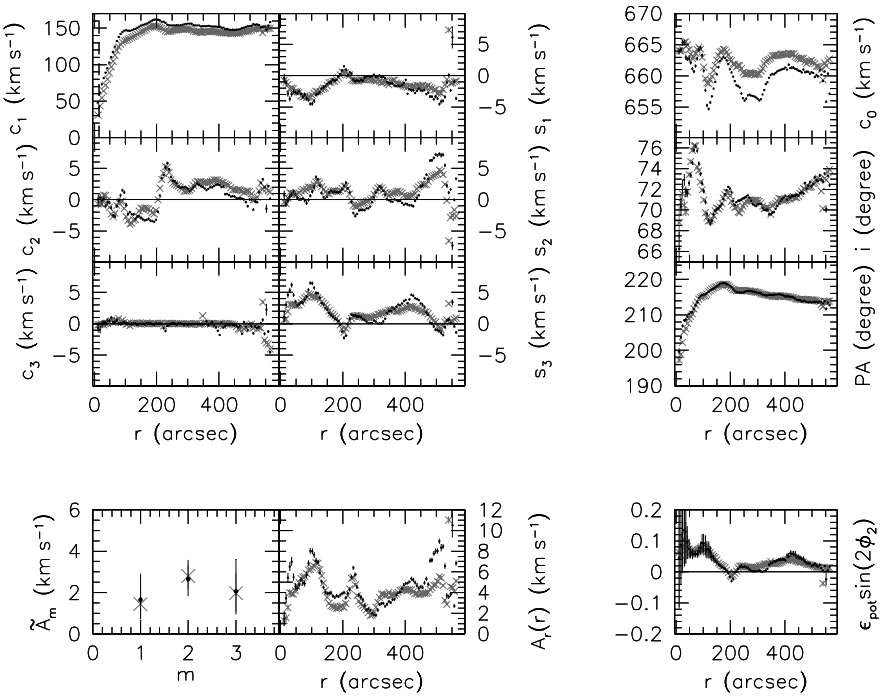

FIG. 19.— Harmonic analysis of NGC 3198 using the hermite velocity field (black dots) and the intensity weighted mean velocity field (gray crosses). The layout of the figure is identical to that of Figs. 3 and 4, except that we do not show any weighted means in the panels on the right-hand side. The differences between the derived quantities are small. The radial variation of the harmonic components seems, however, more pronounced in the hermite velocity field.

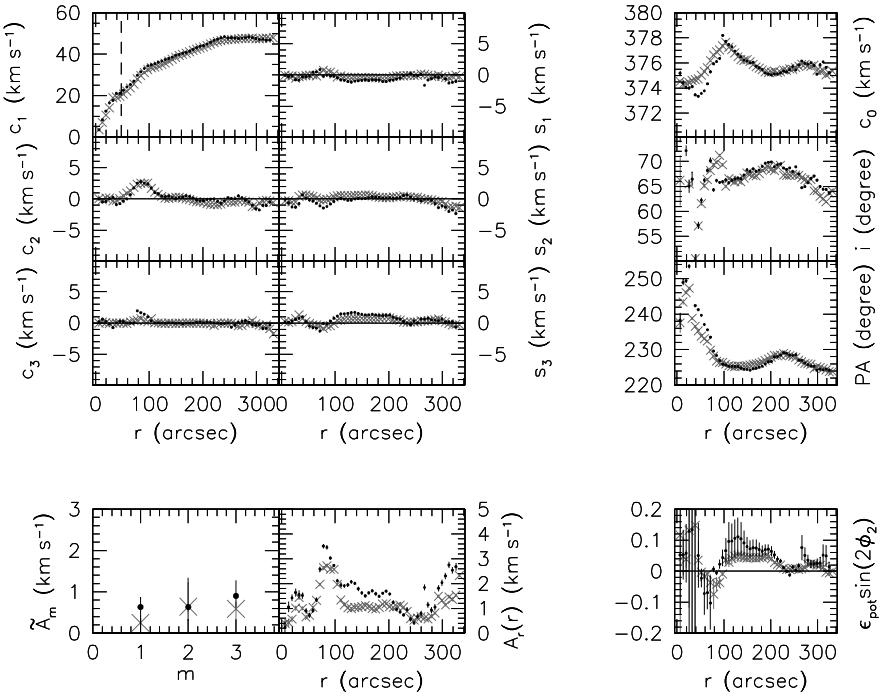

FIG. 20.— Like Fig. 19 but for DDO 154.

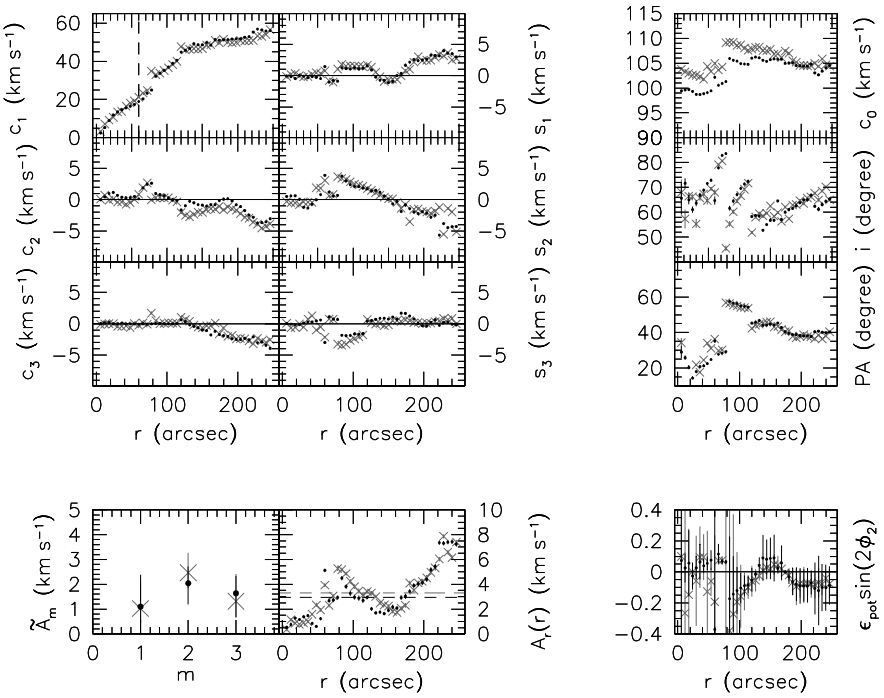

FIG. 21.— Harmonic analysis of NGC 2366 using our best center position (black) and a center position, offset by 10″ along the major axis (gray). The layout of the figure is identical to that of Figs. 3 and 4, except that we do not show any weighted means in the panels on the right-hand side. The difference between the two decompositions is marginal. The offset center causes the median amplitude of the non-circular motions (dashed line in the panel showing the distribution of $A_r(r)$) to increase from $\tilde{A}_r \sim 3\,\mathrm{km\,s^{-1}}$ to $\tilde{A}_r \sim 3.5\,\mathrm{km\,s^{-1}}$, showing that a small offset along the major axis has no significant effect on the derived quantities in the case of NGC 2366.

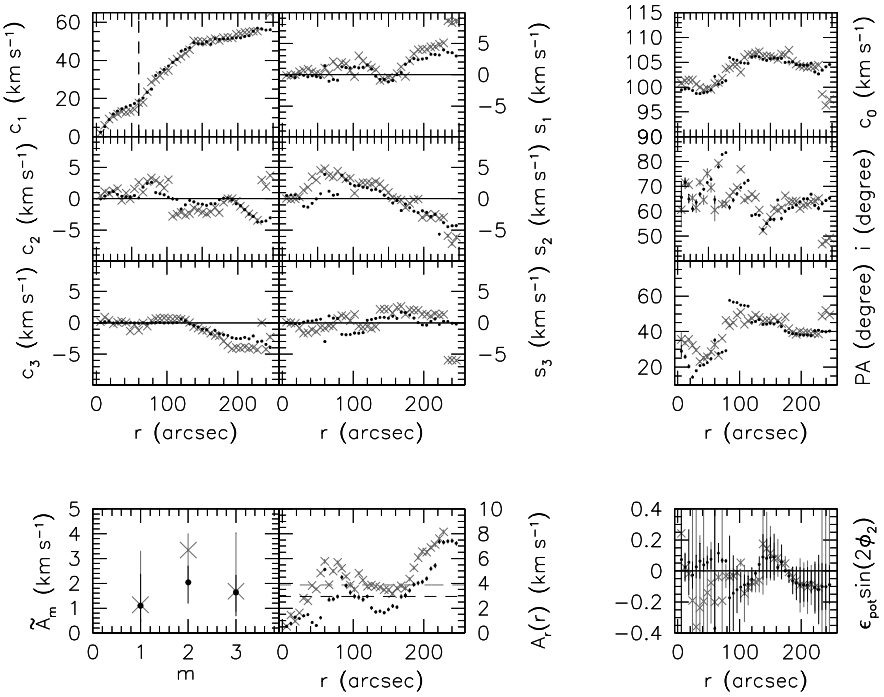

FIG. 22.— Like Fig. 21, but the harmonic analysis shown in gray is using a center position offset by 10″ along the minor axis. Although being larger than in the case of the offset along the major axis, the difference between the two decompositions is still small. The offset center causes the median amplitude of the non-circular motions (dashed line in the panel showing the distribution of $A_r(r)$) to increase from $\tilde{A}_r \sim 3\,\mathrm{km\,s^{-1}}$ to $\tilde{A}_r \sim 4\,\mathrm{km\,s^{-1}}$, showing that even a small offset along the minor axis does not influence the derived quantities in a significant way in the case of a dwarf galaxy like NGC 2366.

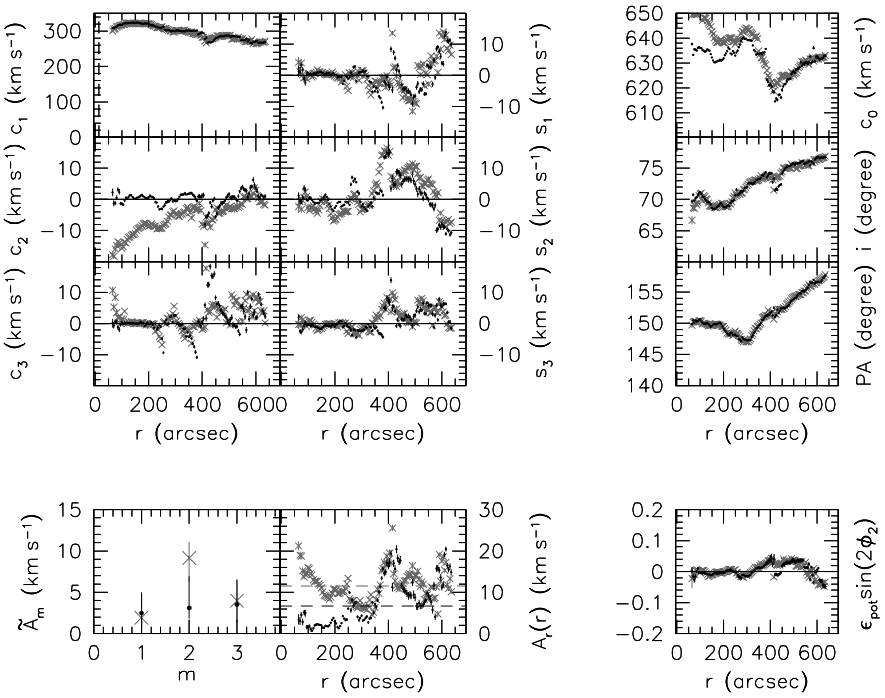

FIG. 23.— Harmonic analysis of NGC 2841 using our best center position (black) and a center position, offset by 10″ along the major axis (gray). The layout of the figure is identical to that of Figs. 3 and 4, except that we do not show any weighted means in the panels on the right-hand side. For NGC 2841, the amount of non-circular motions increases clearly when choosing an offset center. The largest differences are visible in the c_2 term. The median amplitude of the non-circular motions (dashed-line in the panel showing the distribution of $A_r(r)$) increases from $\tilde{A}_r \sim 7\,\mathrm{km\,s^{-1}}$ to $\tilde{A}_r \sim 12\,\mathrm{km\,s^{-1}}$, showing that in the case of NGC 2841, an offset along the major axis will clearly show itself as an increase in the amplitudes of the harmonic components.

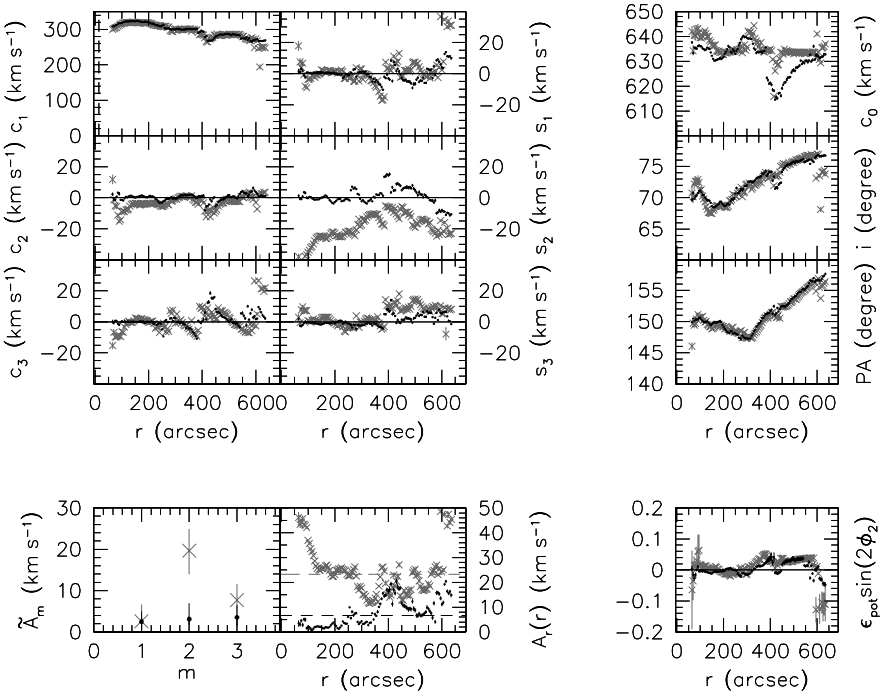

FIG. 24.— Like Fig. 23, but the harmonic analysis shown in gray is using a center position offset by 10″ along the minor axis. For NGC 2841, the amount of non-circular motions increases clearly when choosing an offset center. The largest differences are visible in the s_2 term. $\tilde{A}_r$ (dashed-line in the panel showing the distribution of $A_r(r)$) increases from $\tilde{A}_r \sim 7\,\mathrm{km\,s^{-1}}$ to $\tilde{A}_r \sim 25\,\mathrm{km\,s^{-1}}$, showing that in the case of NGC 2841, an offset along the minor axis will produce significantly different results than if the dynamical center position is chosen.

APPENDIX

A. DESCRIPTION OF INDIVIDUAL GALAXIES

In this section, we present for each galaxy in our sample a detailed description of *(a)* the derivation of the center position, and *(b)* the results of the harmonic decomposition. The galaxies are presented in order of increasing right ascension. The results are presented in graphical form in Figs. 25-42. Channel maps, optical images and moment maps for the galaxies in our sample are given in Walter et al. (2008). The different center estimates are summarized in Table 2, where our adopted best center positions are shown in bold face. The results from the harmonic decomposition are summarized in Table 3.

A.1. *NGC 925 (Fig. 25)*

a) Center estimates

NGC 925 is a barred late-type spiral galaxy whose H I disk looks rather clumpy. The 3.6 μm IRAC image shows a weak central bar and two spiral arms in the outer region. NGC 925 lacks a clear center in the IRAC image as well as in the radio continuum. We used ELLFIT at varying isophote levels to derive a central position from the IRAC image. This center is offset from the pointing center by $\delta X = -0\farcs8$ and $\delta Y = -2\farcs6$ (i.e., towards the south-east) and was used as an initial estimate for a ROTCUR run with all parameters left free. Averaging the values for δX, δY over the region not too heavily affected by spiral arms and asymmetries ($r \leq 121''$, see top row of Fig. 25) results in a center position offset from the pointing center by $\delta X = 4\farcs4 \pm 8\farcs3$ and $\delta Y = -1\farcs5 \pm 4\farcs2$. As this position is consistent with the center from the IRAC image (see row 2 of Fig. 25), we adopt the former one as our best center for NGC 925.

b) Harmonic expansion

The fitted values for the inclination show a lot of scatter in the inner 100″. This is partially caused by the near solid-body rotation in that region, which makes determining a kinematic inclination more difficult. Note that in the case of pure solid-body rotation, VROT and sin(i) are degenerate and cannot be fitted simultaneously. However, we seldom have to deal with *pure* solid-body rotation, but more usually with near solid-body rotation, which gives the algorithm some handle on the fitted values. Although the amplitudes of the individual components are not constant over the radial range, the median amplitudes of all harmonic orders are relatively small ($\tilde{A}_m \leq 5$ km s^{-1} when averaged over the entire galaxy). The median amplitudes are slightly higher if one averages over the inner 1 kpc only, which might be due to the stellar bar. $\tilde{A}_r$ is ~ 6.3 km s^{-1} if averaged over the entire range and ~ 9.5 km s^{-1} if averaged over the inner 1 kpc only (see also Table 3). The elongation of the potential is unconstrained inwards of $r \approx 100''$, mainly because of the large uncertainties for the derived inclination (which enters into the uncertainty in $\epsilon_{\rm pot}$ as a fourth power). Its weighted mean is consistent with a round potential ($\langle \epsilon_{\rm pot} \sin(2\varphi_2) \rangle = 0.000 \pm 0.046$, see again Table 3). The median of the absolute residual velocity field is 3.0 km s^{-1}, showing that a harmonic decomposition up to third order was able to capture most non-circular motions present in NGC 925.

A.2. *NGC 2366 (Fig. 26)*

a) Center estimates

NGC 2366 is classified as a dwarf irregular and belongs, like NGC 2403, to the M81 group. As for all the other dwarf galaxies in the sample presented here, the 3.6 μm IRAC image and the radio continuum map do not show a nuclear source. We derived the center of the emission in the IRAC image by using ELLFIT at varying isophote levels. The IRAC center is offset from the pointing center by $\delta X = 7\farcs8 \pm 0\farcs6$ and $\delta Y = -18\farcs0 \pm 1\farcs8$. This center estimate was used for a ROTCUR run with all parameters left free. We averaged the derived values for δX, δY for $r \leq 200''$ (see row 1 in Fig. 26), but excluded the discrepant data points between $70'' \leq r \leq 100''$. The resulting dynamical center is offset from the pointing center by $\delta X = 5\farcs2 \pm 3\farcs5$ and $\delta Y = -19\farcs2 \pm 7\farcs7$, and within the uncertainties consistent with the center position derived from the IRAC image (see row 2 of Fig. 26). Deriving a kinematic center by averaging over all data points out to $r = 200''$ gives a consistent center estimate, though with a larger scatter ($\delta X = 2\farcs9 \pm 6\farcs5$, $\delta Y = -18\farcs5 \pm 7\farcs9$). Therefore, we adopt the former kinematic estimate as our final center position.

b) Harmonic expansion

NGC 2366 shows no clear signs of spiral structure. Its rotation curve is clearly dominated by near solid-body rotation, making it difficult to determine the rotation velocity and i simultaneously. At $r \sim 100''$, the systemic velocity c_0 rises from ~ 100 km s^{-1} to ~ 105 km s^{-1}. At the same radius, the amplitude of s_2 "jumps" from ~ 0 km s^{-1} to ~ 4 km s^{-1} and decreases then to -4 km s^{-1} in the outskirts of NGC 2366. The distribution of $A_r(r)$ shows that the largest amount of non-circular motions is to be found in the outer parts of NGC 2366, and that the inner 1 kpc exhibit only minor non-circular motions. The weighted mean elongation is $\langle \epsilon_{\rm pot} \sin(2\varphi_2) \rangle = 0.003 \pm 0.067$ and the median of the absolute residual velocity field is 2.4 km s^{-1}, once again showing that the galaxy has a round potential and that there are no large non-circular motions present in the $m > 3$ terms.

A.3. *NGC 2403 (Fig. 27)*

a) Center estimates

NGC 2403 belongs to the M81 group, and is a late-type Sc spiral. Its 3.6 μm IRAC image shows multiple spiral arms and a bright central component. However, neither the IRAC image, nor the radio continuum map show a nuclear source. Therefore, we used 3.6 μm isophote fits to determine center coordinates and used the resulting center position (δX=–4.″7, δY=–13.″6) as an initial estimate for an unconstrained ROTCUR run. As can be seen in the first row of Fig. 27, δX and δY stay fairly constant

over a large part of the galaxy. We determine the dynamical center by averaging the values for $r \leq 220''$, thus excluding the radii where δX changes considerably, probably due to the spiral arm located at that radius. The offset from the pointing center is $\delta X = -5\farcs2 \pm 5\farcs2$ to the east and $\delta Y = -12\farcs8 \pm 4\farcs1$ to the south. Averaging δX and δY over a larger part of the galaxy gives comparable results but with a larger scatter. Given the agreement between the dynamical center estimate and the center as derived using the IRAC image, we adopt the $r \leq 220''$ kinematic center estimate as our best center position.

b) Harmonic expansion

The radial variation of the inclination is only $\sim 5°$, except at a few inner radii. The PA shows a steep inner rise, a flat outer part and a dip at $r \approx 200''$, which coincides with a high amplitude in the c_2 and s_2 components. Inspection of the integrated H I map shows a spiral arm crossing at this radius. The s_1 and s_3 components also show the characteristic wiggles caused by spiral arms. Additionally, s_3 has a small offset from zero, which through Eq. 3 can indicate a slightly elongated potential. The average elongation of NGC 2403, however, is $\langle \epsilon_{\rm pot} \sin(2\varphi_2) \rangle = -0.022 \pm 0.025$, and therefore consistent with a round potential. The distribution of $\tilde{A}_m$ shows that the individual harmonic orders contribute only ~ 2 percent to $V_{\rm tot}$, indicating that non-circular motions play a minor role in NGC 2403. The latter can also be seen in the distribution of $A_r(r)$.

A.4. *NGC 2841 (Fig. 28)*

a) Center estimates

NGC 2841 is an early-type spiral galaxy. Its H I distribution has a central hole and the IRAC 3.6 μm image shows a distinctive bulge and a flocculent spiral structure. The radio continuum map of NGC 2841 shows a strong nuclear source coinciding within $0\farcs2$ with the position of the central source in the 3.6 μm IRAC image. We used the position of the radio continuum source (δX=–$6\farcs3$, δY=$0\farcs5$) as input for ROTCUR and made a fit with all parameters left free. We averaged the values for δX and δY between $75'' < r < 220''$ (see first row in Fig. 28). The lower limit excludes the two innermost rings, as these are sparsely filled. The upper limit restricts our averaging to a region which is unaffected by spiral arms or by the warp. The dynamical center derived in such a way ($\delta X = -6\farcs5 \pm 0\farcs6$, $\delta Y = 0\farcs4 \pm 0\farcs9$) deviates by less than $0\farcs2$ from the other center estimates. Therefore, we choose the radio continuum center as the best center position.

b) Harmonic expansion

The inner 200″-250″ of NGC 2841 are in unperturbed circular rotation and show only small harmonic terms. For the inner 1 kpc, we have no data as the H I surface density in this region falls below the 3σ detection limit imposed on the velocity fields. Most of the parameters show a large change at $r \approx 350'' - 400''$: the systemic velocity drops by about 20 km s^{-1}, and most of the harmonic components show their highest amplitude at these radii. Looking at the total H I intensity map, one can see that this radius coincides with the location of a strong spiral arm. The dip in the fitted inclination at those radii causes a non-zero c_3 term, induced by the spiral arm. The radial variation of the PA and inclination indicates that the outer disk of NGC 2841 is warped. All harmonic components are similar in amplitude, having median amplitudes of $3 \leq \tilde{A}_m \leq 4$ km s^{-1}, or ≤ 2 percent of $V_{\rm tot}$. $A_r(r)$ is small in the inner parts, but > 10 km s^{-1} in the outer parts of NGC 2841. Its median value is $\tilde{A}_r \sim 7$ km s^{-1}. The elongation of the potential is fairly constant over the radius and its weighted average is consistent with a round potential (see Table 3).

A.5. *NGC 2903 (Fig. 29)*

a) Center estimates

NGC 2903 is a barred galaxy with tightly wound spiral arms. Its dominant bar can be seen both in the IRAC image and in the radio continuum map. The radio continuum additionally shows a strong nuclear source, coinciding within $1''$ with the center of the bulge in the 3.6 μm image. The central position as given by the radio continuum (δX=–$1\farcs2$, δY=$2\farcs4$) was used to make a ROTCUR run with all parameters left free. To derive the kinematic center, we averaged the δX and δY values over the stable parts of the fit, i.e., for $100'' \leq r \leq 300''$ (see top row in Fig. 29). The resulting kinematic center ($\delta X = 0\farcs4 \pm 2\farcs4$, $\delta Y = 0\farcs6 \pm 2\farcs2$) agrees within the uncertainties and within one beam with both the IRAC and the radio continuum center (cf. second row in Fig. 29). We therefore adopt the center position as derived from the radio continuum as our final central position.

b) Harmonic expansion

NGC 2903 shows high amplitudes in all harmonic components in the inner $125''$. These non-circular motions are presumably caused by the bar in NGC 2903. The innermost 4-5 data points show the largest deviations from the general trends, most clearly visible in the distributions of the PA, inclination and c_0.

The pronounced shape in the distribution of s_2 could be caused by an $m = 1$ or $m = 3$ term in the gravitational potential. Given that NGC 2903 is not kinematically lopsided (there is, e.g., no significant difference in the rotation curves of the approaching and receding sides), the contribution from an $m = 1$ term is likely to be small. Inspection of the total H I maps presented in Walter et al. (2008) shows that a spiral arm is located at the same radii as the pronounced variation in s_2. The wiggles in the radial distributions of s_1 and s_3 at $r \sim 100''$ and $r \sim 350''$ also coincide with the locations of spiral arms. The median amplitudes of the individual harmonic components are small when averaged over the entire galaxy ($\tilde{A}_m \leq 4$ km s^{-1}, or 2-3 percent of $V_{\rm tot}$), but increase towards the center of the galaxy. Within the inner kpc, the $m = 2$ component of $\tilde{A}_m$ has a median value of about 14 km s^{-1}. These high non-circular motions, which can also be seen in the distribution of $A_r(r)$, are likely to be caused by the strong bar, and the associated streaming motions. Like some of the c_i, s_i, and thus also $A_r(r)$, the elongation of the potential shows some variations with radius. Its mean value is nevertheless consistent with a round potential (see Table 3).

A.6. *NGC 2976 (Fig. 30)*

a) Center estimates

The 3.6 μm image of NGC 2976 shows no sign of a bar or spiral arms. Nevertheless, the image shows two enhanced star forming regions at either end of the disk which coincide with density enhancements in the total H I map. Additionally, the IRAC image contains a nuclear source in the central parts of the galaxy, presumably a nuclear star cluster, which has, however, no counterpart in the radio continuum. To test whether the position of this central source agrees with the dynamical center, we perform an unconstrained ROTCUR run and use the position of the nuclear star cluster (δX= 0.″2, δY= 0.″1) as an initial center estimate. By averaging δX, δY over $r < 50''$ (see Fig. 30, top row), we derive a dynamical center which is offset from the pointing center by $\delta X = 2.''2 \pm 3.''0$ and $\delta Y = 0.''8 \pm 1.''4$ towards the north-west. Averaging over the entire galaxy gives consistent results ($\delta X = 2.''5 \pm 3.''0$, $\delta Y = 1.''6 \pm 3.''9$). As the dynamical center and the position of the nuclear star cluster agree within the uncertainties and to within one beam (cf. second row in Fig. 30), we adopt the position of the nuclear star cluster as the best center position of NGC 2976.

b) Harmonic expansion

The harmonic components of the velocity field of NGC 2976 show a regular behavior. Both s_1 and s_3 scatter within ~ 1 km s^{-1} around zero, indicating that the elongation of the gravitational potential is very small. Its weighted mean is consistent with zero ($\langle \epsilon_{\rm pot} \sin(2\varphi_2) \rangle = -0.010 \pm 0.018$).

The c_2 component is slightly offset from zero and shows sine-like variations with radius, especially for $r > 80''$, where the two H I density enhancements are located. According to Schoenmakers (1999), a non-zero $m = 2$ harmonic component in the velocity field can be caused by an $m = 1$ or $m = 3$ term in the potential. NGC 2976 does not seem to be kinematically lopsided (cf. the negligible differences in the rotation curves of the approaching and receding sides in de Blok et al. 2008). Therefore, there is most likely only a small contribution of an $m = 1$ term in the potential to the $m = 2$ harmonic term in the velocity field, and the significant contribution should come from an $m = 3$ term in the potential.

Beyond $r \approx 80''$, the PA stays constant. The median amplitudes of all harmonic component are small ($\tilde{A}_m \leq 3$ percent $V_{\rm tot}$), irrespective of whether one averages over the entire galaxy or only over the inner 1 kpc. The distribution of $A_r(r)$ is also small for most radii. Only a few data points at extreme radii show large amplitudes, but these are associated with large uncertainties. The mean elongation of the potential is, despite being unconstrained in the inner $30''$, again consistent with a round potential (see Table 3).

A.7. *NGC 3031 (Fig. 31)*

a) Center estimates

NGC 3031 (better known as M 81) is a grand design spiral. Its two well-defined spiral arms are easily visible in the IRAC 3.6 μm image as well as in the H I intensity map. NGC 3031 contains a strong central radio source. The 3.6 μm image also shows a well-defined central component with a central minimum which coincides with the position of the central radio-continuum source (δX= $-202.''7$, δY= $-371.''9$). We used the position of the radio continuum source as input for a ROTCUR run with all parameters left free. As can be seen in the top row of Fig. 31, δX and δY show a clear break at $r \sim 400''$, probably because of the prominent spiral arm which is located at approximately that radius. We therefore estimated the dynamical center by averaging δX and δY over $200'' \leq r \leq 385''$, thus omitting the innermost data points whose tilted-rings are only sparsely filled and have correspondingly large uncertainties. The resulting dynamical center ($\delta X = -205.''1 \pm 3.''1$, $\delta Y = -374.''6 \pm 3.''9$) coincides within the uncertainties and within less than one beam with the other center estimates (second row of Fig. 31) and we therefore adopt the position of the radio continuum source as the best center position of M 81.

b) Harmonic expansion

The PA, c_0, and the inclination of M 81 rise steadily beyond $r \approx 400''$, indicating that the outer disk is warped or disturbed, which is not unexpected given that M 81 interacts with M 82 and NGC 3077. The radii with the highest gradient in s_1 and s_3 ($r \approx 350'' - 400''$) correspond with the location of a prominent spiral arm. Between $400'' \leq r \leq 700''$, c_2 and s_2 change from values around +5 km s^{-1} to < -10 km s^{-1}. Note that if we were to perform a harmonic decomposition with an unconstrained center position, the center would vary at those radii in order to minimize the c_2 and s_2 term, thus underestimating the amount of non-circular motions present in M 81. However, as we keep the center position fixed, we are able to quantify and detect these non-circular motions. The median amplitudes $\tilde{A}_m$ of the $m = 2$ and $m = 3$ component are roughly equally high (~ 5 km s^{-1}), whereas that of the $m = 1$ component is slightly smaller (~ 2 km s^{-1}). As M81 has a central H I minimum, we have no data for the inner 1 kpc. The radial distribution of the non-circular motions varies between $3 \leq A_r(r) \leq 15$ km s^{-1} and has a median of $\tilde{A}_r \sim 9$ km s^{-1} (<5 percent of $V_{\rm tot}$), making the amount of non-circular motions quite small, despite the prominent spiral arms. The elongation of the potential shows distinct radial variation which is due to the spiral arms. Its weighted average is again consistent with zero (see Table 3).

A.8. *NGC 3198 (Figs. 1-4)*

a) Center estimates

NGC 3198 is classified as a SBc spiral. Its 3.6 μm IRAC image shows two well-defined spiral arms, emanating from a prominent bulge. The central component has a nuclear point source embedded, which has a counterpart in the radio continuum. The center estimates from the IRAC image and the continuum map agree to within $1''$. We make a ROTCUR run with the position of the radio

continuum center (δX= –1.″4, δY= –0.″1) as an initial estimate. Fig. 1 shows that the outer parts ($r \geq 150''$) of NGC 3198 are strongly affected by the spiral arms. For the derivation of the dynamical center, we therefore restrict the averaging of δX and δY to radii with $r \leq 100''$. The derived dynamical center ($\delta X = -1.''4 \pm 1.''7$, $\delta Y = -0.''2 \pm 2.''1$) agrees well with the other estimates (see Fig. 2). We therefore adopt the position of the continuum source as the best center position for NGC 3198.

b) Harmonic expansion

The PA of NGC 3198 shows a steep increase within the inner 200″, and then declines slowly. The inclination varies in the inner parts in a range of about five degrees, but shows a steady increase beyond $r \sim 450''$, indicating that the outer disk is warped. The c_3 term is small, meaning that the fitted inclination is close to the intrinsic inclination of the disk. Although there is no global offset from zero for c_2 and s_2, they show small deviations from zero for some radii which are coinciding with the locations of spiral arms in the 3.6 μm image or the total H I map presented in Walter et al. (2008). The distributions of s_1 and s_3 are best described as wiggles caused by spiral arms on top of a small offset. The global elongation of the potential is with $\langle \epsilon_{\rm pot} \sin(2\varphi_2) \rangle = 0.017 \pm 0.020$ consistent with zero.

The median amplitudes of the individual harmonic components are similar in amplitude, and of order $\tilde{A}_m \sim 2-3$ km s^{-1}, or $\leq$ 2 percent of $V_{\rm tot}$. The distribution of $A_r(r)$ shows that the amplitude of the non-circular motions is ≤ 8 km s^{-1} for most radii. Its median is $\tilde{A}_r \sim 4.5$ km s^{-1} when averaged over the entire radial range, and $\tilde{A}_r \sim 1.5$ km s^{-1} for the inner 1 kpc. The median value of the absolute residual velocity field is ~ 2.6 km s^{-1}, showing that a harmonic decomposition up to third order was capable of capturing most non-circular motions.

A.9. *IC 2574 (Fig. 32)*

a) Center estimates

IC 2574 has neither a central radio continuum source, nor a clear nuclear source in the 3.6 μm IRAC image. The dynamics of this galaxy show clear evidence of random non-circular motions, showing themselves as kinks in the iso-velocity contours. For the center determination, we make use of a velocity field where most non-circular features were removed (as presented in Oh et al. 2008). We make a ROTCUR run with all parameters free, using the center position derived by Oh et al. (2008) as an initial center estimate. The results of the ROTCUR fit are shown in row 1 of Fig. 32. It can be seen that the values for δX and δY do not change much over a large part of the galaxy. Averaging δX, δY over $r \leq 400''$ results in a dynamical center which is offset by $\delta X = 8.''7 \pm 14.''9$ and $\delta Y = 18.''6 \pm 10.''4$ towards the north-west of the pointing center. This corresponds to $\alpha_{2000} = 10^h28^m27.5^s$, $\delta_{2000} = +68°24'58.''7$ and is in excellent agreement with the estimate derived by Oh et al. (2008) ($\alpha_{2000} = 10^h28^m27.7^s$, $\delta_{2000} = +68°24'59.''4$).

b) Harmonic expansion

Although we made use of the bulk velocity field from Oh et al. (2008) for the center estimate, we use the hermite velocity field for the harmonic decomposition, as we aim to quantify non-circular motions. The results of the harmonic decomposition of the hermite velocity field of IC 2574 are shown in the third row of Fig. 32.

At a radius of $r \sim 250''$, the PA and inclination drop significantly, and the harmonic components jump to more extreme values. The distribution of $A_r(r)$ has its maximum at this radius, and c_1 also shows a clear break. The feature which is most likely responsible for the major non-circular motions is the supergiant shell in the north-east of IC 2574 (see Walter et al. 1998). Looking only at the inner 1 kpc, the amplitudes of the individual harmonic components are all ≤ 1 km s^{-1}. If one measures the amplitudes over the entire radial range of the galaxy, the $m = 2$ component is the dominant one, mainly because of the large amplitudes in c_2 and s_2 at $r \sim 250''$.

The median amplitude of the quadratically added non-circular motions is $\tilde{A}_r \sim 3.8$ km s^{-1} when averaged over the entire radial range, and $\tilde{A}_r \sim 1.4$ km s^{-1} for the inner 1 kpc. This shows that although IC 2574 contain a significant amount of *chaotic* non-circular motions (see Oh et al. 2008), the effect of *systematic* (potential induced) non-circular motions is small. For some parts of the galaxy, the elongation of the potential is unconstrained. Its weighted mean is consistent with a round potential, although it has a large uncertainty associated ($\langle \epsilon_{\rm pot} \sin(2\varphi_2) \rangle = 0.015 \pm 0.045$).

A.10. *NGC 3521 (Fig. 33)*

a) Center estimates

NGC 3521 appears in the 3.6 μm IRAC image as well as in the H I map as a multi-armed, flocculent spiral galaxy. The IRAC image shows an inner disk, in which a strong nuclear point source (without a counterpart in the radio continuum) is embedded. We use the position of the nuclear point source (δX= –8.″8, δY= 5.″7) as input for a ROTCUR fit with all parameters left free. The top row of Fig. 33 shows that the values of δX and δY stay constant for radii smaller than 220″. Beyond that radius, the rotation curves for the approaching and receding sides start to differ (see de Blok et al. 2008) and this most likely also affects the derived central positions. In order to derive a dynamical center, we average δX and δY for $r \leq 220''$. The resulting center ($\delta X = -8.''9 \pm 0.''8$, $\delta Y = 6.''6 \pm 1.''4$) agrees with the central position found in the IRAC image (see second row of Fig. 33) and we adopt the IRAC position as the best center estimate.

b) Harmonic expansion

As can be seen, e.g., in the radial distribution of PA, i, and $A_r(r)$, the inner few data points clearly deviate from the rest. Note that the c_3 component is higher for these points, meaning that their inclination could not be fitted correctly in an unconstrained fit. Some of these inner data points show large non-circular motions, while others (e.g., the inner two points) do not. This becomes

even clearer if one looks at the distribution of $\tilde{A}_m$. Although the median of the $m = 3$ component in the inner 1 kpc is small, its upper quartile is rather large, as the inner 1 kpc contain only three data points, one of which has a large amplitude. The s_1 and s_3 components are both slightly offset from zero and superimposed on a wiggle at $r \approx 200''$. The wiggle coincides with a density enhancement in the total H I intensity map (in this case a spiral arm). However, as s_1 is offset to negative values, and s_3 to positive ones, their offsets almost cancel out for the derivation of the elongation of the potential (cf. Eq. 3), whose weighted mean is within the uncertainties consistent with zero ($\langle \epsilon_{\rm pot} \sin(2\varphi_2) \rangle = 0.017 \pm 0.019$).

The effect of the spiral arms is clearly visible in the c_2 and s_2 components. NGC 3521 has the highest median value in the absolute residual velocity field of our sample (4.5 km s^{-1}).

A.11. *NGC 3621 (Fig. 34)*

a) Center estimates

The 3.6 μm IRAC image of NGC 3621 is dominated by a flocculent spiral structure, which contains a central point source. The prominent star forming region in the south-west is connected to the center of the galaxy by a spiral arm which is clearly visible in the total H I map and the IRAC image. While this star forming region has a counterpart in the radio continuum, the IRAC nuclear point source has not. We use the coordinates of the nuclear point source in the IRAC image (δX= $-4\farcs2$, δY= $-1\farcs1$) as an initial estimate for a ROTCUR fit with all parameters left free. The results (top row of Fig. 34) show that the derived central positions are fairly constant for radii smaller than $450''$ and we therefore derive the dynamical center by averaging over all points with $r < 450''$, with the additional exclusion of the innermost data point. The resulting dynamical center ($\delta X = -6\farcs0 \pm 2\farcs0$, $\delta Y = 1\farcs4 \pm 6\farcs5$) coincides with the coordinates of the point source both within the uncertainties and the size of the beam (Fig. 34, second row). Therefore, we adopt the position of the central point source as our best center estimate for NGC 3621.

b) Harmonic expansion

The data points beyond $r = 600''$ are not used for our analysis due to their sparsely filled tilted-rings. The PA of NGC 3621 is, except for the innermost two data points, constant to within a few degrees. Apart from a few data points at extreme radii, the amplitude of s_1 is almost negligible. c_3 is close to zero, except for $r \approx 300''$. This position also coincides with the radius of the highest amplitude in c_2, and s_2. Inspection of the total H I intensity map shows that there is a ring-like H I density enhancement at which a spiral arm emerges in the south-east. The s_3 component shows clear wiggles, indicating spiral arms, and a steep rise beyond $r \approx 500''$, where the tilted-rings are less filled. The elongation of the potential again shows the kinematic signature of the spiral arms. Its weighted average is consistent with zero (see Table 3). The median amplitudes for each individual harmonic component are fairly small ($\tilde{A}_m < 3$ km s^{-1}, or ≤ 2 percent of $V_{\rm tot}$). The distribution of $A_r(r)$ is ≤ 5 km s^{-1} for the majority of radii and has a median value of $\tilde{A}_r \sim 3.4$ km s^{-1}.

A.12. *NGC 3627 (Fig. 35)*

a) Center estimates

The 3.6 μm IRAC image shows that NGC 3627 is a barred galaxy with two asymmetric spiral arms, which are also clearly visible in the total H I map. The central parts of NGC 3627 contain a nuclear point source which is visible in the IRAC image as well as in the radio continuum. Using the position of the point source ($\delta X = 0\farcs1$, $\delta Y = 0\farcs1$) as input for an unconstrained ROTCUR fit results in a slightly different center estimate (see row 1 and 2 of Fig. 35). We exclude some data points at extreme radii because of their large uncertainties, and average δX, δY for $45'' \leq r \leq 160''$, resulting in a dynamical center which is offset from the pointing center by $\delta X = -4\farcs5 \pm 3\farcs1$ and $\delta Y = -6\farcs8 \pm 4\farcs8$. These values deviate from the radio continuum source by approximately 1.5σ. Given the asymmetric appearance of NGC 3627, it is to be expected that the results from ROTCUR are somehow affected by it. However, the difference between the kinematic center and the center from the radio continuum is only one beam. We therefore use the coordinates of the central radio continuum source as the best center position for NGC 3627.

b) Harmonic expansion

NGC 3627 has a central hole in the H I distribution. Therefore, we see only the flat part of the rotation curve and have no data within the inner kpc. The systemic velocity changes from $\sim$730 km s^{-1} at $r \leq 60''$ to $\sim$705 km s^{-1} for $r \geq 90''$. All harmonic components (c_2, c_3, s_1, s_2, s_3) show high amplitudes. The galaxy is kinematically and morphologically lopsided (cf., de Blok et al. 2008), which is also indicated by the non-zero values for c_2 and s_2. Both the s_1 and the s_3 component show a "dip" at $r \approx 70''$, followed by a steep rise beyond that radius. In the case of s_3, the rise is followed by a second decline. The radius of that first "dip" coincides with the location of the large arm which extends to the south of NGC 3627. The median amplitudes of the individual harmonic components are the highest in our sample, reaching from $\tilde{A}_m \sim 10$ km s^{-1} for $m = 3$ to $\tilde{A}_m \sim 17$ km s^{-1} for $m = 2$. The distribution of $A_r(r)$ shows that the amplitude of non-circular motions is large at all radii. The median amplitude is $\tilde{A}_r \sim 28.5$ km s^{-1}, or up to 14.7 percent of $V_{\rm tot}$. Given the morphology of NGC 3627, this is not unexpected. Despite the high non-circular motions present here, the weighted mean elongation of the potential is still small, and within its uncertainty consistent with a round potential (cf. Table 3), although there are large errors associated with the data points in the outer parts and in the region at $r \approx 70''$.

A.13. *NGC 4736 (Fig. 36)*

a) Center estimates

The 3.6 μm IRAC image of NGC 4736 is dominated by a ring of star formation which is also prominently visible in the radio

continuum and the total H I map. The center is well-defined both in the 3.6 μm image and in the radio continuum. The former shows a small central *minimum* in the flux which coincides within 1.″3 with the central radio-continuum *maximum*. We use the position of the radio continuum source ($\delta X = 0.''2$, $\delta Y = -0.''4$) for a ROTCUR run with all parameters left free. The fitted center positions are stable within the inner 100″, but have an increasingly large scatter towards the outer parts, most likely due to the marginally filled tilted-rings beyond $r \sim 100''$, and also because of the low inclination of NGC 4736. We therefore average the estimates for δX and δY over the inner 100″, resulting in a dynamical center ($\delta X = 0.''5 \pm 1.''8$, $\delta Y = 0.''6 \pm 2.''0$) whose deviation from the other center estimates slightly exceeds the uncertainties (1.2σ deviation for δY). Though, to put things into perspective, this is far smaller than one beam (see second row of Fig. 36). Thus, we will use the position of the radio continuum source as the best center estimate for NGC 4736.

b) Harmonic expansion

The star forming ring at $r \sim 80''$ causes a lot of confusion in the inner parts of NGC 4736. Here the unconstrained fit by RESWRI produces an apparent rotation velocity which rises to twice the value in the outer parts. The other harmonic components also show high amplitudes. The median amplitudes of each harmonic component (averaged over the inner 1 kpc) are negligible for the $m = 1$ and $m = 3$ component ($\tilde{A}_m \sim 1$ km s^{-1}), but much higher for the $m = 2$ component ($\tilde{A}_m \sim 7$ km s^{-1}). The amplitude of the quadratically added non-circular motions, $A_r(r)$, is ~ 10 km s^{-1} for most radii.

NGC 4736 is both kinematically and morphologically lopsided, which can be seen not only in the differences between the rotation curves of the approaching and receding sides (see de Blok et al. 2008), but also in the high amplitudes in the c_2 and s_2 terms of our harmonic expansion. The highest amplitudes in the harmonic terms are found for radii between $r \approx 200''$ and $r \approx 300''$, i.e., those radii where the large northern spiral arm is located. The weighted average of the elongation of the potential is $\langle \epsilon_{\rm pot} \sin(2\varphi_2) \rangle = -0.055 \pm 0.149$.

A.14. *DDO 154 (Fig. 37)*

a) Center estimates

DDO 154 is a quiescent, gas-rich dwarf galaxy with a warp in the outer parts. It does not have a compact, well-defined center in the 3.6 μm IRAC image, or in the radio continuum. We attempted to derive a center position by fitting ellipses at a few representative intensity levels to the IRAC image, and the total H I map. The resulting central positions showed a variation of up to 15″, demonstrating that deriving an unambiguous *photometric* center for DDO 154 is not straightforward. We used the center which was derived using the total H I map as a initial estimate for a ROTCUR fit with all parameters left free. The central positions as derived by ROTCUR are fairly stable over the radial range of the galaxy and the kinematic center was derived by averaging the δX, δY values over $100'' \leq r \leq 260''$, thus omitting the slightly more unstable inner and outer regions. The resulting center position is given in Table 2. Including the inner data points gives a similar center position, but with two times larger scatter. We therefore adopt the dynamical center as averaged over $100'' \leq r \leq 260''$ as the best center position of DDO 154.

b) Harmonic expansion

The c_3 term is close to zero for the entire radial range, normally indicating that the inclination could be well-determined. However, due to the nearly solid-body rotation in the innermost parts of DDO 154, the inclination is not very well-constrained in this region, as can be seen in the large scatter of the individual data points for $r \leq 70''$. This is studied in more detail in Section 6.4. The c_2 component shows a maximum at around $r \approx 80''$ which coincides with a minimum in the s_2 component and a change in the systemic velocity c_0, providing evidence for a small kinematic lopsidedness as supported by the variation of the center position at these radii and the differences between the approaching and receding sides of the rotation curve (see de Blok et al. 2008). However, the effects described above are small. Despite the small-scale structure present in the velocity field, the amplitudes of all harmonic components — both for the entire galaxy and for the innermost 1 kpc — are ≤ 1 km s^{-1}, or ~ 2 percent of $V_{\rm tot}$. The distribution of $A_r(r)$ shows that the amplitudes of non-circular motions in DDO 154 are small for all radii. The mean elongation of the potential is small, $\langle \epsilon_{\rm pot} \sin(2\varphi_2) \rangle = 0.024 \pm 0.033$, and consistent with zero. The median of the absolute residual velocity field is 1.2 km s^{-1} (the smallest in our sample).

A.15. *NGC 4826 (Fig. 38)*

a) Center estimates

NGC 4826 shows no sign of spiral structure in the 3.6 μm IRAC image, but has two counter-rotating gas disks (Braun et al. 1994). The center of NGC 4826 is well-defined by the central, compact source visible in the radio continuum, and the IRAC 3.6 μm image, whose coordinates agree to within 1″. We use the position of the radio continuum source ($\delta X = 2.''4$, $\delta Y = 8.''5$) as an initial estimate for an unconstrained ROTCUR fit. We derive the dynamical center by averaging the δX, δY values inwards of 60″, i.e., over the radial range of the inner disk. The kinematic center derived in such a way ($\delta X = 2.''2 \pm 1.''6$, $\delta Y = 7.''5 \pm 0.''8$) agrees well with the other center estimates and we therefore assume the position of the radio continuum source to be the best center for NGC 4826.

b) Harmonic expansion

Because of the sparsely filled tilted-rings, and the additional complication of the two counter-rotating disks, we have not attempted to derive a harmonic decomposition for this galaxy.

A.16. *NGC 5055 (Fig. 39)*

a) Center estimates

NGC 5055 is classified as an Sbc galaxy and has a flocculent structure in the 3.6 μm IRAC image. The IRAC image shows a compact nucleus with a well-defined center, whose position coincides to within 1″ with a faint central radio continuum source. We use the position of the latter ($\delta X = 8\farcs8$, $\delta Y = 0\farcs4$) as the input center for a ROTCUR run with all parameter left free.

We derive the dynamical center by averaging the δX, δY values for radii smaller than 450″ to exclude the parts with sparsely filled tilted-rings beyond $r \sim 450''$. This center ($\delta X = 8\farcs2 \pm 4\farcs8$, $\delta Y = 0\farcs4 \pm 2\farcs0$) coincides within the uncertainties and to within a beam size with the other center estimates. We therefore adopt the position of the radio continuum source as the best estimate for the central position of NGC 5055.

The H I distribution and kinematics of NGC 5055 were recently analyzed by Battaglia et al. (2006). They define a dynamical center coinciding with their optical center at $\alpha_{2000} = 13^h15^m49.25^s$, $\delta_{2000} = +42°01'49\farcs3$, which is 4″ to the north of our choice. As our choice was also guided by the position of the central source in the 3.6 μm image, this would imply that the respective photometric centers must be shifted by 4″ with respect to each other. The optical center position listed in Battaglia et al. (2006) is ultimately based on a listing in Maoz et al. (1996) of the position of the central UV source in NGC 5055 determined using an HST FOC image. On examination of the relevant image in the Hubble Space Telescope archive, we find the central source to be located at $\alpha_{2000} = 13^h15^m49.3^s$, $\delta_{2000} = +42°01'46\farcs2$, which is in much closer agreement (0.″8) with our position.

b) Harmonic expansion

For the harmonic analysis of NGC 5055, a distinction between the inner and the outer parts has to be made. NGC 5055 has a well-defined H I disk which extends to about 450″. Beyond that radius, the H I column density is lower and generally falls below the 3 σ column density limit which we imposed during the construction of the velocity fields (see de Blok et al. 2008). Therefore, the uncertainties increase rapidly and we considered only data points with radii $r < 450''$ for the radial averaging of the parameters. The median amplitudes of the individual harmonic components (averaged over $r < 450''$) are all fairly low ($\tilde{A}_m < 3$ km s^{-1} or ~ 2 percent of $V_{\rm tot}$). The median amplitudes averaged over the inner 1 kpc contain only three data points and are also low for the $m = 1$ and $m = 3$ components, but quite high (~ 8 km s^{-1}) for the $m = 2$ component. The latter has a large scatter associated with it, mainly because of the innermost data point which shows high non-circular motions, but is derived from an only partially filled tilted-ring. The global elongation of the potential is well-constrained in the inner part of NGC 5055. The weighted mean elongation within 450″ is again consistent with a round potential (see Table 3).

A.17. *NGC 6946 (Fig. 40)*

a) Center estimates

NGC 6946 is a late-type spiral galaxy with well-defined multiple spiral arms. The IRAC 3.6 μm image shows a point source in the center of the galaxy which coincides to better than 1″ with the central radio continuum source. We use the position of the latter ($\delta X = -1\farcs8$, $\delta Y = 14\farcs5$) as input for a ROTCUR fit with all parameters left free and determine the dynamical center by averaging the δX, δY values for $22'' \leq r \leq 290''$, thus excluding the two innermost points which are affected by sparsely filled tilted-rings. The resulting dynamical center ($\delta X = -3\farcs3 \pm 4\farcs4$, $\delta Y = 11\farcs8 \pm 5\farcs8$) coincides within the uncertainties and to within one beam with the other center estimates (see Fig. 40, row 2). The large uncertainties in the kinematic estimate are caused by the relatively low inclination of NGC 6946, which makes an unconstrained tilted-ring fit of the velocity field more difficult. We adopt the position of the central radio continuum source as the best center for NGC 6946.

b) Harmonic expansion

NGC 6946 is the galaxy in our sample with the lowest inclination. This introduces larger uncertainties in the rotation curve and the harmonic decomposition. For our analysis of the median amplitudes, and for the derivation of the average elongation, we regard only the inner 420″, i.e., the region where the unconstrained apparent circular velocity c_1 does not rise to a value two times that in the flat part. This radius also coincides with the location from which, when moving outwards, the approaching and receding sides of the velocity field start to differ substantially (see de Blok et al. 2008). The median amplitudes averaged over $r < 420''$ are small for each harmonic component ($\tilde{A}_m \leq 5$ km s^{-1}). Due to the deficiency of H I in the center of NGC 6946, we can not study the kinematics within the inner 1 kpc. Again averaging only over $r < 420''$, the median of the quadratically added amplitudes of all non-circular components is $\tilde{A}_r \approx 7$ km s^{-1}. The steep rise in s_2 and s_3 at $r \approx 120''$ is probably caused by the spiral arm which crosses at that radius. Due to the low inclination of NGC 6946, and the associated large error in the derivation of the fitted parameters, the elongation of the potential is not well-constrained for $r \leq 150''$ and $r \geq 420''$. Its weighted mean (again averaged over $r \leq 420''$), however, is consistent with a round potential.

A.18. *NGC 7331 (Fig. 41)*

a) Center estimates

The 3.6 μm IRAC image of NGC 7331 shows prominent spiral arms, and a well-defined nucleus which has no counterpart in the radio continuum. We use the center from the 3.6 μm image ($\delta X = 0\farcs1$, $\delta Y = 0\farcs3$) as input for an unconstrained fit with ROTCUR. Ignoring the two innermost points as their tilted-rings are only sparsely filled, we average the values for δX and δY over the stable region with $r \leq 185''$. This results in a dynamical center of $\delta X = 0\farcs0 \pm 0\farcs6$, $\delta Y = -1\farcs8 \pm 2\farcs2$, which agrees within the uncertainties and to within one beam with the IRAC center. Therefore, we adopt the IRAC center as our best center position for NGC 7331.

b) Harmonic expansion

Although PA and inclination do not change much over the radial range (∼4-6 degrees), they both increase outwards, indicating a warping of the disk. The small c_3 values denote that the inclination could be well-determined for most radii. The s_1 and s_3 values both show a wiggle at $r \approx 150''$, coinciding with the location of a spiral arm visible in the total intensity H I map and in the IRAC 3.6 μm image. The variation of c_0, c_2, and s_2 shows that NGC 7331 is kinematically lopsided, as shown by the differences in the rotation curves of the receding and approaching sides of the velocity field (cf., de Blok et al. 2008). The median amplitudes of the individual harmonic components are all small ($\tilde{A}_m < 5$ km s^{-1}). Because of the central H I deficiency of NGC 7331, there is no kinematic data for the inner 1 kpc. The distribution of $A_r(r)$ varies between $A_r(r) \sim 2$ km s^{-1} and $A_r(r) \sim 10$ km s^{-1} and has a median of $\tilde{A}_r \sim 6$ km s^{-1}. The elongation of the potential is well-determined and close to zero for most radii. The wiggle at $r \approx 150''$ is again an indication of the aforementioned spiral arm. The weighted mean elongation is $\langle \epsilon_{\rm pot} \sin(2\varphi_2) \rangle = -0.003 \pm 0.017$, and therefore consistent with a round potential.

A.19. *NGC 7793 (Fig. 42)*

a) Center estimates

NGC 7793 is a flocculent spiral whose 3.6 μm IRAC image shows a well-defined central source without a counterpart in the radio continuum. We adopt the position of this source ($\delta X = -9\farcs1$, $\delta Y = -0\farcs9$) as the initial estimate for an unconstrained ROTCUR fit, and average the δX, δY values over the stable part of the galaxy ($r \leq 180''$). The resulting kinematic center ($\delta X = -9\farcs9 \pm 2\farcs6$, $\delta Y = 1\farcs8 \pm 2\farcs1$) agrees reasonably well with the IRAC center (1.5σ deviation). However, the deviation between these two center estimates is ∼ 6 times smaller than the size of one beam and we therefore use the IRAC center as our best center position.

b) Harmonic expansion

The PA and the inclination vary continuously with radius, indicating that the disk of NGC 7793 might be warped. The systemic velocity, c_0, stays fairly constant over radius. The offset from zero in the s_2 component might indicate a slight kinematic lopsidedness, which is also visible in the difference between the receding and approaching sides of the rotation curve in de Blok et al. (2008). The s_3 term is significantly larger than the s_1 term, which is typical for galaxies with low inclination (Schoenmakers 1999). In fact, the s_3 component seems to be offset from zero, indicating through Eq. 3 an elongation of the potential. The weighted mean elongation is $\langle \epsilon_{\rm pot} \sin(2\varphi_2) \rangle = -0.067 \pm 0.085$, which is the largest elongation we have measured in our sample. It is due to its large uncertainty consistent with both the CDM predictions by Hayashi et al. (2007) and with a round potential. The large uncertainty for the elongation arises from the relatively large error bars of the inclination values, which enter into the uncertainty in $\epsilon_{\rm pot}$ as a fourth power (cf. Eq. 3). The median amplitude of each harmonic component is fairly low ($\tilde{A}_m < 4$ km s^{-1}), both for the entire galaxy and for the inner 1 kpc. The distribution of $A_r(r)$ shows that the amplitude of non-circular motions is small, especially in the inner parts of NGC 7793. Its median value (averaged over the entire galaxy) is $\tilde{A}_r \sim 5$ km s^{-1}. The median of the absolute residual velocity field is 2.2 km s^{-1}, again showing that a harmonic expansion up to third order did cover most of the non-circular motions.

B. THE ATLAS

The center estimates and the harmonic decompositions are shown in Figs. 25-42. Following is a description of the content and layout of the figures: Each figure consists of four rows. From top to bottom, they contain:

Row 1: The radial variation of the center position. Shown is the offset from the pointing center in arcsecond. The top panel shows the offsets in the X (or right ascension) direction, with positive δX to the west; the bottom panel those in the Y (declination) direction, with positive δY to the north. The filled circles represent the individual center positions derived using ROTCUR, and the error bars indicate the formal uncertainties derived by ROTCUR. The two dotted, vertical lines indicate the radial range over which the positions were averaged in order to derive a kinematic center. The kinematic center is indicated by the solid horizontal line, and the 1σ standard deviation by the dotted, horizontal lines. For those cases where the kinematic center was not used as our best center position, we additionally show the best estimate with a dashed, horizontal line.

Row 2: The inner $150'' \times 150''$ of the galaxy. The total intensity H I map is shown in grayscales, and the beam size is indicated in the bottom-left corner. The black contours are drawn from the velocity field which was used for the estimate of the dynamical center (bulk velocity field from Oh et al. 2008 for IC 2574, hermite velocity field from de Blok et al. 2008 for the other galaxies). The thick line represents the systemic velocity as derived in de Blok et al. (2008). The thin black contours overlaid on the thick white contours belong to the 3.6 μm IRAC image and are usually given at a 2, 5, 10, 20, and 50 percent level of the maximum flux in the image. The white contours are taken from the THINGS radio continuum maps and are usually given at a 10, 20, and 50 percent level of the maximum flux. The black, filled circles indicate the individual center positions from ROTCUR and the black cross represents the chosen dynamical center and its uncertainty. The derived center from the 3.6 μm image is shown as a gray, filled triangle, and the one from the radio continuum as a black, open triangle.
Inset: To better highlight the different center estimates, we additionally show in the upper-right corner an inset with only the central few arcseconds. For clarity, we omit the total H I map and the velocity field contours in the inset. The contours from the 3.6 μm image are shown in black and are given at the same intensity levels as in the main plot. The same holds for the radio continuum contours, which are shown here in gray. The individual center estimates from ROTCUR are shown as small crosses. In the inset, the beam size is indicated by the thick dashed ellipse, which is centered on our best center position.

Row 3: The error bars of all plots in this row are the formal uncertainties as derived by RESWRI.
Left panel: This panel consists of six sub-panels, all of which are plotted against radius in arcsecond. The upper-left sub-panel shows c_1, the amplitude of the circular velocity. The other five sub-panels show the amplitudes of the non-circular components,

namely the second and third order component of the cosine term (c_2, c_3) and the first, second, and third order component of the sine term (s_1, s_2, s_3). The axis scale of these five sub-panels is generally −20 to +20 $\mathrm{km\,s^{-1}}$. The solid, vertical line in the panel containing c_1 indicates the radius corresponding to 1 kpc. All quantities shown in Row 3 are corrected for inclination effects.
Right panel: From top to bottom: systemic velocity c_0; inclination angle i; and position angle PA, all plotted against radius in arcsecond. The dashed, horizontal line in all three sub-panels indicates the weighted mean, using the inverse square of the uncertainties as weight.

Row 4: *Left panel:* This panel consists of two sub-panels. The left sub-panel shows $\tilde{A}_m$, the median amplitudes for each harmonic order m. The values are calculated by radially averaging the quadratically added amplitudes as described by Eqs. 4 and 5. We show the median as determined for the entire extent of the galaxy (filled circles) as well as using only the inner 1 kpc (open circles). The error bars indicate the lower and upper quartile respectively. The right sub-panel shows $A_r(r)$, the radial distribution of the amplitude of all non-circular motions derived following Eq. 6. The error bars of $A_r(r)$ are derived with formal error propagation assuming a Gaussian error distribution. Both $\tilde{A}_m$ and $A_r(r)$ are corrected for inclination effects.
Right panel: This panel contains the elongation of the potential $\langle \epsilon_{\mathrm{pot}} \sin(2\varphi_2) \rangle$ (cf., Eq. 3) *vs.* radius. The elongation is also corrected for inclination. The solid, black line indicates the zero level, the dotted gray one represents the weighted mean elongation, and the dashed, gray ones its standard deviation. The error bars shown here are derived using a formal error propagation assuming a Gaussian error distribution.

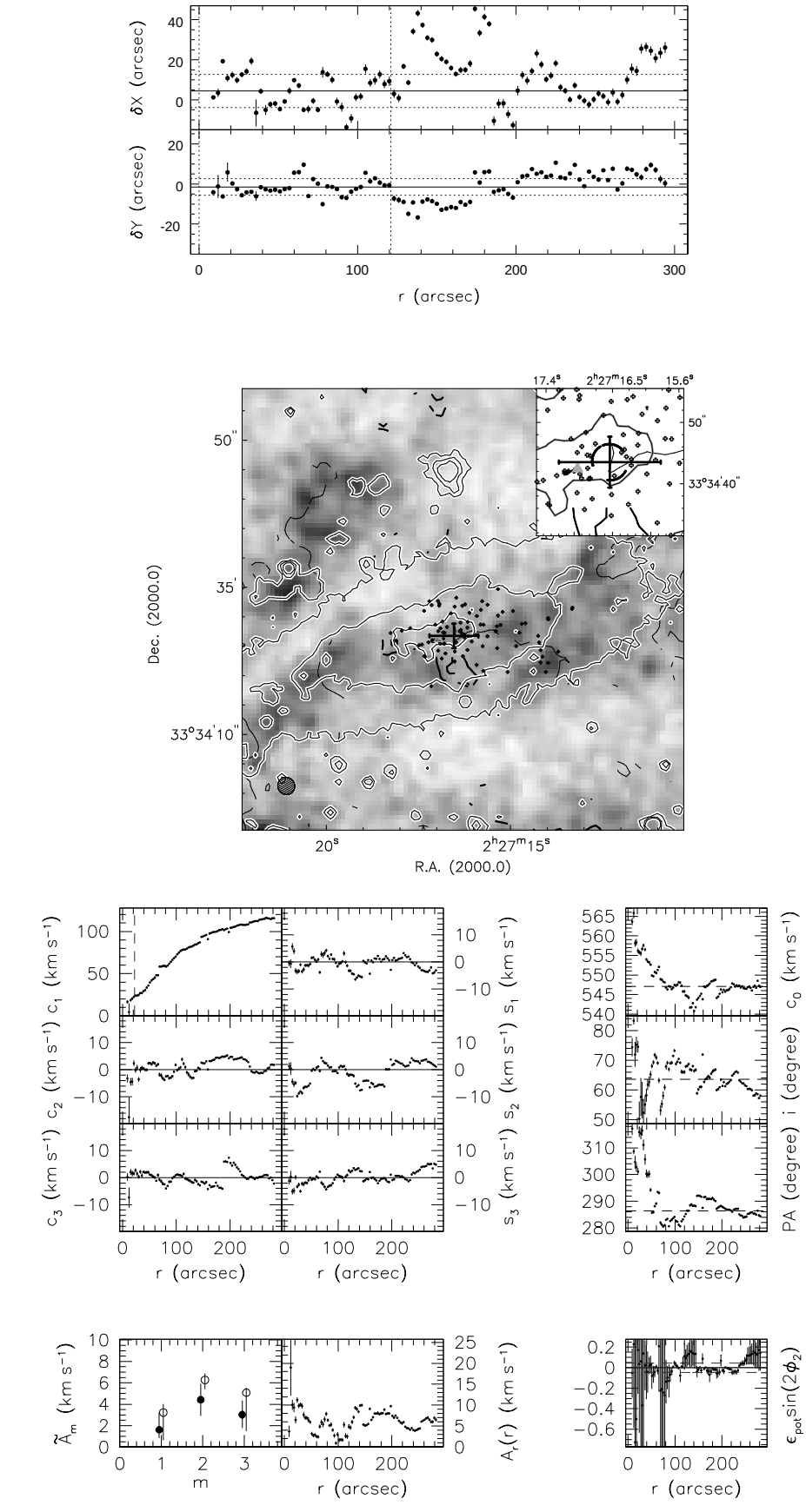

FIG. 25.— Summary panel for NGC 925. Lines and symbols are described in the text, Appendix B. The IRAC center shown was derived using ELLFIT. We omitted the IRAC contours at the 2% and 5% levels for clarity reasons. See Appendix A.1 for a discussion of this galaxy.

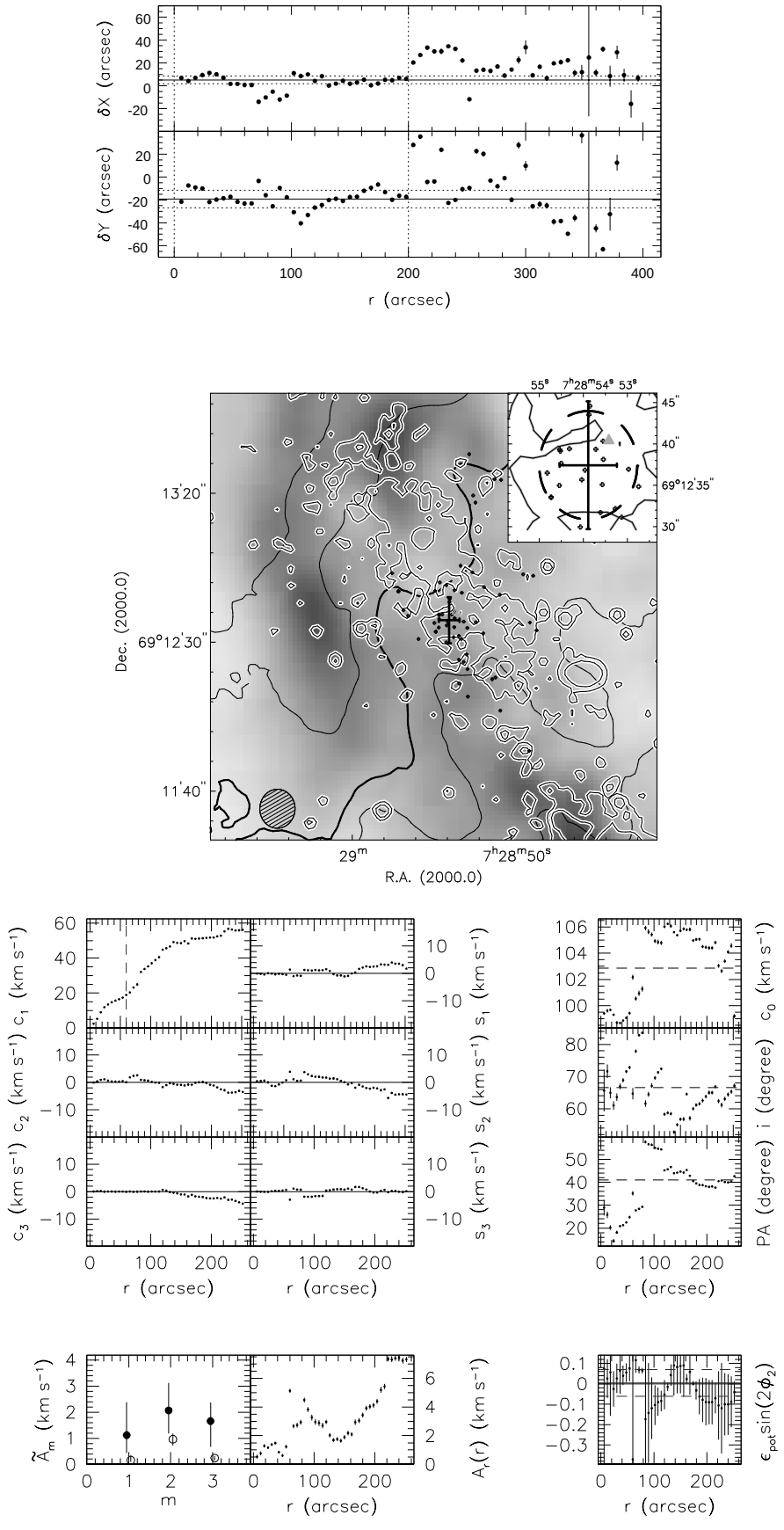

FIG. 26.— Summary panel for NGC 2366. Lines and symbols are described in the text, Appendix B. The IRAC center shown was derived using ELLFIT, and the contours of the IRAC image are given at the 20% and 50% level of the maximum intensity. See Appendix A.2 for a discussion of this galaxy.

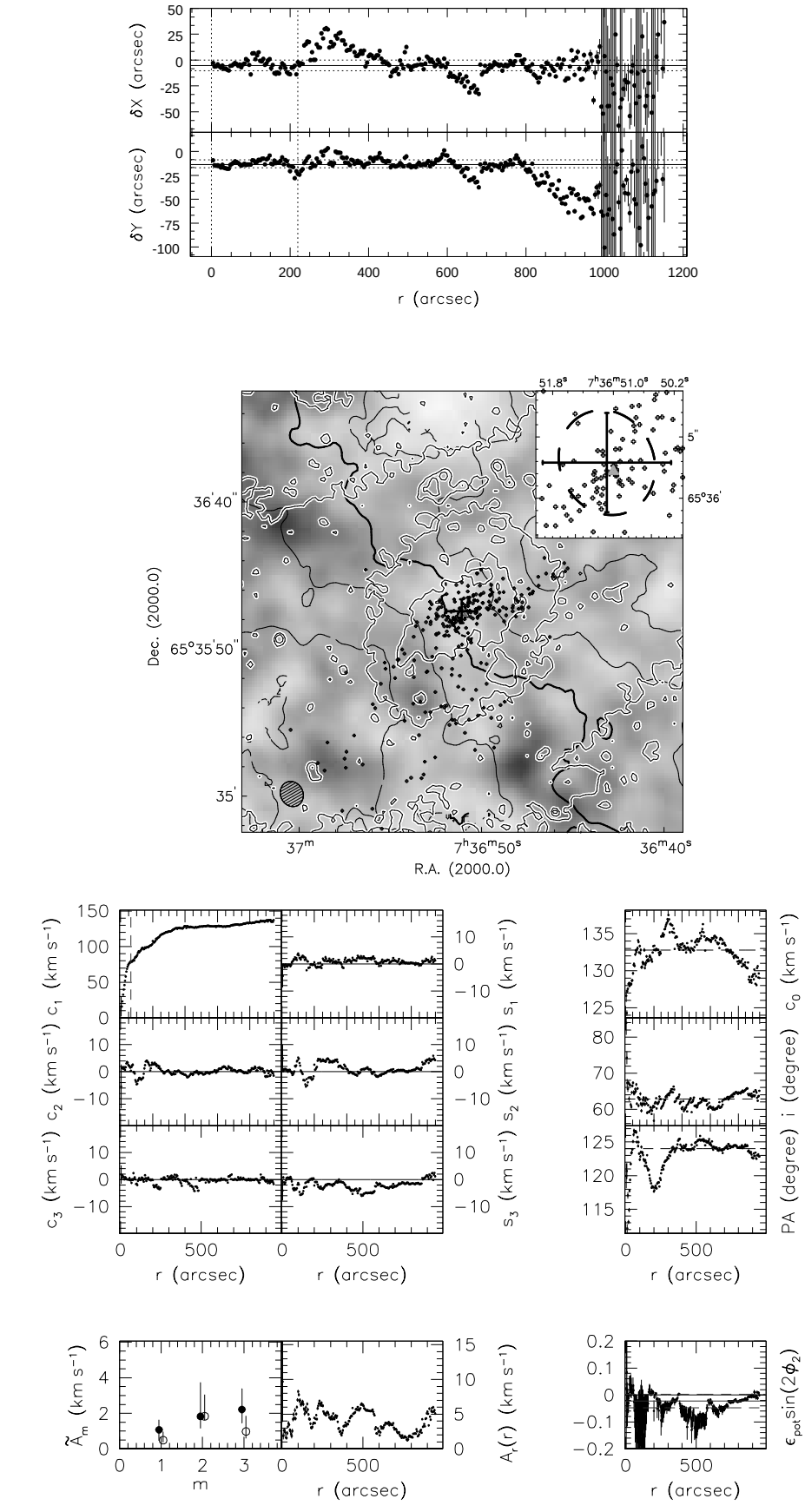

FIG. 27.— Summary panel for NGC 2403. Lines and symbols are described in the text, Appendix B. The IRAC contours are given at the 20, 50, and 80% level of the maximum intensity. See Appendix A.3 for a discussion of this galaxy.

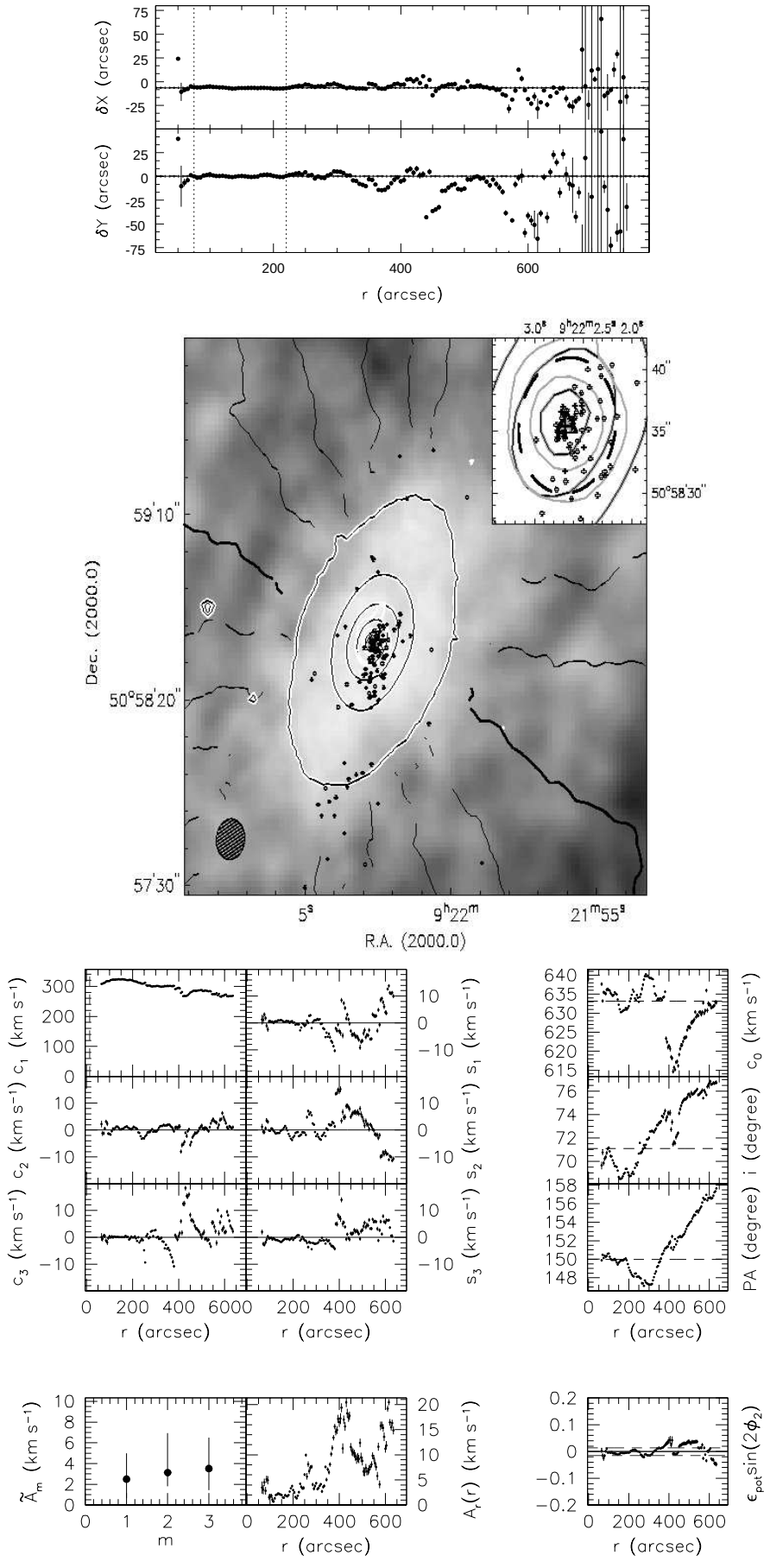

FIG. 28.— Summary panel for NGC 2841. Lines and symbols are described in the text, Appendix B. See Appendix A.4 for a discussion of this galaxy.

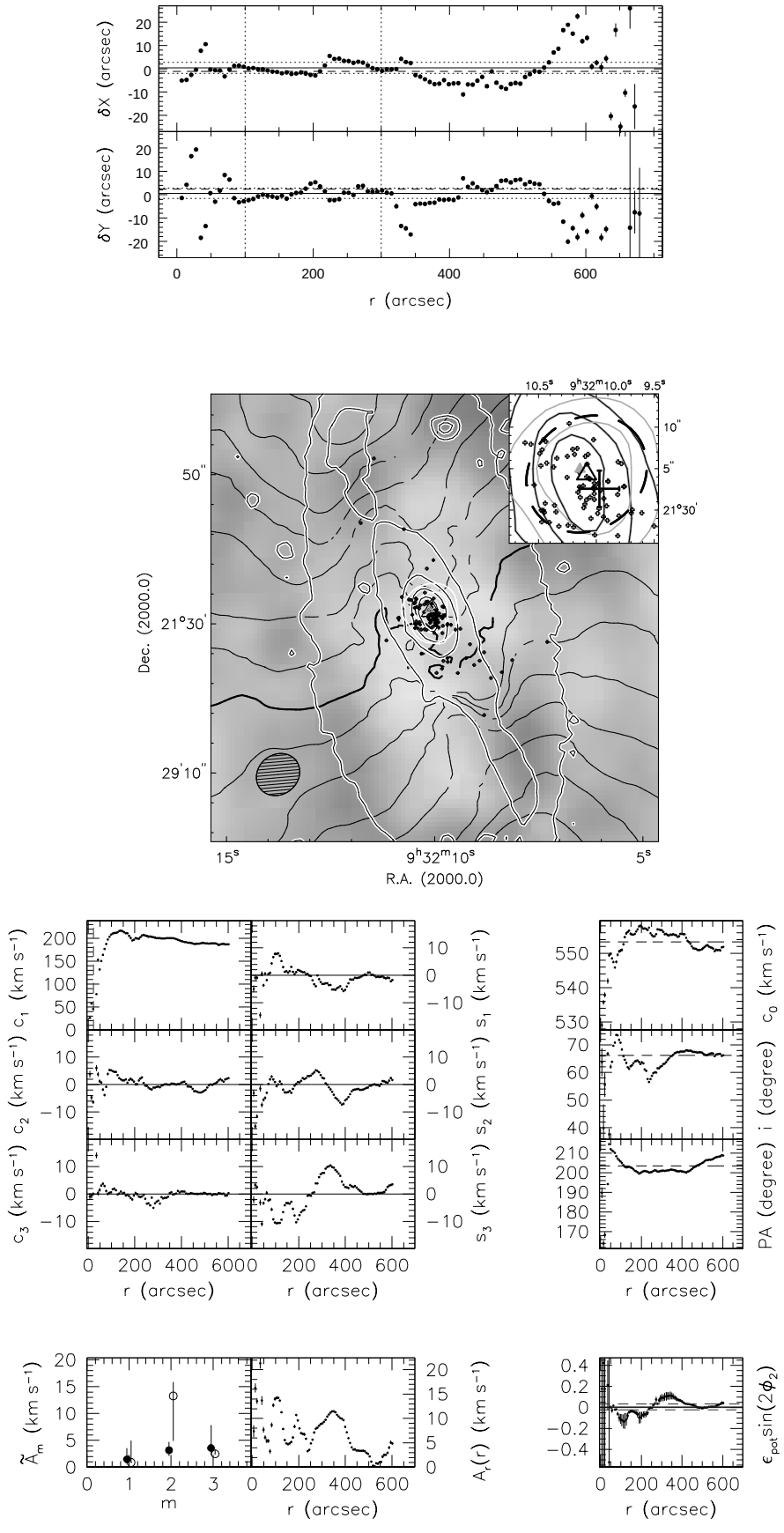

FIG. 29.— Summary panel for NGC 2903. Lines and symbols are described in the text, Appendix B. See Appendix A.5 for a discussion of this galaxy.

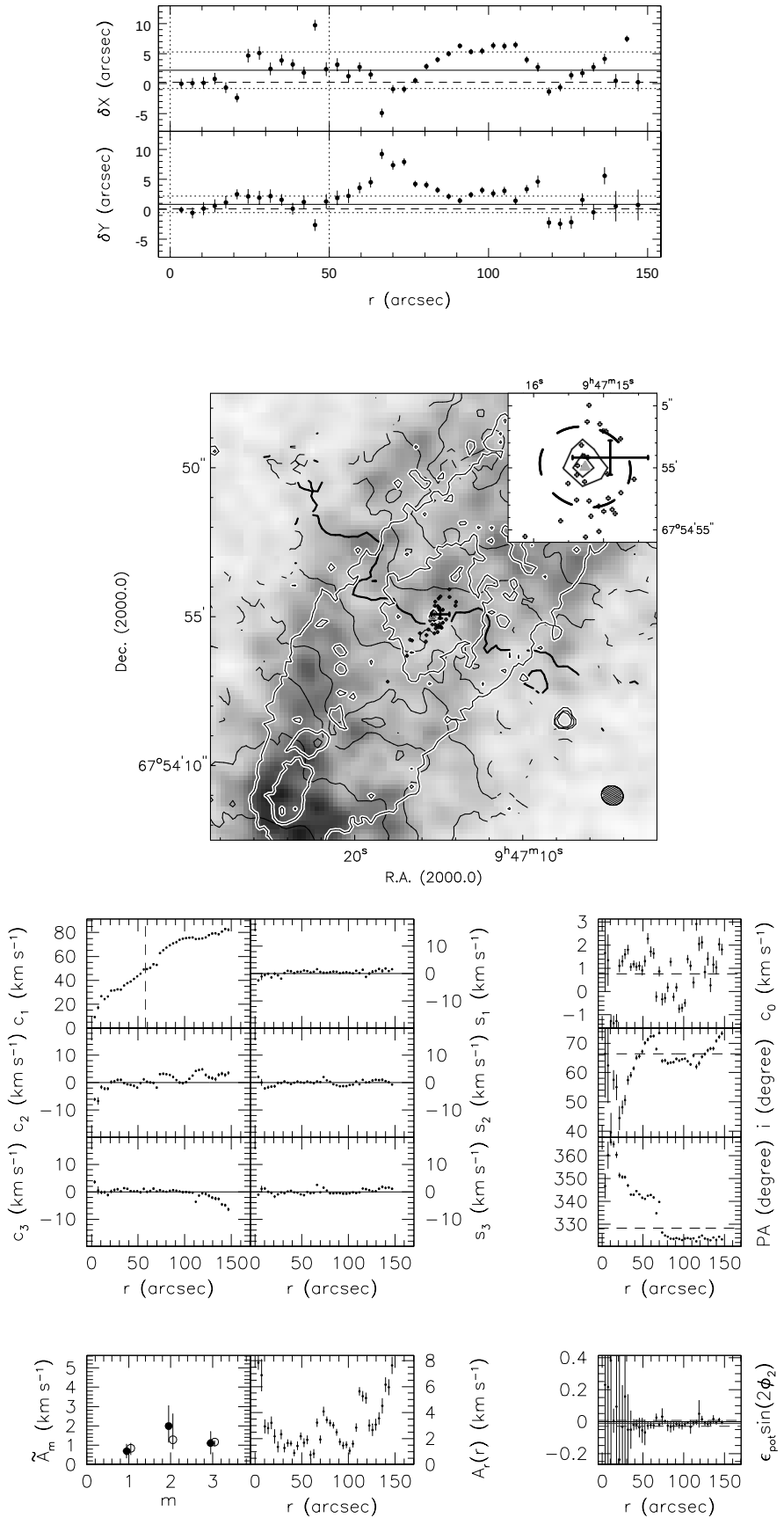

FIG. 30.— Summary panel for NGC 2976. Lines and symbols are described in the text, Appendix B. The IRAC contours are given at the 10, 20, 50, and 80% level of the maximum intensity. See Appendix A.6 for a discussion of this galaxy.

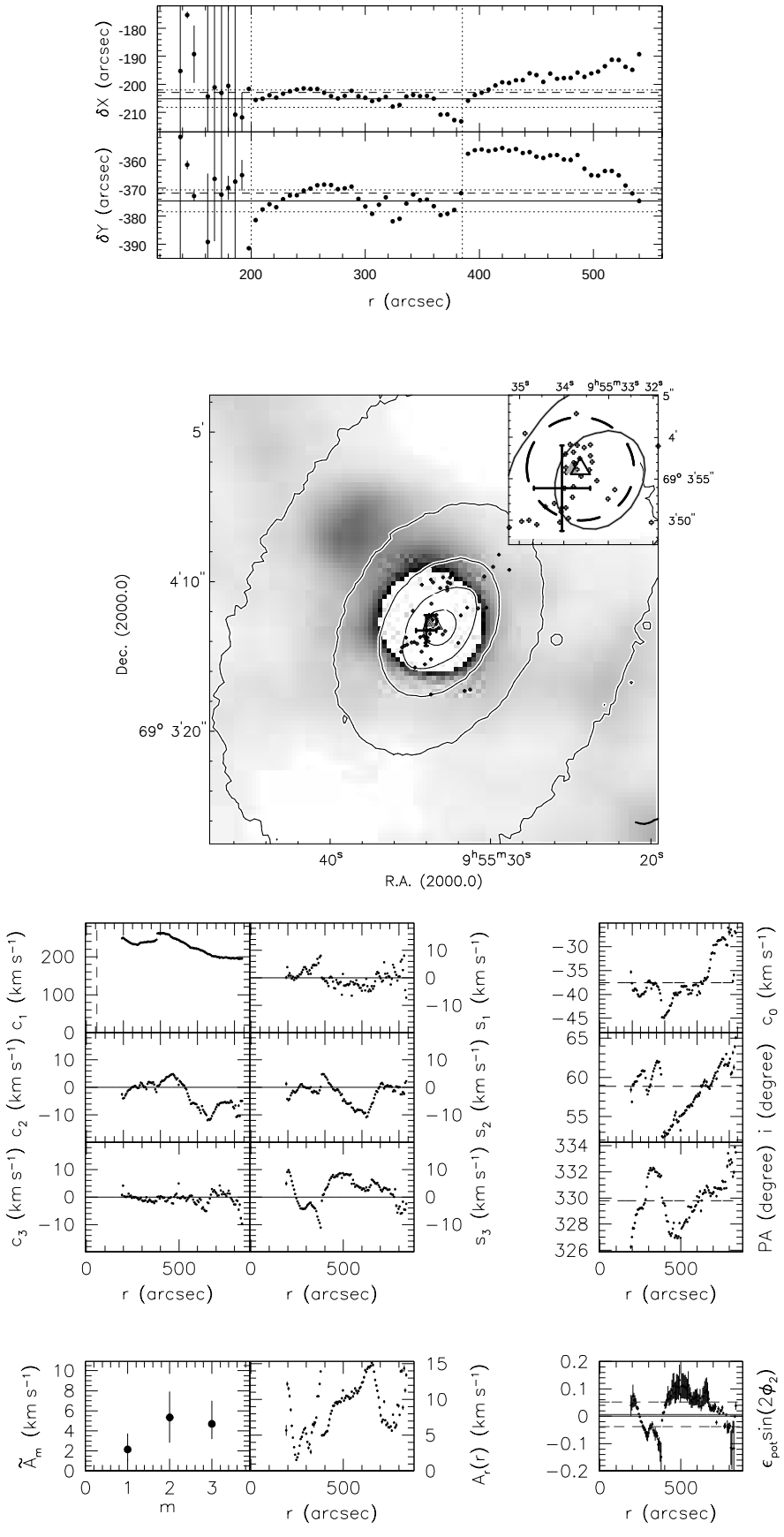

FIG. 31.— Summary panel for NGC 3031. Lines and symbols are described in the text, Appendix B. The bright radio continuum source which is still visible in the total intensity H I map was blanked out for clarity reasons. Due to the central H I deficiency, no velocity contours are visible. See Appendix A.7 for a discussion of this galaxy.

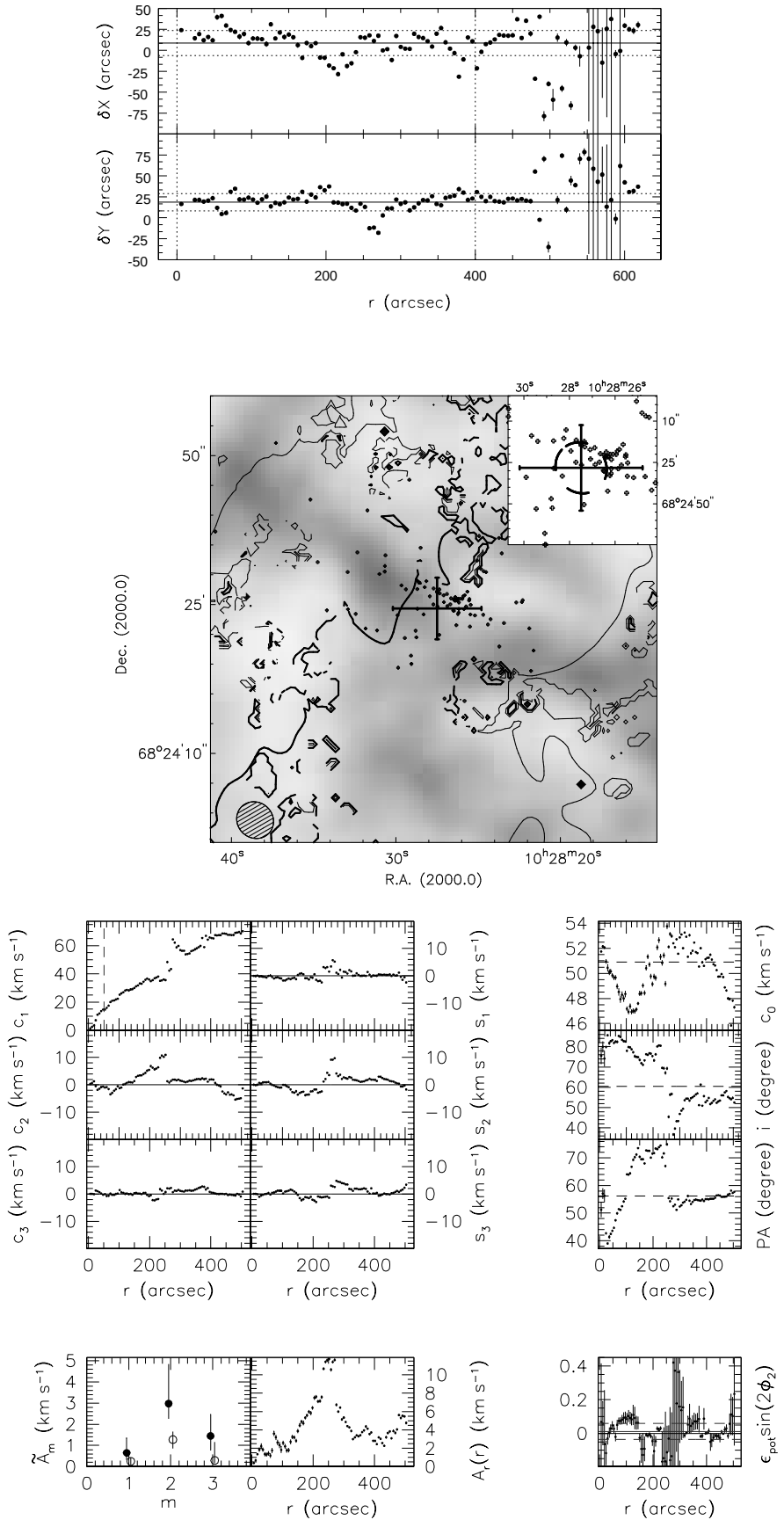

FIG. 32.— Summary panel for IC 2574. Lines and symbols are described in the text, Appendix B. No estimate could be derived from the IRAC and radio continuum images, and their respective contours are therefore not shown. See Appendix A.9 for a discussion of this galaxy.

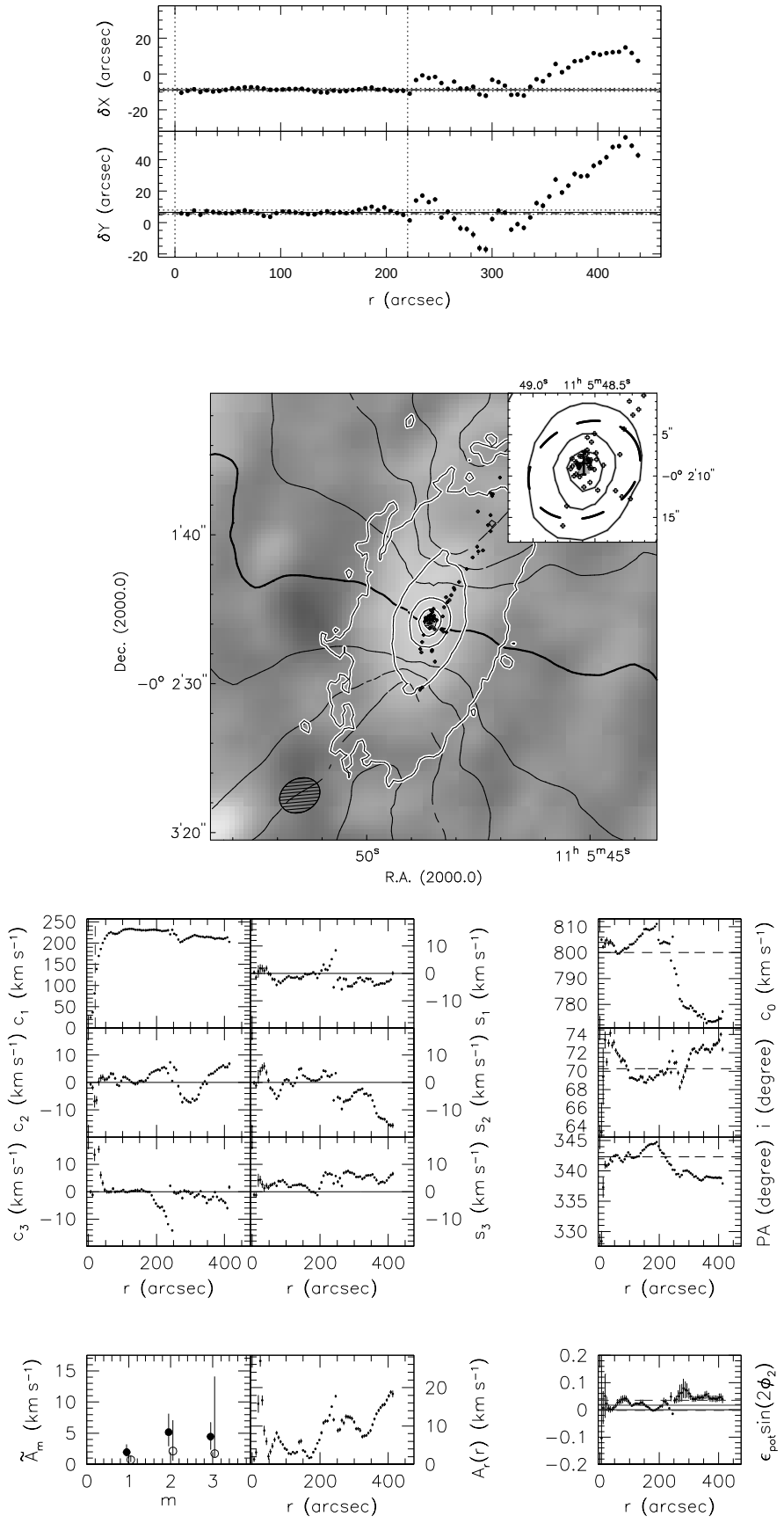

FIG. 33.— Summary panel for NGC 3521. Lines and symbols are described in the text, Appendix B. See Appendix A.10 for a discussion of this galaxy.

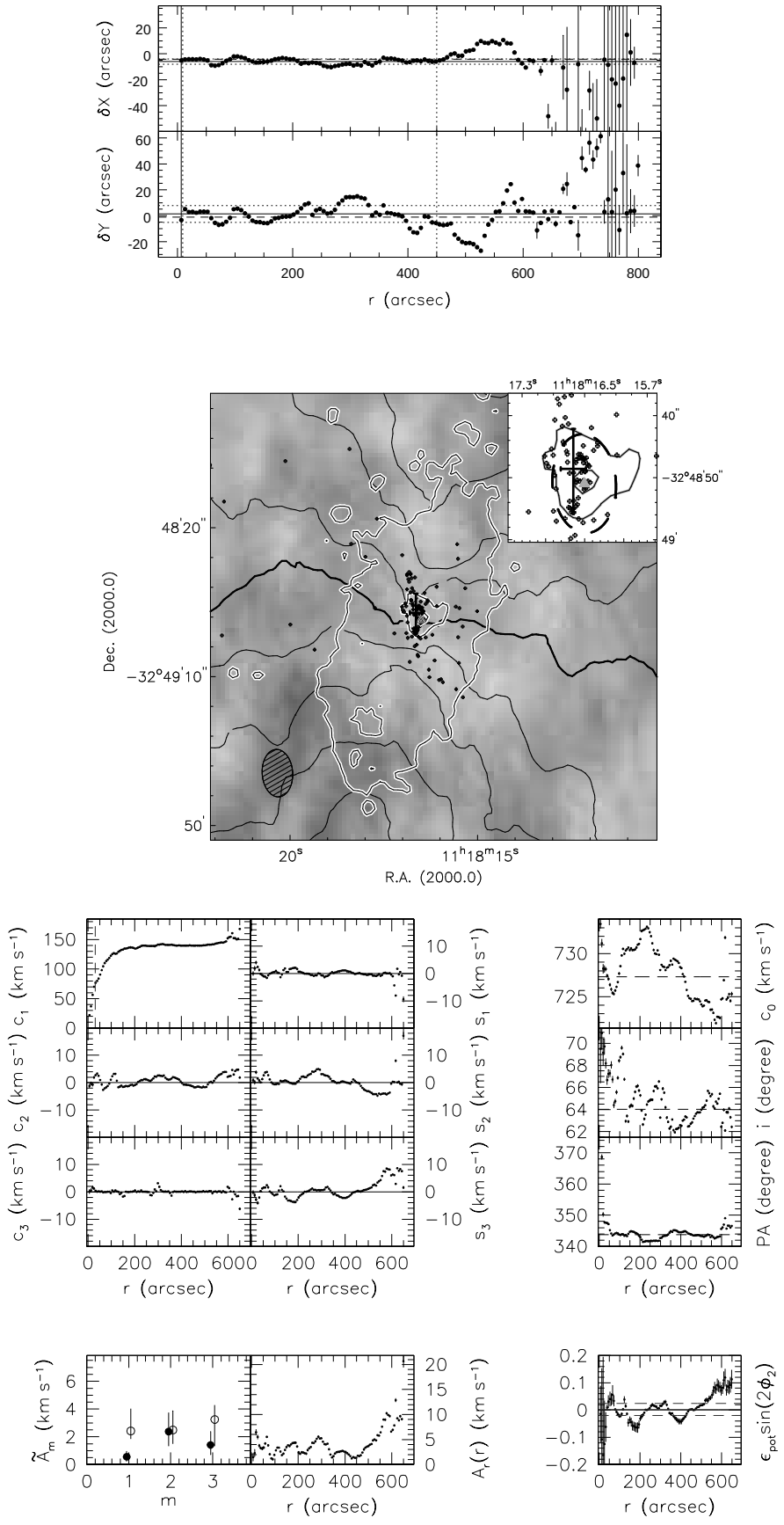

FIG. 34.— Summary panel for NGC 3621. Lines and symbols are described in the text, Appendix B. The IRAC contours are given at the 20, 50, and 80% level of the maximum intensity. Only data with $r \leq 600''$ was used for radial averaging of $\tilde{A}_m$ or $\epsilon_{\rm pot}$. See Appendix A.11 for a discussion of this galaxy.

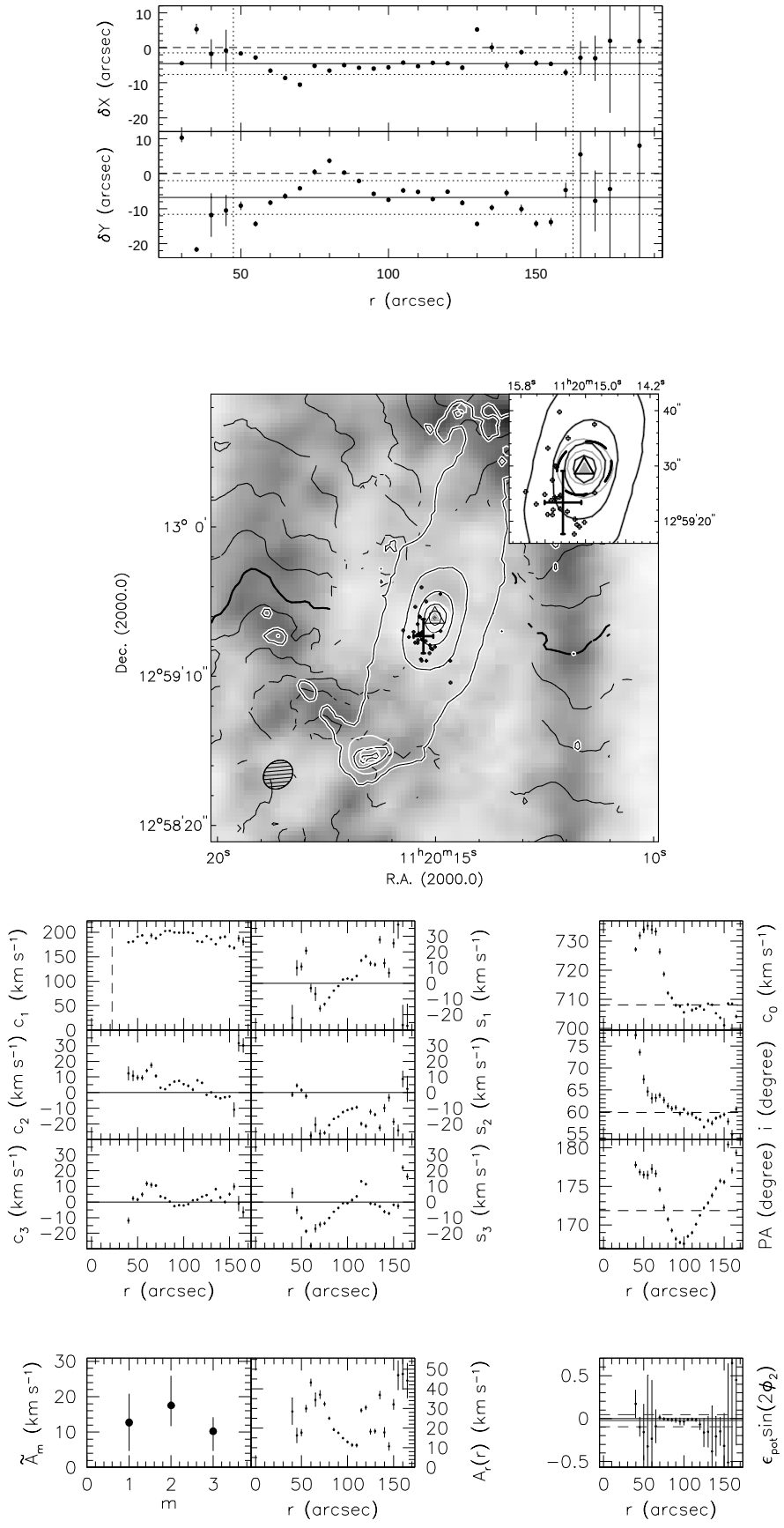

FIG. 35.— Summary panel for NGC 3627. Lines and symbols are described in the text, Appendix B. The axis scale on the panels showing the non-circular components runs from –30 to 40 $\mathrm{km\,s^{-1}}$. See Appendix A.12 for a discussion of this galaxy.

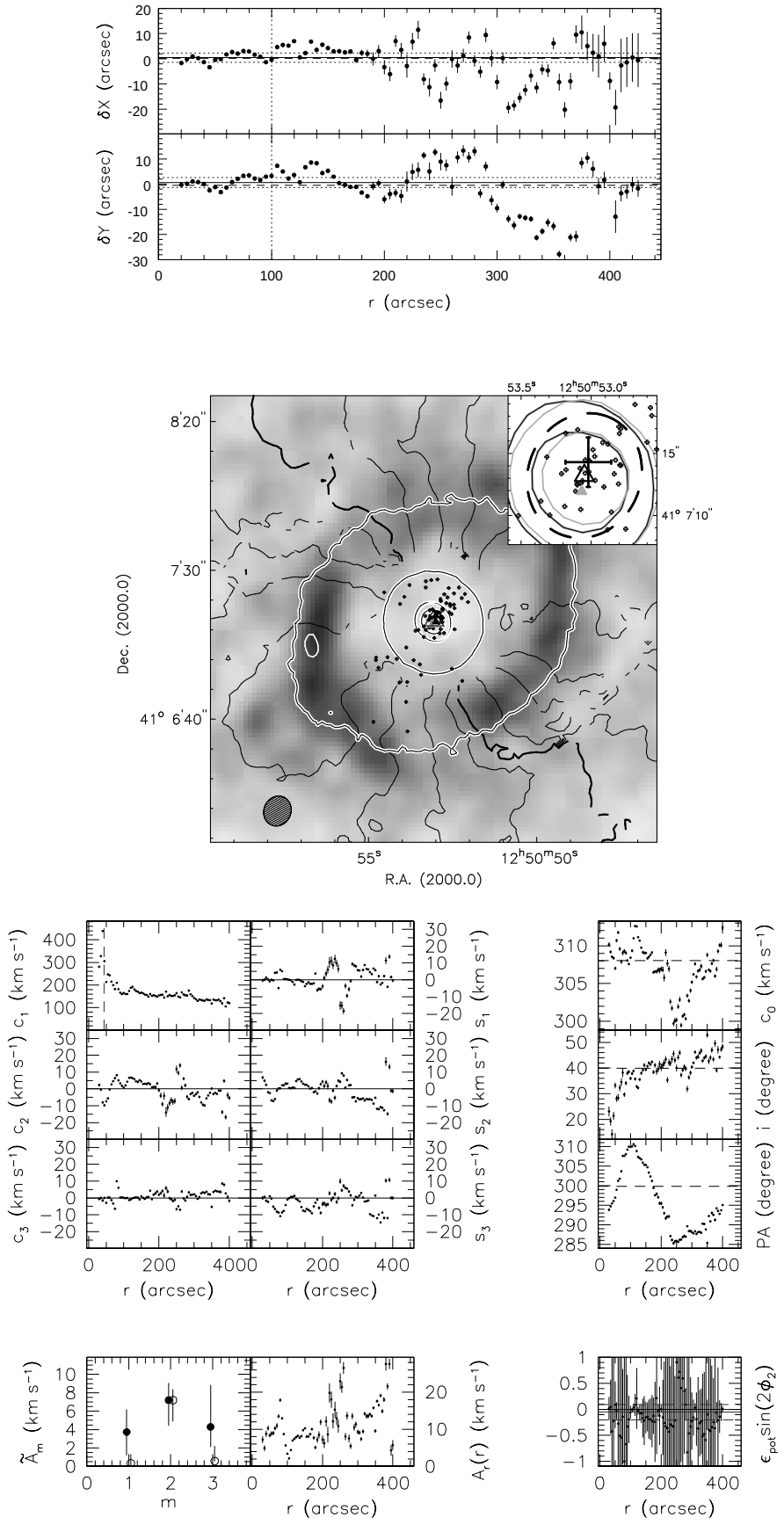

FIG. 36.— Summary panel for NGC 4736. Lines and symbols are described in the text, Appendix B. The IRAC contours are given at the 2, 10, 50, and 80% level of the maximum intensity. The axis scale on the panels showing the non-circular components runs from –30 to 35 km s^{-1}. See Appendix A.13 for a discussion of this galaxy.

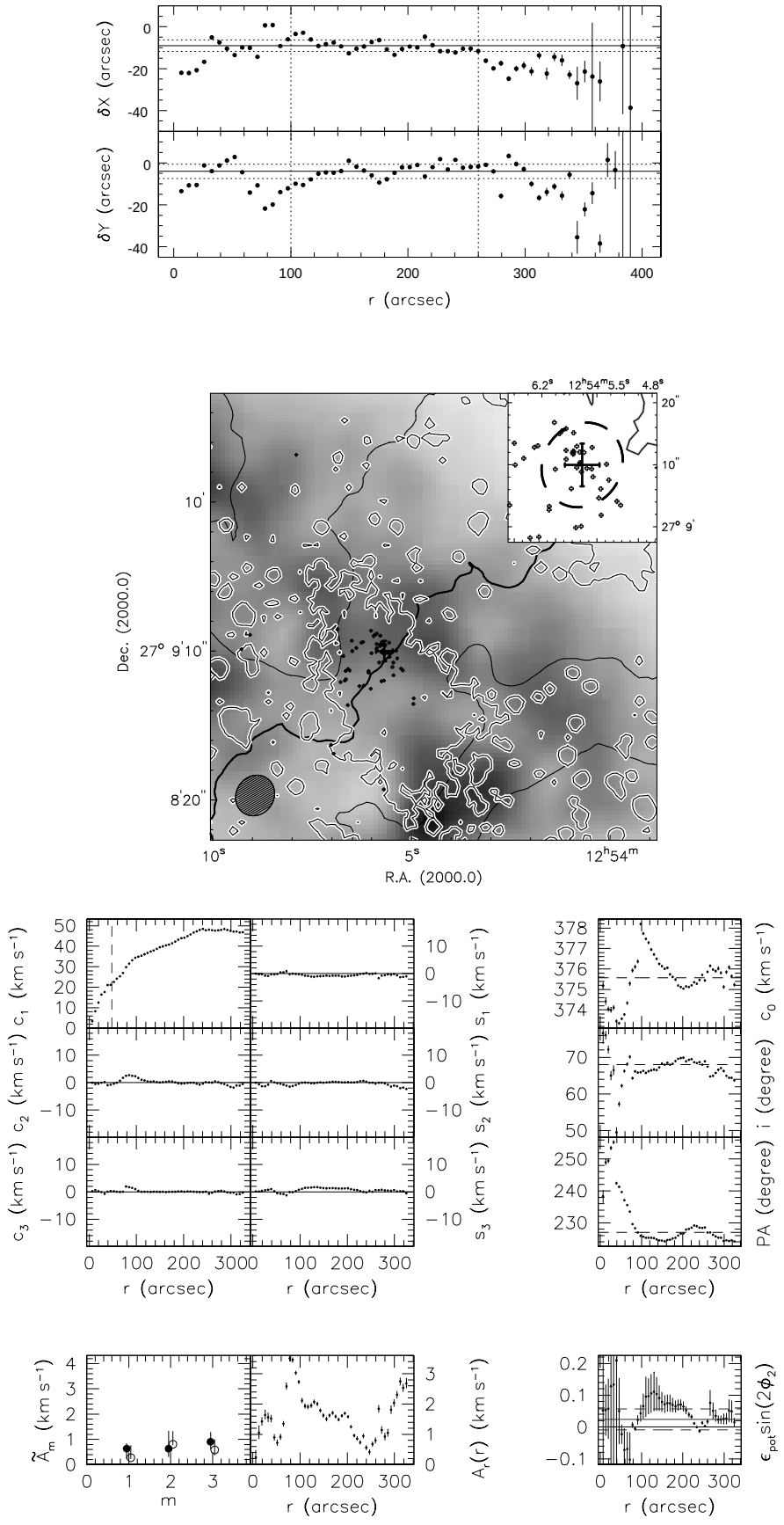

FIG. 37.— Summary panel for DDO 154. Lines and symbols are described in the text, Appendix B. No estimate could be derived from the IRAC and radio continuum images, and their respective contours are therefore not shown. See Appendix A.14 for a discussion of this galaxy.

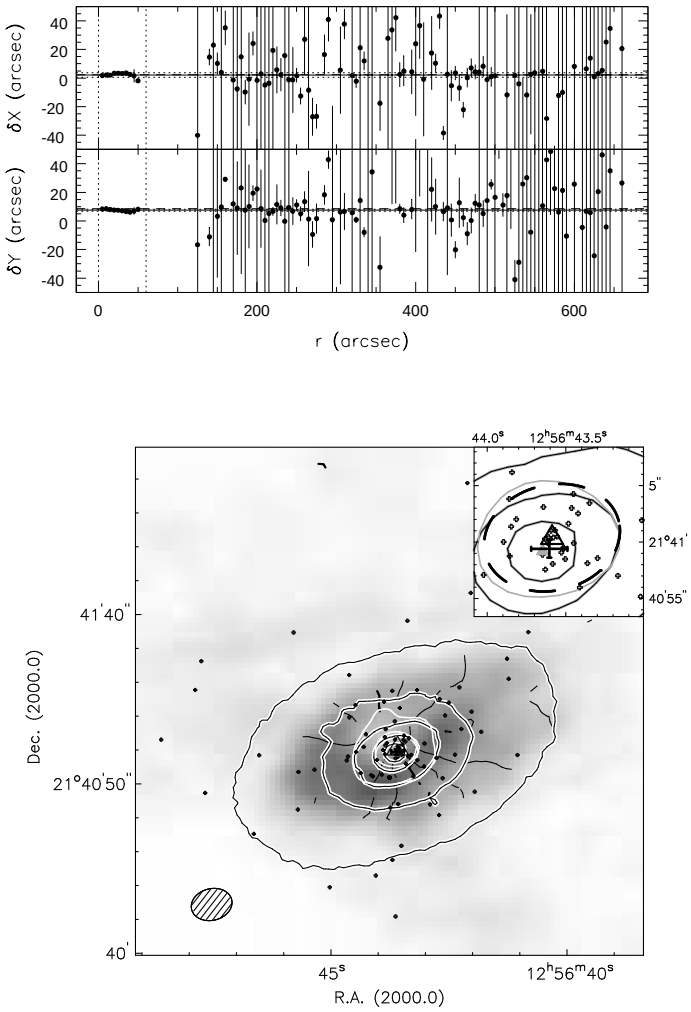

FIG. 38.— Summary panel for NGC 4826. Lines and symbols are described in the text, Appendix B. The lower panel is missing given that we were not able to derive a meaningful harmonic decomposition of the velocity field. See Appendix A.15 for a discussion of this galaxy.

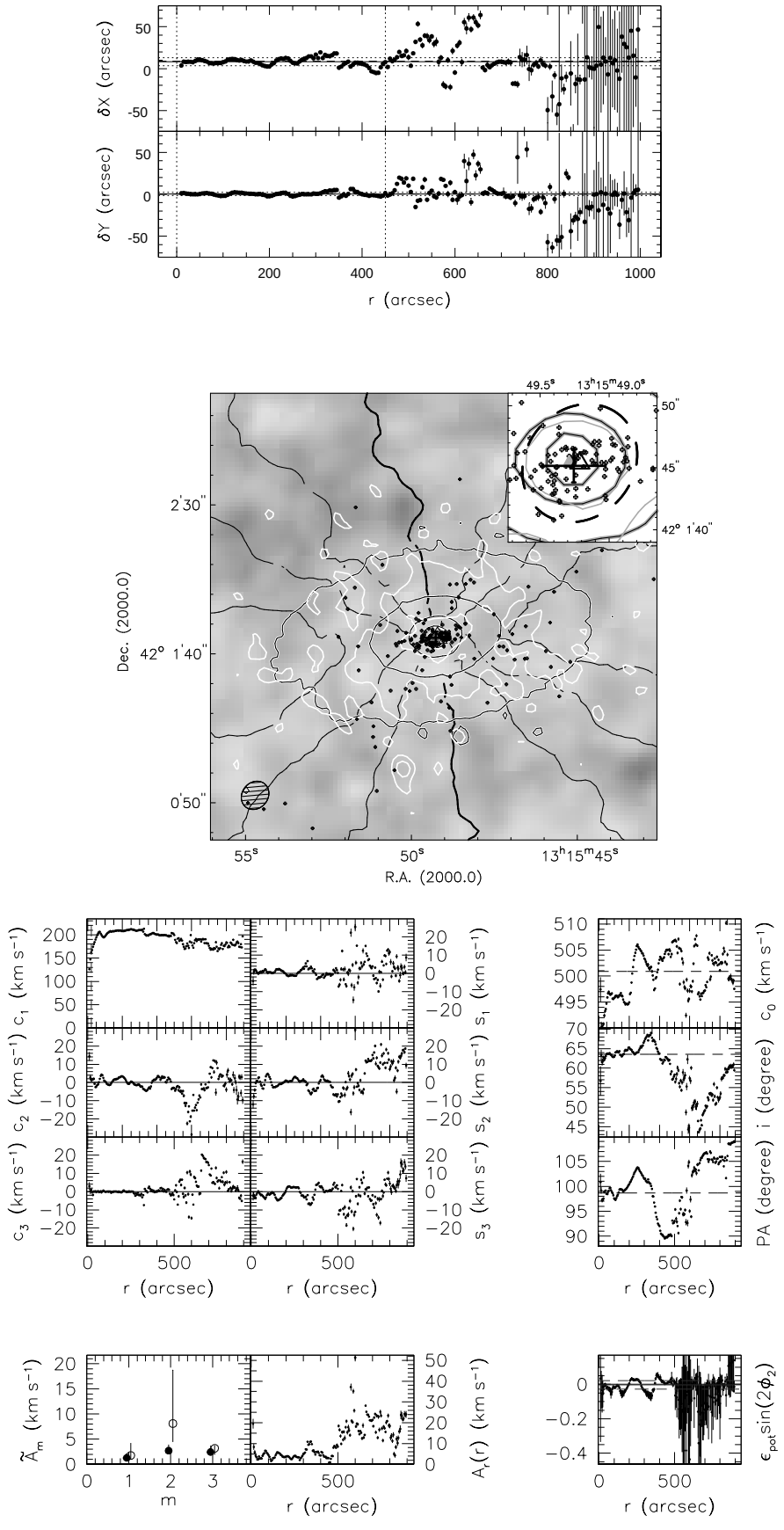

FIG. 39.— Summary panel for NGC 5055. Lines and symbols are described in the text, Appendix B. The axis scale on the panels showing the non-circular components runs from –30 to 30 $\mathrm{km\,s^{-1}}$. Only data with $r \leq 450''$ was used for radial averaging of $\tilde{A}_m$ or $\epsilon_{\rm pot}$. See Appendix A.16 for a discussion of this galaxy.

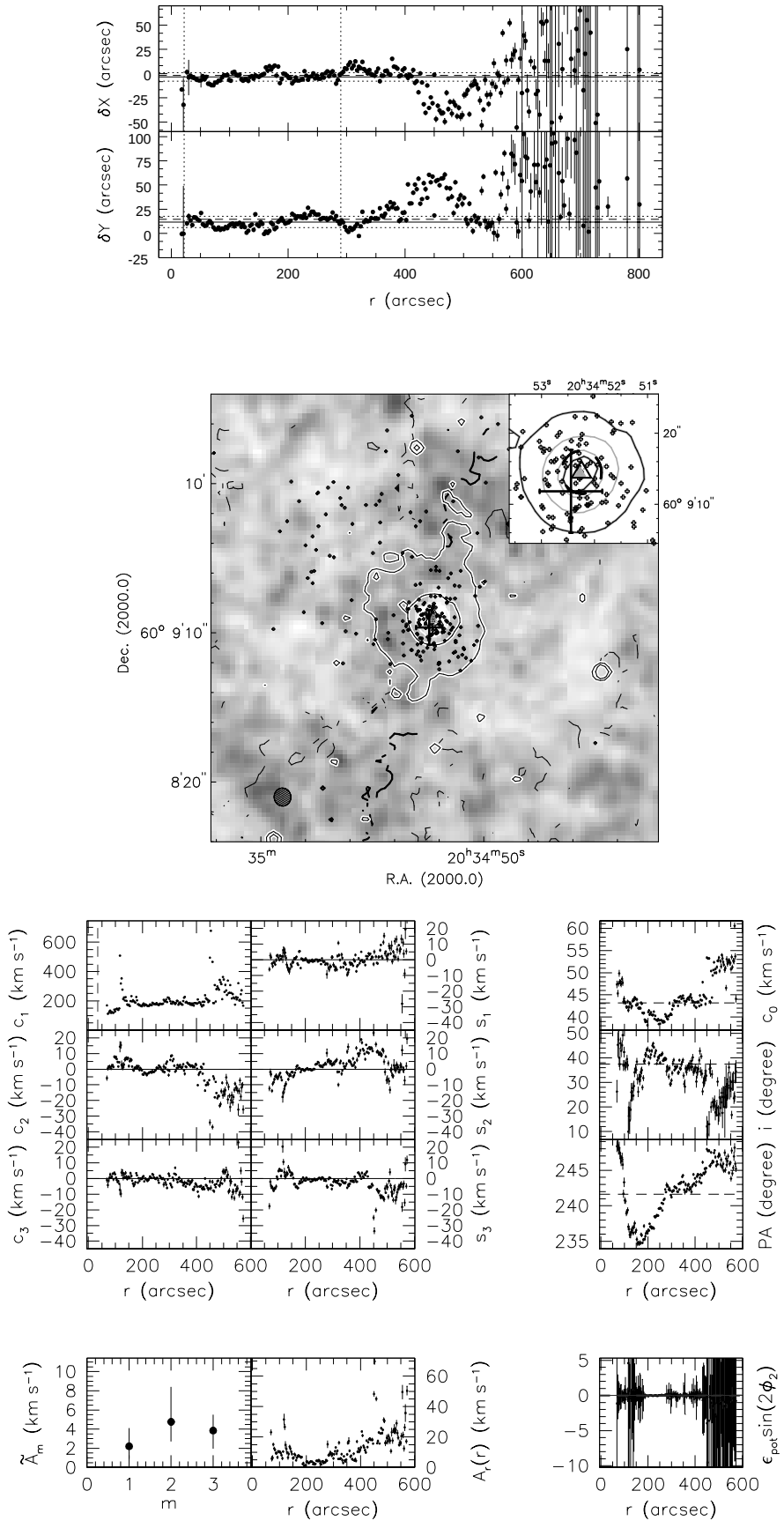

FIG. 40.— Summary panel for NGC 6946. Lines and symbols are described in the text, Appendix B. The IRAC contours are given at the 2, 5, and 50% level of the maximum intensity. The axis scale on the panels showing the non-circular components runs from –45 to 25 $\mathrm{km\,s^{-1}}$. Only data with $r \leq 420''$ was used for radial averaging of $\tilde{A}_m$ or $\epsilon_{\rm pot}$. See Appendix A.17 for a discussion of this galaxy.

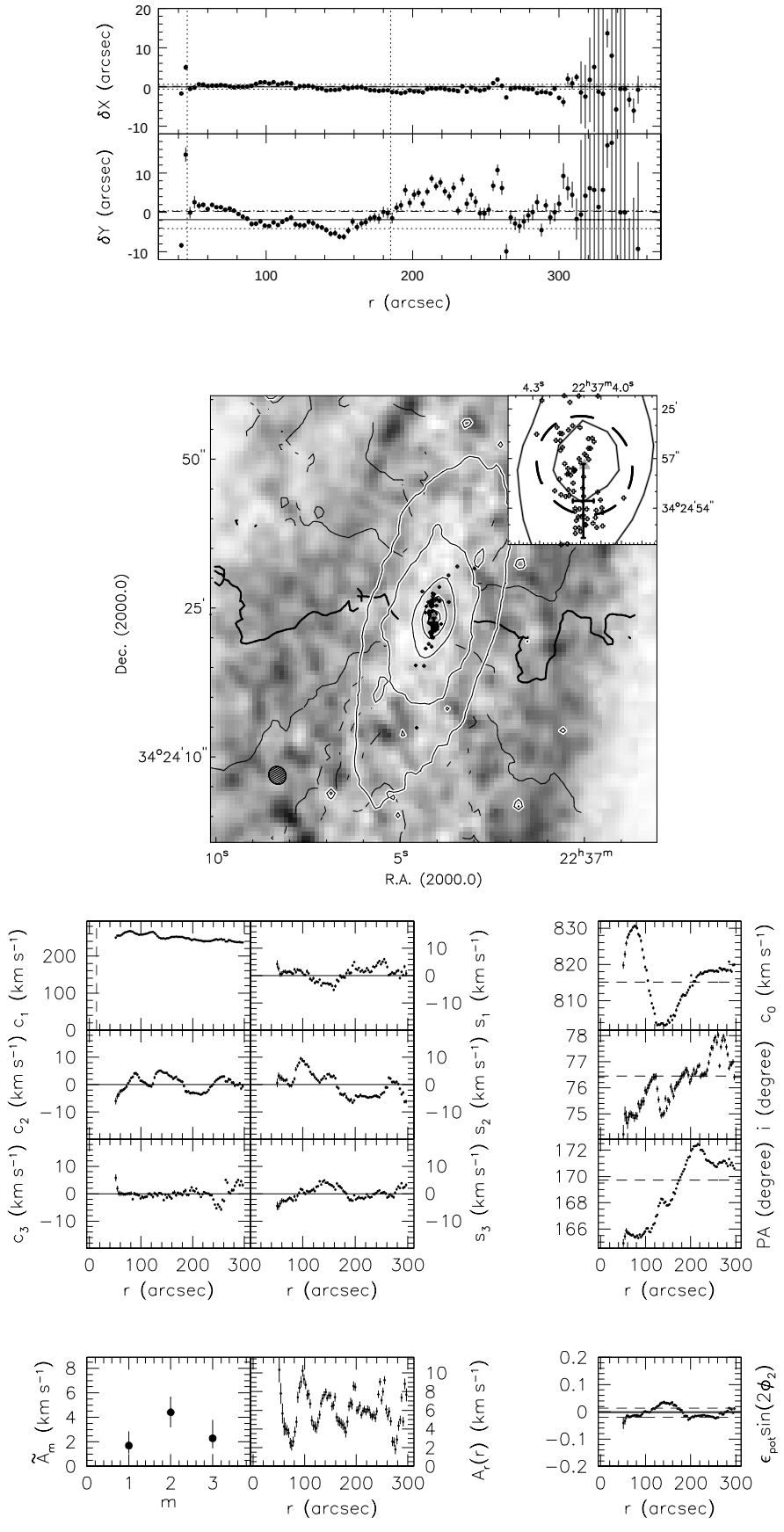

FIG. 41.— Summary panel for NGC 7331. Lines and symbols are described in the text, Appendix B. See Appendix A.18 for a discussion of this galaxy.

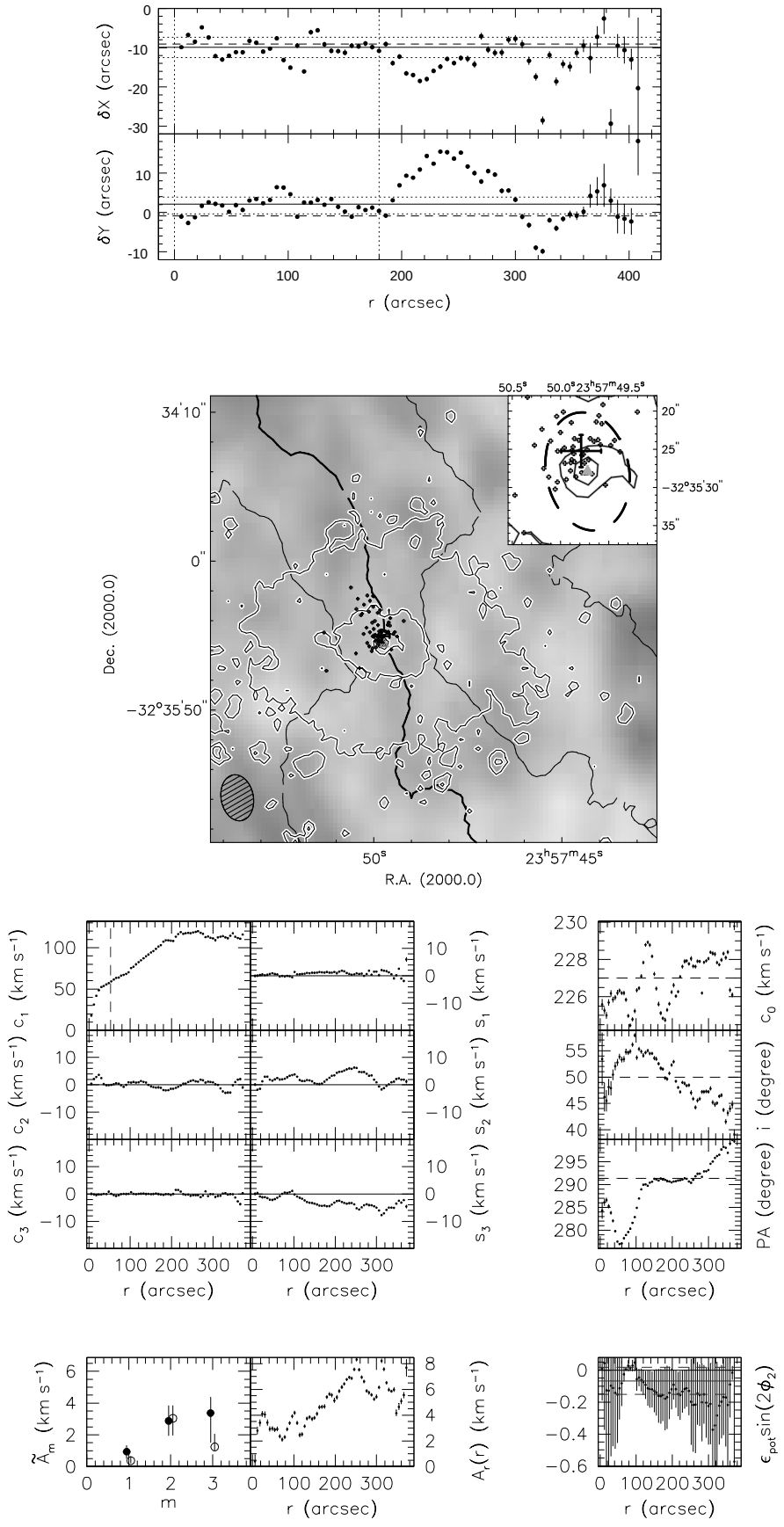

FIG. 42.— Summary panel for NGC 7793. Lines and symbols are described in the text, Appendix B. The 2% IRAC contour was omitted for clarity reasons. See Appendix A.19 for a discussion of this galaxy.